INFORMATION TO USERS

This manuscript has been reproduced from the microfilm master. UMI films the text directly from the original or copy submitted. Thus, some thesis and dissertation copies are in typewriter face, while others may be from any type of computer printer.

The quality of this reproduction is dependent upon the quality of the copy submitted. Broken or indistinct print, colored or poor quality illustrations and photographs, print bleedthrough, substandard margins, and improper alignment can adversely affect reproduction.

In the unlikely event that the author did not send UMI a complete manuscript and there are missing pages, these will be noted. Also, if unauthorized copyright material had to be removed, a note will indicate the deletion.

Oversize materials (e.g., maps, drawings, charts) are reproduced by sectioning the original, beginning at the upper left-hand corner and continuing from left to right in equal sections with small overlaps.

Photographs included in the original manuscript have been reproduced xerographically in this copy. Higher quality 6" x 9" black and white photographic prints are available for any photographs or illustrations appearing in this copy for an additional charge. Contact UMI directly to order.

ProQuest Information and Learning
300 North Zeeb Road, Ann Arbor, MI 48106-1346 USA
800-521-0600

Non-Uniform Sources in the Total/Scattered Finite Difference Time Domain (FDTD) Method

by

Michael E. Potter

A Dissertation Submitted in Partial Fulfillment of the
Requirements for the Degree of

DOCTOR OF PHILOSOPHY

in the Electrical Engineering

We accept this dissertation as conforming
to the required standard

Dr. M. Okoniewski, Co-Supervisor (Department of Electrical and Computer Engineering)

Dr. M.A. Stuchly, Co-Supervisor (Department of Electrical and Computer Engineering)

Dr. W.R. Hoefer, Departmental Member (Department of Electrical and Computer Engineering)

Dr. J. Bornemann, Departmental Member (Department of Electrical and Computer Engineering)

Dr. D. Olesky, Outside Member (Department of Computer Science)

Dr. R. Ziolkowski, External Examiner (Department of Electrical and Computer Engineering, University of Arizona)

Supervisor: Dr. M. Okoniewski, Co-Supervisor (Department of Electrical and Computer Engineering)

ABSTRACT

The Finite-Difference Time-Domain (FDTD) method has been used extensively in electromagnetic field modeling because of its ability to robustly handle interactions of fields with complex heterogeneous structures. In particular, the total/scattered field formulation has allowed for efficient implementation of arbitrarily directed uniform plane waves, consequently facilitating efficient modeling of far-field scattering problems. The total/scattered approach is not restricted to plane waves and can be expanded to any waveforms that can be described in analytical or semi-analytical form.

While existing formulations of FDTD have been immensely successful, they are not well suited to problems that involve near field scattering/interaction problems, where both the source and object are in the same domain but at a substantial distance from each other. This is due to the exceedingly high demands for computational resources that may result from the domain size, and/or dramatically different requirements for the mesh density in the source and object areas. One solution to this problem is to separate the domain into source and scatterer regions coupled by surface boundary radiation conditions. However, this method can incur large storage requirements for calculation of the radiation conditions.

A specific near-field situation of interest to the utility industry is the case of workers near high voltage powerlines. In this instance, the field pattern takes on a cylindrical, transverse electromagnetic character. More general radiating sources can be accurately represented in the near-field by using spherical wave expansions, which are often used to represent antennas measured on test ranges. Successful implementation of these analytic solutions is feasible within the FDTD framework, and would allow for the illumination of the scatterer modeled at a considerably lower cost than in the standard approach. This thesis presents a method where these non-uniform, near-field, sources can be implemented implicitly as source conditions in an existing FDTD method. The specific case of powerline

fields is described first, followed by the more general case of spherical waves.

The analytic solution for powerline fields is implemented to show that near-field source configuration can be successfully modeled implicitly with accurate and efficient results. The method is validated by comparing with known analytic solutions, with very good accuracy being achieved. Then, a specific example of a human under a powerline close by is modeled to examine predictions made earlier under the assumption of a plane wave source condition. For a similar powerline source configuration, results of organ dosimetry predict that induced fields are from ten to sixty percent greater than predicted with the plane wave source.

This same approach is applied to model a more general and difficult problem, namely spherical waves as sources in the total/scattered FDTD, called the SW-FDTD. Since transverse properties of spherical modes are known, the behavior of a mode can be represented on a one-dimensional radial grid. Thus, much like the plane wave sources in the FDTD method, the spherical wave modes are time-stepped on one-dimensional staggered electric/magnetic field source grids in the radial direction, representing mode propagation in free space. Spherical wave modes can then be interpolated and summed on the Huygens' surface to represent the total field of the source, thus providing the coupling between the complex source and a scatterer using one-dimensional grids. It is assumed that the object of interest is beyond the reactive near-field of the source, and therefore there is no significant coupling between source and object.

The SW-FDTD method is validated by comparing simulations with several analytic solutions that increase in complexity, demonstrating very good accuracy. Issues relating to the numerical implementation are discussed, including the effects of numerical dispersion, stability, and simple Mur first order boundary conditions. Incorporation of the method as a source condition in an existing FDTD program, and validation of this synthesis, show that the SW-FDTD method can implictly model sources as accurately as explicit models do. The efficiency, and the reduction of errors remain issues for further research to improve the overall utility of the SW-FDTD method.

Examiners:

Dr. M. Okoniewski, Co-Supervisor (Department of Electrical and Computer Engineering)

Dr. M.A. Stuchly, Co-Supervisor (Department of Electrical and Computer Engineering)

Dr. W.R. Hoefer, Departmental Member (Department of Electrical and Computer Engineering)

Dr. J. Bornemann, Departmental Member (Department of Electrical and Computer Engineering)

Dr. D. Olesky, Outside Member (Department of Computer Science)

Dr. R. Ziolkowski, External Examiner (Department of Electrical and Computer Engineering, University of Arizona)

Contents

List of Tables

List of Figures

Chapter 1

Introduction

1.1 Motivation

Thirty years ago, the application of efficient numerical methods to practical electromagnetic (EM) problems was still in its infancy. Analytic models were available for a set of simple shapes, but they were inadequate for modeling problems of interest. As is often the case, military needs were driving the demand for modeling extremely complicated and large structures (e.g. radar cross section, RCS, evaluation). There was also a growing interest in modeling electromagnetic interactions with the human body. For some complex shapes, an integral equation (IE) method such as the method of moments (MoM) was the method of choice. However, at that time MoM was able to solve for only a few hundred unknowns. There truly were no practical numerical methods for electrically large problems, especially if the structure was heterogeneous, mainly because of prohibitive computational demands.

The next decades ushered in a rapid increase in computing power, with a corre-

sponding increase in the affordability of that power. For research in electromagnetics, the direct result was the ability to solve problems that previously were prohibitively complex. The MoM approach was still perceived as having difficulty with large, heterogeneous problems; consequently, along with the marked increase in computer power, there was also an explosion in the number of methods to deal with such problems. Finite-element methods (FEM) partially alleviated some of the restrictions of the MoM, but in general researchers started to gravitate towards partial differential equation (PDE) solutions to Maxwell's equations for many different reasons. These reasons include robustness for complex geometries, the ability to handle heterogeneous structures in a straight-forward manner, and in some methods the elimination of the need to solve large, dense matrix equations. The finite-difference time-domain (FDTD) method, as introduced by Yee [1], is one such approach that has gained widespread popularity because of its simple and elegant formulation, and because it continues to be refined and enhanced for numerous applications.

Although Yee published his paper in 1966, the method did not enter the mainstream until the late 1970's. A possible reason that this paper was largely ignored was the inability of the proposed method to model an "open" problem for any significant period of time. Firstly, at the time there was no efficient way of specifying a uniform plane wave source, which was a necessary condition for RCS predictions. Secondly, there was still no valid method to model the open problem at the edges of the computational domain. But in time both these problems have been alleviated; the total/scattered field formulation of Taflove [2] allows for the efficient implementation of plane waves, and research in absorbing boundary conditions for open problems has progressed rapidly to allow scattering

predictions rivaling those managed in anechoic chambers.

One particular area of research that has gained interest in the last decade has been electromagnetic interactions with biological objects, including the human body, to aid in identification of potential health hazards. Initial research in this area utilized MoM, but the resolution achieved by this method was simply not good enough for the determination of the specific absorption rate (SAR), which is a benchmark figure in such studies. The problem is that biological objects are complicated, with extensive material heterogeneities at small and large scales. The FDTD method has quickly become the method of choice for modeling these interactions since it is inherently well suited to such heterogeneous objects. Moreover, elegant modifications to the FDTD method have enabled the range of exposure frequencies to extend from the quasi-static region (10 Hz - 100 kHz) to the microwave region (1-20 GHz). As a result, problems such as the exposure of humans to power lines or cellular phones have been successfully investigated.

Although the FDTD method has attained success in scattering and exposure predictions, work in this area to date was restricted to either using uniform plane wave sources (effectively modeling in the far-field), or incorporating the EM sources in the computations (resulting in increased computational complexity). Incorporating the source in computations increases computational complexity in two ways. First, the numerical volume needed to incorporate the source *and* any objects of interest is necessarily greater than the volume of the objects of interest alone. Secondly, the source may require greater numerical accuracy than the objects of interest due to its shape and/or size. As a result, one may need to utilize a finer mesh (depending on the computational method) for that area of the com-

putation, or perhaps for the entire computational volume if no sub-gridding techniques are available. In either case, the result is an increase in the computational resources required. In many cases this increase is substantial enough to prohibit a solution altogether.

In reality, there are many cases where the object of interest is located in the radiating near-field of the source, where plane wave approximations are not appropriate. For instance, for some industry workers there is concern regarding the health effects of e.g. exposure from cellular base station antennas. These workers often have to service equipment in close proximity to such antennas, and the antennas can not be shut off because the provider would lose service. In the military, a similar situation exists for personnel in naval vessels, where a large number of high power antennas are clustered in a limited space. The radiation pattern and sighting lines for these antennas, which have complicated structures in the near-field, must also include the source and object in any modeling. Another application could be the simulation of radar target returns and the classification of targets in the near-field of any military antenna system.

With these examples in mind, it is clear that a niche exists for accurately modeling complicated problems in the near-field of sources. Since computational resources can become taxed with complex source-object configurations, it would be beneficial to be able to avoid explicitly modeling one or the other. In practice, it is much easier to classify sources implicitly.

These problems provide motivation for a solution: to implement a method where sources, other than uniform plane waves, can be accurately modeled without having to directly incorporate the source structure in the computational domain. This would allow

for modeling of objects in the near field without incurring the computational overhead arising from the source geometry; the scatterer alone will determine the mesh requirements. The research in this thesis will address these problems.

1.2 Objectives

The overall objective of this research is to investigate effective methods for modeling of sources other than uniform plane waves in the FDTD method. Since the scenarios of interest can involve complicated structures with possible heterogeneous material properties (e.g. the human body), the computational method utilized for the research must be robust and able to handle such possibilities. The FDTD method has been chosen because it is well suited to such problems. Since its introduction by Yee, the FDTD method has been used extensively in electromagnetic field modeling because of its ability to robustly handle interactions of fields with complex heterogeneous structures. In particular, the total/scattered field formulation [2] has allowed for efficient implementation of arbitrarily directed uniform plane waves, consequently facilitating efficient modeling of far-field scattering problems. The equivalence principle, which admits sources to a computational domain, is summarized by Stratton [3]:

> An electromagnetic field is uniquely determined within a bounded region V at all times $t > 0$ by the initial values of electric and magnetic vectors throughout V, and the values of the tangential component of the electric vector (or magnetic vector) over the boundaries for $t > 0$.

If the electromagnetic fields can be specified on the boundaries, the radiation from any source can be recreated in V. In the FDTD method, uniform plane wave sources are

implemented with a Huygens' surface formulation (also known as the total/scattered field formulation), where the electric and magnetic source fields are specified on a closed surface surrounding a computational volume. Thus, plane waves incident on the domain can be initiated in any direction.

The theorem allowing the specification of incident fields on such a surface, and representing exactly the resultant fields within that volume, is not restricted to uniform plane waves. The aim of this research is to allow for Huygens' sources other than uniform plane waves, in order to efficiently model more general situations of interest. The focus is specifically on sources that accurately model near-field situations, without explicitly having to model the source (e.g. the antenna).

1.3 Contributions

In this thesis, the research completed to date is fully outlined, along with suggestions for future work. One contribution is the development of a methodology for low frequency line-sources to be implemented as sources in the FDTD method. The impact of the success of this methodology is that more accurate predictions of the impressed fields in objects near high voltage powerlines can be made. This is particularly important for the assessment of safety for personnel working in such situations, where the exposure fields can then be evaluated.

The other significant contribution is the development of a method to allow any source to be utilized by propagating its spherical wave expansion as a source in the total/scattered field formulation. This spherical wave FDTD method is important since the

source will not need to be explicitly modeled in the computational domain. As a result, substantial savings in computational resources can be realized.

1.4 Thesis Outline

Chapter 2 provides a comprehensive literature review, and introduces the total/scattered field formulation into the FDTD approach. As well, the use of full wave sources for radar cross section predictions and human body dosimetry problems is discussed. Other hybrid numerical methods that have been used to tackle similar problems are then outlined. Finally an examination of spherical waves and FDTD in spherical coordinates is presented.

Chapter 3 explains the models and methods used in the development of this report. The fundamental FDTD method is briefly outlined with reference to a more detailed description in Appendix A. The implementation of plane waves as sources in the total/scattered field formulation is formally discussed, followed by a description of the human body model used in some examples.

Chapter 4 details the development of modifications to the existing FDTD code for the case of low frequency line-sources. The theory and implementation surrounding the method are summarized, with more details and verification in Appendix B. Finally, an example of an application for the method is shown for the human body model close to such a line-source.

Chapter 5 presents the development of an analogy to the uniform plane wave source in the form of spherical waves as sources for the FDTD method. The implementation of

this spherical wave FDTD method is detailed by describing the theoretical development and finite difference formulation.

Chapter 6 provides insight into the numerical issues faced in implementing the method described in Chapter 5. The stability and dispersion properties of the method are developed, along with a discussion on the implications. Numerical boundary conditions for the method are briefly described.

In Chapter 7 initial validation of the method is presented by comparing some simple test cases with analytic solutions. These consist of a spherical resonator, an elementary dipole, and a more complicated, multi-mode case. Finally, a comparison is made to gauge the computer resource savings incurred in using the method for a relatively simple case study.

Conclusions and directions for future research are given in Chapter 8.

Chapter 2

Literature Review

Any numerical method used to investigate EM problems must have some methodology for injection of sources, which are the generators of EM waves. Sources can take a multitude of forms analytically, be it as electric or magnetic current densities, voltage across a gap, or even the direct specification of electric or magnetic fields. There are as many different and distinct ways of specifying sources as different numerical methods. In any excitation method, the goal is to realize the source in as efficient a manner as possible. In general, this means using as few field components as possible (or the analogous voltage/current), and preferably having the source localized in space. The reason for this is to minimize the computer storage requirements and the running time needed to simulate the entire source function.

For sources localized in space, efficient realization has not been problematic. As an example, for a radiating linear dipole the feed point is simulated as an open gap where the voltage source is specified. Since the gap is usually only a couple of grid cells in size

at most, it is an extremely simple manner to initiate the source function numerically. For most frequency domain methods, the source is specified as a vector on the surface of the radiating structure (e.g. wire antenna, aperture, coaxial line).

Remembering that one of the early motivations for numerical methods in electromagnetics was for RCS evaluation, it follows that one of the earliest sources required was a linearly polarized plane wave propagating in free space. This type of source differs from those above since it is not localized: it is of infinite extent, and exists throughout most of the computational volume. One of the early problems was how to implement a plane wave in as efficient a manner as possible. The answer came straight from electromagnetic fundamentals: volume sources can be replaced by an equivalent representation of surface sources. This *equivalence principle* was outlined previously in Chapter 1.

In this research, sources for the FDTD method are of particular interest, so we will begin with a short discussion of an efficient scheme for excitation of uniform plane waves, and the areas of research spurred by this development. The fundamentals underlying efficient plane wave sources provided the basis for development of hybrid methods, which are discussed next. Finally, the focus will change to briefly examine classification of radiating fields by other mathematical methods, and how this opens the possibility of non-localized sources alternative to the uniform plane wave in FDTD.

2.1 Total/Scattered Formulation in FDTD for Plane Waves

The uniform plane wave formulation in the FDTD method was actually introduced in Yee's original paper [1]. This source was very useful for modeling radar scattering,

because the target is usually in the far-field of the radar so that the EM illumination could be considered a plane wave. Yee's approach was to specify *all* the electric and magnetic field values throughout the computational domain for the incident plane wave. The limitations imposed by this approach were that it was a non-compact source (increasing computer requirements), and the outer computational boundaries introduced distortion of the field.

One of the first attempts to mitigate the prohibition imposed by excessive computer requirements was the *hard source* developed by Taflove [4]. The hard source would explicitly force the field at one or several grid locations at each time-step, according to the source function desired e.g. sinusoid, Gaussian pulse, frequency shifted Gaussian pulse, etc. The explicit time-stepping nature of FDTD would then propagate the source fields as time progressed. This gave the desired compact source, but introduced the new problem of retro-reflection of non-physical fields from the hard source. Simulations utilizing hard sources must then be limited in time to avoid retro-reflection, limiting the scenarios that can be modeled.

Finally in 1982, continued attempts to realize compact full-wave sources led to the total/scattered field formulation [5, 6], which has become the method of choice for all modeling requiring plane wave sources. The computational domain is separated into a total field region and a scattered field region, separated by a virtual surface where the equivalence principle is implemented for sources. By this separation, parameters of interest are easily recovered (such as the scattered field for RCS evaluation), and sources can be implemented in a far simpler and more efficient manner. The rapid development of absorbing boundary conditions to simulate the open problem also helped spur the success of the total/scattered

field formulation. Features of the total/scattered field formulation are: i) an arbitrary incident wave direction; ii) simple programming of interacting structures; iii) a wide dynamic range; iv) the development of absorbing boundary conditions; and v) extrapolation of a far-field response [2].

2.1.1 Radar Cross Section

The original FDTD algorithm from Yee [1] was developed for application to RCS evaluation, and, since that seminal paper, one of the primary applications of the method has been to such problems. Other groups that have used the FDTD method for RCS evaluation include Kunz et al. [7, 8], Holland [9], Merewether et al. [10, 11], Taflove and Umashankar and coworkers [5, 12, 13, 14], and an early paper by Taylor et al. [15].

One of the drawbacks of the original Yee grid in its rectangular form is that it implicitly produces staircased approximations to object edges that do not conform to the grid. Staircasing can lead to significant errors for certain problems, or may tax computer requirements by demanding finer meshing in areas requiring detail. Techniques to overcome this difficulty include sub-gridding of finer detail in certain sub-domains [16, 17, 18], and subcellular techniques that modify update equations near fine detail [19, 20]. An alternate approach has been to recast Maxwell's equations to a conformal grid that follows the object outline everywhere, first introduced by Holland [21].

2.1.2 Human Body Dosimetry

Early in the development of numerical methods for EM problems, predictive models for absorption by biological tissue were based almost exclusively on frequency domain

moment methods [22, 23]. But the familiar problems of large, dense matrices restricted the problem size that could be attacked. As a result, the level of resolution attainable with moment methods was not adequate for the problems at hand. But in 1975, Taflove successfully used the FDTD method to study induced fields and currents in the human eye [4], with a model size of 14,000 cells. From that time on, the FDTD method became the method of choice for biological problems because of its affinity to large, heterogeneous structures.

Since then, the FDTD method has been used for full-body exposure analysis of the human body [24], and many other medical applications. The areas of application can be divided into two main categories: the design of therapeutic exposure systems, and the assessment of safety for exposure to EM fields. For the former, earlier examples include FDTD modeling of methods and systems for treatment planning of hyperthermia cancer therapy [25, 26, 27, 28, 29, 30, 31, 32]. In these applications, the FDTD method is utilized in both the design of the therapeutic device, and in the prediction of necessary the heating patterns.

For safety assessment applications, concern always centres around the mass normalized EM energy specific absorption rate (SAR) that must not be exceeded for EM exposure. Considering the safety standard, research with the FDTD method has investigated a variety of problems ranging from standard far-field studies, and to near-field predictions, e.g. cell phones next to the user's head. Published reports on the potential hazards of power lines have also spurred interest in low frequency dosimetry. The advent of efficient numerical techniques, and the associated development of highly detailed anatomically based

models of the human body, have pushed bioelectromagnetic research methods with FDTD to the forefront.

Dosimetry research with the FDTD method began with far-field investigations, where the body or a portion thereof was illuminated with a plane wave. For instance, Chen and Gandhi examined induced currents in the human body from electromagnetic pulses (EMP) generators [33]. Investigations for portable phone users began with Dimbylow and Gandhi, where they used the simplification of a plane wave in the 600 MHz - 3 GHz range [34].

It is useful to briefly divert from full wave sources here to indicate research directions in safety assessment with the FDTD method. Plane waves are not an accurate enough representation of the fields from a mobile phone close to the user's head, for example, and thus researchers have had to include the phone in computations to properly model the near-field interactions. There has been a dearth of publications involving these types of studies, in which the FDTD method played a prolific role [35, 36, 37, 38, 39, 40, 41]. These studies have either focussed on exposure evaluation for existing phone designs, or the investigation of alternative antenna designs to minimize power deposition in the user's head.

Modeling near-field phone interactions is not a difficult task, because including the phone in the computational domain does not increase the computer resources substantially. But for situations such as low frequency power line interactions, it is impossible to explicitly model the entire power line in the domain. Until recently, researchers had to revert to far-field (plane wave) approximations. Another problem with the FDTD method in particular

is that it is not well suited in its original form at low frequencies, because simulating several periods of the source becomes impractical. But innovative modifications to the FDTD method have extended its applicability to the quasi-static region. Gandhi and Chen provided a low frequency FDTD method for human body dosimetry by taking advantage of the linear properties of the material parameters in the low frequency region [42]. This allows computations to be performed at the highest frequency in the quasi-static region, and then scaled back to the frequency of interest. Another method was proposed by De Moerloose et al. whereby the sinusoidal plane wave is approximated by a ramp function [43]. Taking advantage of the derivative relation between internal and external fields of a good conductor, a quasi-static computation can be performed in far fewer time steps.

As has been shown, the application of the total/scattered FDTD method to biological problems has been extensive, and the requirement for near-field analysis has also been demonstrated. However, previous near-field analyses have either been performed with inclusion of the source, or have ignored the characteristics of the actual source altogether by approximating it by a plane wave. Power frequency studies of exposure to the electric field are a prime example of this work. To date a uniform plane wave has been assumed; but if the power line is close to the body of interest, then the fields are no longer uniform. The question then arises as to how to model these situations in the FDTD method.

2.2 Hybrid Methods

As mentioned before, two main problems occur for near-field studies when the source and scatterer are included in the same computational domain. First, a large com-

putational overhead of "free space" is incurred in these cases, as the transmitted wave is propagated explicitly. Second, the fine mesh requirements of the source or scatterer can tax computer resources. One approach to address such problems has been to combine the benefits of two or more methods in a hybridized scheme. These hybrids can be loosely grouped as field equivalence hybrids, and modal hybrids.

2.2.1 Field Equivalence Hybrids

Hybrids in this category rely on the field equivalence theorem to link two methods. Usually the radiating source field is solved using some other method than the FDTD, and the source is surrounded by a fictitious surface on which a field equivalence is constructed; the scatterer is also surrounded by an equivalence surface. The two (or more) regions are coupled together via appropriate field transformations. In the past, the FDTD method has been combined with moment methods [44, 45, 46, 47, 48], spectral methods in periodic structures [49], ray tracing [50], physical optics (PO) [51], the boundary integral equation (BIE) [52], Green's theorem in the time domain [53], and the uniform theory of diffraction (UTD) [54]. The equivalence principle has even been exploited by dividing a total FDTD interaction domain into multiple sub-domains that are coupled through field transformations [55], effectively removing the free space between interacting elements. Alternatively, propagation in the free space region can be performed by a FDTD approximation to the scalar wave equation [56], or the vector wave equation [57], as the problem configuration permits.

In each of these methods, reductions in necessary computational resources are the net gain, and substantial time savings can be accomplished. The drawbacks are that the

source is still modeled concurrently and, except in the last two cases (FDTD approximation to the scalar or vector wave equation), computations are restricted to narrow-band observations. Also, some sources may be exceedingly complex to model with any method; some complicated structures may still require substantial computer resources for effective source representation.

2.2.2 Modal Hybrids

When problems of interest involve the analysis of guided wave structures, it is useful to exploit the known modal field configurations in homogeneous sections of the guiding structure. Mrozowski first explored this concept by analyzing the general case of inhomogeneities in guided wave structures [58, 59], and how function expansion algorithms can be utilized to build iterative matrix schemes analogous to an FDTD scheme. Building on this idea, he showed how to combine one function expansion algorithm - the partial eigenfunction expansion (PEE) - with FDTD to accelerate computations in a rectangular waveguide [60]. In the PEE, function expansion into modes is done in the transverse coordinates, and the third space coordinate along with time are discretized (effectively a 1-dimensional FDTD scheme for each mode). This is used in the homogeneous sections of the waveguide, and coupling proceeds to full FDTD for heterogeneous sections. A similar method was subsequently used by Alimenti et al. [61]. Mrozowski et al. further extended the method to cylindrical guiding structures [62].

The efficacy in modal methods is achieved because of the geometry of the supporting structure (the waveguide), which immediately reduces the necessary field expansion to a finite number of discrete modes. On the other hand, for problems in free space involving

radiation without a guiding structure, any analogy with the modal expansion methods leads to a continuous spectrum of modes. The efficacy is lost because of the number of modes required for accurate representation of the radiated fields. One solution may lie in describing the geometry in spherical coordinates: even in free space the transverse boundary conditions are periodic, leading to discrete modal solutions. This will be of fundamental importance in the development of a portion of this thesis.

2.3 Spherical Waves

Using separation of variables in rectangular or cylindrical coordinates, solutions to Maxwell's equations in free space lead to a continuous spectrum of modes. But even for an unbounded region such as free space, the solution in spherical coordinates leads to discrete modal solutions termed *spherical waves*. Stratton [3] provides a fundamental treatise on the mathematical properties of spherical waves, and a discussion of the interpretation and application of spherical waves in EM radiation problems is well summarized in [63]. One property of a spherical wave expansion is that, in general, the number of modes for a certain degree of accuracy is far fewer than in rectangular or cylindrical modes. These properties make spherical waves particularly useful for finite sources radiating into unbounded regions.

Furthermore, spherical wave expansions are often used to classify antennas on test ranges, as spherical scanning is used in compact ranges to obtain near-field radiation patterns. The implication here is that a given antenna may be used as a source in an FDTD computation simply by using its spherical wave expansion. Also, spherical waves are inherently well-suited to near-field studies.

2.4 FDTD in Spherical Coordinates

Assuming that spherical wave expansions are a valid avenue to explore for integration with FDTD, it is useful to ask what techniques exist for the FDTD method in spherical coordinates. The first FDTD code in spherical coordinates was developed by Holland [64], and since that time most of the research surrounding the topic has been in the area of developing proper absorbing boundary conditions (ABC). The sparsity of research in the utilization of this technique may be due to the lack of a proper ABC. Another explanation is the inherent geometry problems: for a given elevation and azimuthal step size, at increasing radius a unit cell becomes increasingly larger in size. This results in a decline in resolution at the outer edges of the domain. In fact, soon after Holland's paper, many articles appeared that developed the FDTD method in generalized curvilinear coordinates [21], and the curvilinear method is still a method that continues to be an area of active research and development.

2.5 Conclusions

This chapter outlined how the total/scattered field formulation was the first method developed that allowed for volume source distributions to be initiated efficiently. Based fundamentally on the equivalence principle, incident fields need only be explicitly set on a two dimensional surface as opposed to over the entire volume in three dimensions. But to date, efficient methods of specifying the source have only been exploited by using the plane wave source of Taflove, which effectively models far-field situations. As a corollary, the plane wave method in the total/scattered field formulation was also enhanced to investigate

low frequency quasi-static problems.

One low frequency problem of interest is the examination of exposure levels for humans close to power lines, where research has focussed on solving the problem without incorporating the power line explicitly. This has effectively meant modeling in the far-field with a uniform plane wave. There is still a requirement to examine electric field exposure levels when the power line is close to, e.g. a worker. Such scenarios exist in electric power substations, where high voltage equipment and lines can not be shut down because of service requirements. The total/scattered field formulation and the equivalence principle provide the necessary stepping stones to investigate efficient methods to attack this problem, which will be the starting point in the development of this thesis.

Another way of taking advantage of the equivalence principle has been to use hybrid techniques. By combining the best features of different methods in different regions, difficult problems have become feasible by reducing numerical complexity. But the hybrid methods to date still require the source to be modeled explicitly in one sub-domain, and are frequently restricted to narrowband applications due to limitations in one of the hybridized techniques. Also, moment method applications integrated with the FDTD can place excessive memory demands to store the time history of signals. Modal methods can eliminate narrowband restrictions or storage demands, but are limited in application to waveguide structures. Furthermore, a significant number of modes is usually required to accurately depict a given source configuration.

From the limitations discussed for equivalence principle methods, an attractive technique for general application would need to combine several features:

- the use of an explicit time-domain algorithm (eliminating most storage requirements);
- the elimination of the requirement to concurrently model the source;
- no restriction to a waveguiding structure; and
- a reduced number of modes.

It appears that spherical waves offer most, if not all, of the features required. Although somewhat complicated conceptually, they offer a reduced number of modes and inherent near-field modeling. Furthermore, free space is actually a waveguiding structure due to periodic and radiation boundary conditions. Finally, a source can be effectively represented by far fewer modes with spherical waves than with plane or cylindrical waves.

It still needs to be shown that other analytic sources can be efficiently incorporated on the equivalence surface in the total/scattered FDTD method in view of the complications introduced by spherical waves. So to start the total/scattered field formulation will be augmented, then a method for efficient modeling of humans close to line sources will be demonstrated, and finally a general method for any near-field analysis using spherical waves will be presented.

Chapter 3

Models and Methods

Before investigating modifications to the FDTD method to allow for efficient near-field modeling, additional discussion follows regarding some of the concepts elucidated upon in the previous chapters. Appendix A outlines the FDTD method and some of the salient features relevant to the discussion for this thesis. These involve the stability analysis of a simple Cartesian FDTD scheme, a general discussion on the types of boundary conditions needed for certain types of problems, and material modeling issues. Also a general discussion on the quasi-static FDTD method is presented which is valuable in understanding low frequency modeling with FDTD, and particularly for power line exposure modeling.

This chapter begins with the FDTD fundamental developments that led to the efficient uniform plane-wave model. Particular interest lies in problems involving the exposure of humans to electromagnetic energy in the near-field. Therefore, the human body model used is briefly outlined.

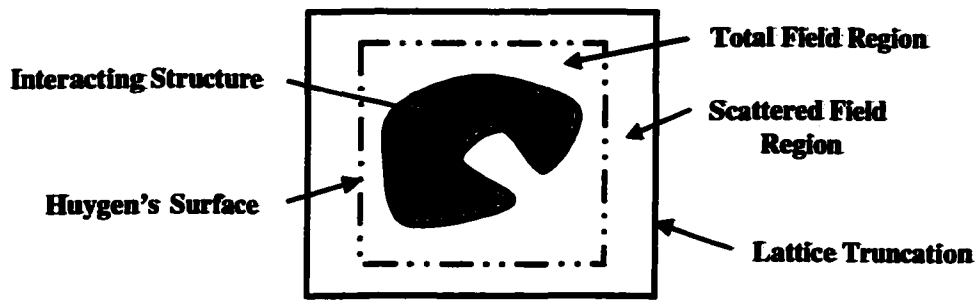

Figure 3.1: Diagram of the total/scattered field formulation.

3.1 Plane Waves and the Total/Scattered Field Formulation

The basis of the total/scattered field formulation introduced by Taflove [2] is the equivalence principle. In this formulation, splitting the computational domain into two regions (Figure 3.1) separated by a Huygens' surface modifies the standard Yee algorithm [1]. Inside this closed surface the updated field values are still total fields, but outside the surface there are only scattered fields. By specifying the initial field values for the entire domain (usually zero), the tangential electric or magnetic field vectors at the Huygens' surface for all $t > 0$ can be specified, thus uniquely determining domain field values for all times $t > 0$.

The Huygens' surface field values can be decomposed into a scattered field component and an incident field component. The incident field values are derived from the source function. In the previously derived uniform plane wave source [2], the fields are uniquely specified by three fixed angles (ϕ, θ, ψ) which define the direction of propagation and the polarization of the electric field vector with respect to that direction. The angles ϕ and θ are the standard spherical coordinates (azimuth and elevation). The reference direction

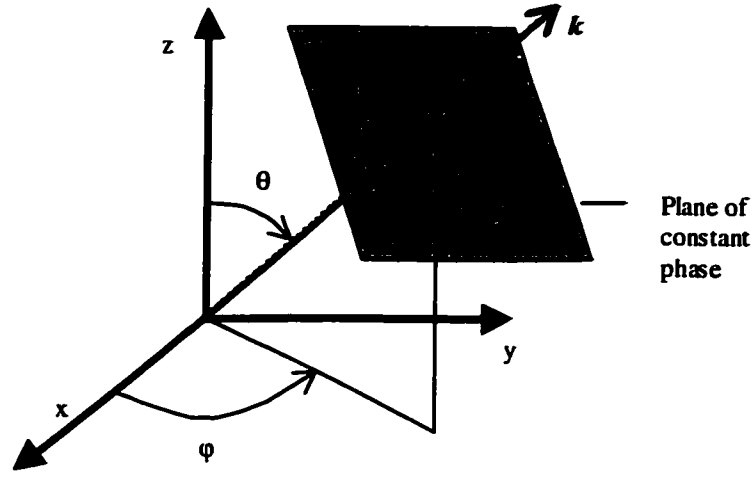

Figure 3.2: Definition of angles for the incident uniform plane wave.

for ψ is the vector $\vec{e} = \vec{k} \times \vec{z}$ where $\vec{k}$ is the incident wave vector direction, and ψ is measured clockwise (when looking towards the source) from the reference. This defines the electric field polarization on the transverse plane, as illustrated in Figure 3.2.

For the uniform plane wave formulation [2], a computationally efficient way to specify the incident wave components is through the use of an alternate one-dimensional source grid valid for propagation directions defined by the angles (ϕ, θ, ψ). Incident electric and magnetic field values on the Huygens' surface are then specified by interpolation of the field value in the source grid, and implementation of appropriate connecting conditions. These connecting conditions are the Yee update equations, modified to incorporate an incident field component and a scattered field component.

The incident field vectors lie in planes transverse to the direction of propagation, at distances d along the source grid. Hence the incident fields must be transformed to Cartesian coordinates to be consistent with the Yee grid. The intersection of the Huygens'

surface and these planes define contours on which, for a uniform plane wave, all electric and magnetic fields are identical. The appropriate equations as connecting conditions for a uniform plane wave are [2]:

$$H_{x,inc}|_d^n = H_{inc}|_d^n \times (\sin\psi \sin\phi + \cos\psi \cos\theta \cos\phi) \quad (3.1a)$$

$$H_{y,inc}|_d^n = H_{inc}|_d^n \times (-\sin\psi \cos\phi + \cos\psi \cos\theta \sin\phi) \quad (3.1b)$$

$$H_{z,inc}|_d^n = H_{inc}|_d^n \times (-\cos\psi \sin\theta) \quad (3.1c)$$

$$E_{x,inc}|_d^n = E_{inc}|_d^n \times (\cos\psi \sin\phi - \sin\psi \cos\theta \cos\phi) \quad (3.1d)$$

$$E_{y,inc}|_d^n = E_{inc}|_d^n \times (-\cos\psi \cos\phi - \sin\psi \cos\theta \sin\phi) \quad (3.1e)$$

$$E_{z,inc}|_d^n = E_{inc}|_d^n \times (\sin\psi \sin\theta) \quad (3.1f)$$

where $H_{inc}|_d^n$ and $E_{inc}|_d^n$ are the incident magnetic or electric field respectively, at a distance d along the source grid, and at timestep n. For this uniform plane wave implementation the angles are *fixed* for *all* locations on the Huygens' surface.

3.2 Human Body Model

A model of the human body has been developed in the Bioelectromagnetics lab at the University of Victoria based on magnetic resonance images (MRI) obtained from the Yale Medical School [65]. The original model consisted of head and torso data, which was completed by adding arms and legs based on representations obtained by applying segmentation algorithms to computer tomography (CT) and MRI data from the Visible Human Project at the U.S. National Library of Medicine (http://www.nlm.nih.gov/research/visible/ visible_human.html). The final body model is 1.77 m tall, and has a mass of approximately

76 kg. The resolution of the models is 3.6 mm in each Cartesian direction, with the x, y, and z axes directed from left-to-right, back-to-front, and head-to-foot, respectively.

Chapter 4

Low Frequency Line-Source

In its classical form, the FDTD is not a very attractive method at low frequencies. The required simulation times may be prohibitively long even for moderate spatial resolution. However, at sufficiently low frequencies, and for suitable object dimensions and electrical properties, the quasi-static FDTD formulation [43] overcomes that problem (described in Appendix A). This formulation holds for quasi-static conditions, where the wavelength and skin depth are much greater than the size of the structure under consideration. It is also assumed that parts of the structure can be represented either as good conductors or good dielectrics. The structure itself can be heterogeneous, but in any given part either the conduction or displacement current has to dominate, to the extent that the other current component can be neglected (preferably it is below 0.1%). Under these conditions, the fields in the conductors are proportional to the time derivative of the incident field, and in the dielectrics follow the applied field temporal behavior. The field response needs to be computed separately for the electric and magnetic field. In practice, at low

frequencies, the response for one field only is of interest anyway. By creating a standing wave condition, electric or magnetic field exposure can be studied in isolation.

For plane wave excitations with a ramp function, accurate results can be extracted immediately after the transient response has decayed, typically after 1000-4000 time steps [43] (i.e. a fraction of the signal period). A properly designed perfectly matched layer (PML), originated by Berenger [66], provides efficient low reflection termination of the computational space for this type of problem [67, 68, 69].

The quasi-static formulation of the FDTD was developed for evaluation of electric fields induced in the human body from exposure to powerline frequency (50 Hz or 60 Hz) uniform electric fields. The computations had to be performed with high resolution to identify organs that might have higher fields than the average. Thus the resolution used in the FDTD was 7.2 mm [43]. When the FDTD was hybridized with an efficient finite difference (FD) code, resolution of 3.6 mm was easily achieved with high accuracy [70]. In some occupational situations, such as those in electric utility substations, workers on the ground are too close to high voltage conductors for the exposure fields to be assumed to be uniform.

Although the total/scattered field formulation has so far been utilized for uniform plane wave excitation only, there is no reason why it can not be extended to other excitations for which analytic solutions exist. In this chapter, the solution for an infinite line-source at an arbitrary distance and orientation is provided. This modification to the FDTD program is important, since it allows for the prediction of fields and currents induced in utility workers in close proximity to powerlines. This in turn gives a more accurate estimation

of the hazards they are exposed to on a daily basis. The theory and implementation of the new algorithm are outlined, with comprehensive validation of the algorithm provided in Appendix B. This includes comparisons with analytic solutions for a homogeneous lossy sphere in proximity to a current-carrying infinite conductor, or an infinitely long line of uniformly distributed charge. At the end of this chapter, results are given for a high resolution heterogeneous model of the human body under a line-source for electric field exposure (exposure to non-uniform magnetic fields can be more efficiently evaluated by FD methods [71]).

4.1 Implementation

For an infinite line of charge or current at a low frequency, the fields have a cylindrical TEM configuration. On a plane perpendicular to the line, electric fields are radial and magnetic fields are circumferential, with magnitudes inversely proportional to the distance from the line. These fields are thus transverse planar with their polarization dependent on their point in space with respect to the line. This immediately suggests how to modify the equations (3.1) to reflect this cylindrical TEM configuration. The source field values for the Huygens' surface are still transformed using (3.1), with the modification that the angle ψ is dependent on the distance vector $\vec{\mathbf{d}}$ between that point in space and the line: $\psi = \psi(\vec{\mathbf{d}})$. The TEM field $\vec{\mathbf{F}}$, where $\vec{\mathbf{F}}$ represents either the magnetic or electric field, can then be represented as:

$$\vec{\mathbf{F}} = \frac{1}{\left|\vec{\mathbf{d}}\right|} \vec{\mathbf{F}} \left(\psi(\vec{\mathbf{d}})\right) \tag{4.1}$$

Without loss of generality, it can be assumed that the infinite line-source is oriented

parallel to the x-axis, and passing through the point (yh, zh). Then for any point on the Huygens' surface (x, y, z), to specify the incident field value, the scale factor is found as:

$$\left|\vec{\mathbf{d}}\right| = \sqrt{(z - zh)^2 + (y - yh)^2} \tag{4.2}$$

Also, to resolve the fields into the three Cartesian components, the equations (3.1) still hold, with the modification that the angle ψ is:

$$\psi(y, z; yh, zh) = \begin{cases} \arctan\left(\frac{z-zh}{y-yh}\right) & \vec{\mathbf{k}} = -\hat{\mathbf{x}} \\ \arctan\left(\frac{z-zh}{yh-y}\right) & \vec{\mathbf{k}} = +\hat{\mathbf{x}} \end{cases} \tag{4.3}$$

depending on the direction of the source wave. This is visualized in Figure 4.1 for a yz-plane ($x = a$) perpendicular to the direction of propagation, with (yh, zh) being the origin. For this case, the source wave is travelling in the positive x-direction, and so the reference direction for polarization is the negative y-direction ($\vec{\mathbf{k}} \times \hat{\mathbf{z}} = \hat{\mathbf{x}} \times \hat{\mathbf{z}} = -\hat{\mathbf{y}}$). Note that a mutually perpendicular vector couplet of the electric and magnetic fields for a given point in space rotates through the angle ψ with the distance vector.

A standard FDTD code has been modified to implement this line-source. It is a simple procedure to modify the standard plane wave source implementation to allow for such a case. In this case, the angle ψ is no longer fixed for all points on the Huygens' surface, but changes depending on the point location with respect to the line.

This method has been fully validated by comparing the fields in a computational free space to the analytic solution, and for the case of a homogeneous lossy sphere near a line of charge or line of current for which analytic solutions exist as well. The details of this validation are presented in [72] and Appendix B.

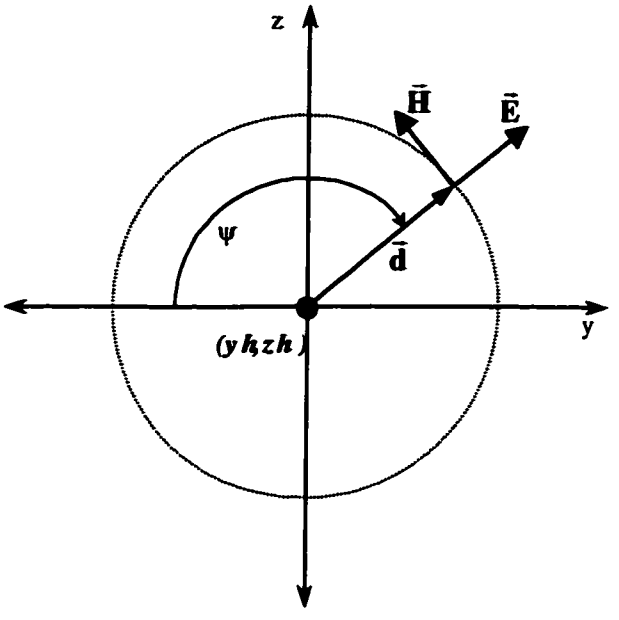

Figure 4.1: Visualization for the polarization angle ψ for a source wave (from a line-source) in the $\hat{x}$ direction. Note the orientation of the vector couplet.

4.2 Example of Application - Human Body Dosimetry

The quasi-static FDTD method with a line-source can be used to compute induced electric fields and currents in the human body close to high-voltage transmission lines, where the incident electric field can no longer be considered uniform. The heterogeneous model of the human body used is based on MRI scans. The various organs and tissues were assigned conductivity ranging from 0.01 to 2.2 $\mathrm{S/m}$, based on the most recent measurements. Detailed conductivity values are given in [73]. Since the displacement current is negligible, relative permittivity values were set to 1 for all material types.

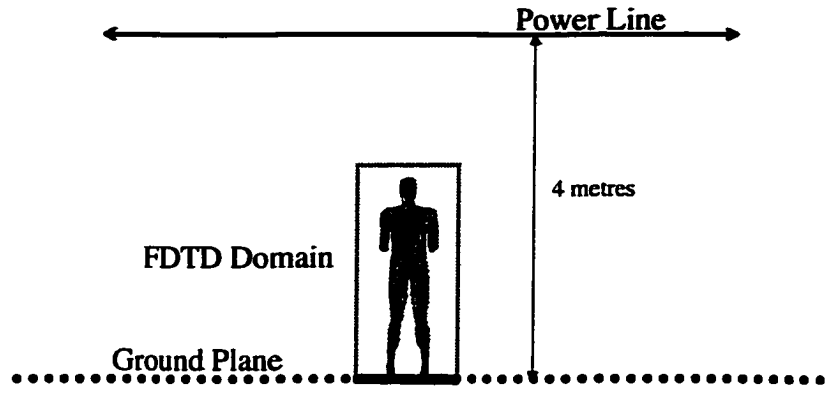

Figure 4.2: Geometry for example problem - a worker standing on a ground plane near a conducting powerline

4.2.1 Geometry of the Problem

The geometry of the problem is sketched in figure 4.2. The body model and the bounding box encompassing it were placed in contact with a perfect ground plane. The remaining five sides were surrounded by four layers of free space cells, and PMLs (15, P, 40dB). This led to an overall computational domain of $114 \times 83 \times 264 = 2,497,968$ voxels at 7.2 mm resolution. In order to initiate the proper analytic fields in the computational domains, four line-source functions had to be initiated: two for each of the real and image source (as a result of the ground plane). As noted previously, two sources create the standing wave condition for the electric field excitation. The source functions simulated source (image) lines located 4 m above (below) the ground plane, oriented parallel to the x-axis, and centered over the domain. The parameters of the functions were chosen to represent a 60 Hz field with a magnitude of 1 kV / m at the ground plane directly underneath the line. All results presented scale linearly with amplitude and with frequency up to 100 kHz [43].

Table 4.1: Organ Dosimetry for Electric Induction from 60 Hz line-source at 4m over a perfect ground plane

Organ	$\|E\|_{max}$ (mV/m)		$\|J\|_{max}$ (mA/m)		$\|E\|_{avg}$ (mV/m)		$\|J\|_{avg}$ (mA/m)	
	line-source	Uniform	line-source	Uniform	line-source	Uniform	line-source	Uniform
bowels	3.74	3.20	1.27	1.36	1.18	0.946	0.374	0.305
brain	4.45	2.82	0.445	0.282	1.21	0.869	0.101	0.0727
brain - gray	4.45	2.82	0.445	0.282	1.14	0.828	0.114	0.0828
brain -white	2.80	2.22	0.168	0.133	1.32	0.940	0.0790	0.0564
heart	3.18	2.19	0.318	0.219	1.49	1.07	0.149	0.107
kidneys	2.75	2.43	0.275	0.242	1.38	1.03	0.138	0.103
liver	4.07	2.69	0.285	0.188	1.76	1.26	0.123	0.0884
lungs	3.23	2.30	0.259	0.184	1.36	1.01	0.108	0.0805
muscle	27.6	23.5	9.65	8.21	1.47	1.32	0.515	0.462
prostate	2.23	2.26	0.893	0.904	1.49	1.47	0.596	0.589
spinal cord	3.55	2.23	0.355	0.223	1.29	1.08	0.129	0.108
spleen	3.48	2.29	0.348	0.229	1.74	1.36	0.174	0.136
stomach	1.63	1.33	0.815	0.666	0.854	0.684	0.427	0.342
thyroid	1.14	0.962	0.572	0.481	0.911	0.819	0.456	0.410
whole body	75.2	48.1	12.01	11.5	2.031	1.70	0.349	0.309

4.2.2 Results and Discussion

Steady state for this problem was reached after 8000 timesteps. The induced electric fields at the end of the simulation were the data of interest, and were analyzed as follows. First, organ dosimetry data in terms of the induced electric field and current density maximums and averages for organs of interest were determined. Subsequently these data were compared with comprehensive organ dosimetry obtained previously in the case of a uniform 1 kV/m field. Most of the organs chosen were those whose ratio of surface area to volume were suitable for analysis, given that boundary field values are overestimated and may skew data. None of the data was post-processed in the manner discussed in Appendix B (setting tangential surface fields to zero), since it is the internal organs that are of interest. The results are shown in Table 4.1. The uniform field used for comparison is 1 kV/m. All the values for the line-source are higher, by up to 40%, as is expected since the fields in the absence of the object are higher than those of a uniform field.

It is informative to compare the ratio of the induced fields with the line-source to

that of the uniform field, and relate that to the fields that exist in the absence of the body for each source respectively, described as follows. For a particular organ a suitable coordinate location P is identified as an approximate centre of the organ. Then the ratio (R_P) of the field at that location in the absence of the body model, to that of the uniform field strength of 1 kV/m, is computed. Next maximum and average induced electric field values in the organ for the line-source exposure and the uniform field exposure are compared, and two other ratios OR_a and OR_m are constructed, representing the ratios for the organ average and maximum values. Finally, these organ ratios are compared to the exposure field ratio R_P. The steps are thus as follows:

1. determine an organ midpoint, P;
2. at P, find the free-space field for the line-source $E_l(P)$;
3. determine the free-space ratio $R_P = \frac{E_l(P)}{1000\,\mathrm{V/m}}$;
4. determine organ ratios for maximum and average induced electric fields OR_m and OR_a; and
5. compare organ ratios with free-space ratios R_P.

The results of this process are tabulated in Table 4.2. This process is informative because the results obviously show that the induced field ratios are much larger than the free space ratio at the position of every organ of interest. While the free space ratio R_P ranges from 108-120%, the organ ratios for both the average and maximum induced fields are higher, ranging from 116%-160%.

Table 4.2: Ratios of Electric Fields induced by a line-source to those of a uniform field, along with the free-space ratio R_p

Organ	R_P	OR_a	OR_m
bowels	1.084	1.249	1.169
brain	1.218	1.389	1.578
brain- gray matter	1.218	1.380	1.578
brain - white matter	1.218	1.401	1.263
heart	1.125	1.391	1.451
kidneys	1.097	1.344	1.130
liver	1.106	1.398	1.511
lungs	1.131	1.343	1.405
spleen	1.105	1.280	1.517
stomach	1.106	1.334	1.225

Another parameter of interest is the total vertical current through each layer of the model. These data are illustrated in Figure 4.3, along with the corresponding vertical current previously calculated for a uniform field of 1000 V / m. It is readily evident that the vertical current predicted by exposure to the line-source is greater than that for the uniform field, as is expected since the field at the head from the line-source is approximately 20% higher than that of the uniform field.

Finally it is useful to examine the maximum external electric field, or more importantly the field enhancement factor. The field enhancement factor is a ratio of the external field in the presence of the body to that in the absence of the body. The enhancement factor predicted for the case of a uniform field is 16.8 [70]. For exposure to a line-source, the predicted enhancement factor is 19.0. It should be noted that the maximum external field is likely to be over-predicted (for any type of exposure), because of the staircasing approximation. Indeed, visual inspection of the vertical layer where the maximum field occurs (at the top of the head) shows a "corona" of high field values around the exterior, where a staircase edge occurs. But this error is consistent with and evident in the previous uniform field research as well, since the same staircasing approximation is used.

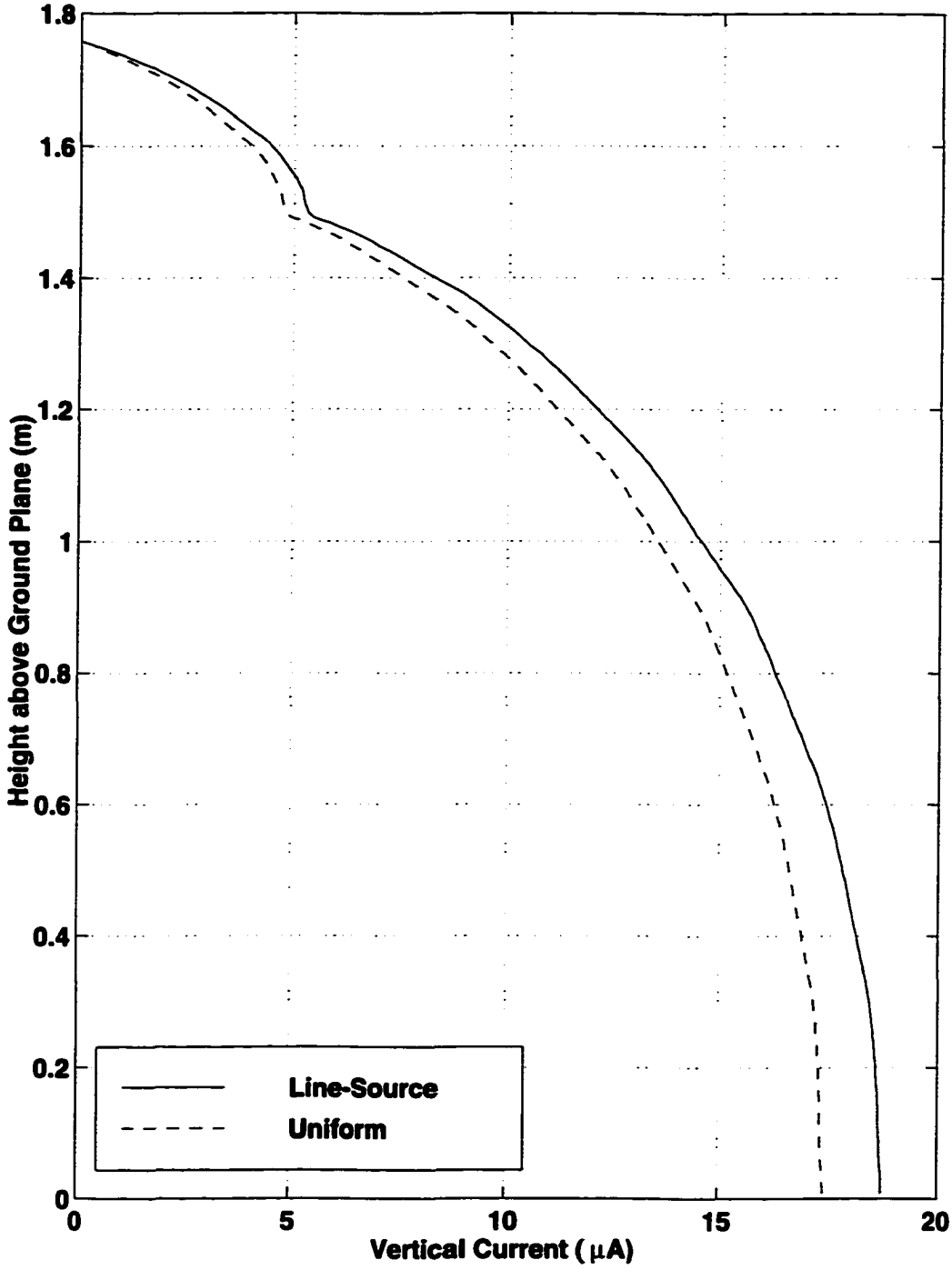

Figure 4.3: Total Vertical Current (as a function of height) of the human model on a ground plane, in an electric field produced by a 60 Hz line-source (1 kV / m at the ground).

4.3 Conclusions

An extension to the total/scattered field formulation of wave excitation in the FDTD has been provided for line-sources with TEM waves. The formulation based on the analytic formulation of the incident field is rather straightforward, and is of high accuracy even for a coarse mesh. This formulation has been used in the recently developed quasi-static FDTD method. A verification of the method against an analytic solution for a conductive sphere in the proximity of a line-source attests to its high accuracy. Finally, the combination of the new non-uniform source formulation and the quasi-static FDTD provides an effective tool for computations of induced electric fields and currents in the human body in close proximity to high voltage transmission lines. Such situations occur in some locations in the electric utility industries, and an accurate evaluation of fields in the body is of importance, particularly for persons with medical devices, e.g. cardiac pacemakers.

More importantly, it has been shown that the equivalence principle and the total/scattered field formulation allow for the efficient realization of sources other than the uniform plane wave. In this particular case, simple modifications to the existing algorithm produced a method to model near-field effects close to line-sources without having to explicitly model the source. The next direction of investigation is to tackle more general problems in the near-field of sources with a method of comparable efficiency.

Chapter 5

Spherical Wave Sources

In the previous chapter, it was demonstrated that a particular near-field situation (a line-source) can be efficiently modeled with only small modifications to the total/scattered field formulation method. But the equivalence principle does not exclude more general types of sources. Using separation of variables in rectangular or cylindrical coordinates, solutions to Maxwell's equations in free space lead to a continuous spectrum of modes. But even for an unbounded region such as free space, the solution in spherical coordinates leads to discrete modal solutions termed spherical waves. Details of spherical wave theory can be found in [74], [3], and [75], and the fundamentals are summarized in Appendix D. One property of a spherical wave expansion is that the number of modes required for a certain degree of accuracy is far less than for rectangular or cylindrical modes. These properties make them particularly useful for finite sources radiating into unbounded regions.

Furthermore, spherical wave expansions are often used to classify antennas on test ranges because spherical scanning in an indoor range allows for near-field scanning

techniques. The implication here is that a given antenna may be used as a source in an FDTD computation simply by using its spherical wave expansion, and that representation is inherently well-suited to near-field studies.

In the next chapters the *efficient* implementation of spherical waves as sources in the FDTD is detailed, by describing a method whereby a model of a source incorporating spherical waves is implemented in the total/scattered FDTD method. Much like the plane wave sources in the FDTD method, the spherical wave modes are time-stepped on 1-D alternate source grids, representing mode propagation in free space. Spherical wave modes are then interpolated and summed on the Huygens' surface. It is assumed that the object of interest lies no closer than in the radiative near-field of the source, and therefore there is no significant coupling between source and object.

The problem formulation is first outlined in order to draw analogies to the existing uniform plane wave method. The framework of two methods of implementation are then discussed by developing one-dimensional update equations useful for spherical coordinates. Next, the discretization of the spherical wave FDTD (SW-FDTD) methods are developed. In Chapter 6, numerical considerations are outlined, including stability and dispersion analyses of the method. In Chapter 7, validation of the SW-FDTD method is presented by examining test cases that have analytic solutions, and some numerical comparisons are made with other methods.

5.1 Problem Outline

From Appendix D, equations (D.7) and (D.8) show that spherical wave vectors are fixed for a set of points in space $\{r_s, \theta_s, \varphi_s\}$ with an explicit harmonic time-dependence assumed. Consider the set of points $\{r_s, \theta_s, \varphi_s\}$ as those that define the Huygens' surface (an equivalence surface); because all the node locations on the Huygens' surface are known *a priori,* the angular functions can be pre-processed and stored for future use. Calculating the radial and time-dependence are the goal of the explicit part of the SW-FDTD method.

Thus a spherical wave analogy is created to the plane-wave FDTD formulation, only there are separate equations in r and t discretized for each mode. The radial, time-dependent, modal functions - explicitly determined in an FDTD method - are then weighted with angular function values determined in pre-processing. Only N modes need to be calculated because of the cutoff behaviour of spherical waves. The set of weighted mode values can then be summed to determine the total field value at each point $\{r_s, \theta_s, \varphi_s\}$.

The following assumptions are made to implement the outlined method:

1. the origin of the spherical waves is known, and lies outside the total field domain (i.e. exterior to the Huygens' surface);

2. the spherical wave expansion of the source is a known quantity; that is, we have specified our source entirely by pre-determining the spherical wave expansion coefficients of the wave functions $a^{(i)}_{\substack{e \\ o}mn}$ and $b^{(i)}_{\substack{e \\ o}mn}$; and

3. modeling is required beyond the reactive near-field of the source, where no significant coupling exists between source and scatterers (this condition may be relaxed in the

future with further research, which may allow for multiple, coupled domains).

The spherical wave expansion is only valid for the region of space $r > r_0$, where r_0 is the radius of the sphere enclosing the sources for which the spherical wave expansion has been made. Therefore, this entire sphere (and hence the spherical wave origin) must lay outside the computational domain. The coefficients $a^{(i)}_{\substack{e\\o}mn}$ and $b^{(i)}_{\substack{e\\o}mn}$ are weights for each explicit modal function determination.

The next item to consider then is how to implement a finite difference method for the modal equations.

5.2 Implementation

5.2.1 Partial Eigenfunction Expansion

The previous section outlined what is essentially a Partial Eigenfunction Expansion coupled with a Finite Difference Time Domain method (PEE-FDTD). As outlined in Appendix C, this general approach is possible because the field configuration in the transverse direction is known analytically from the problem structure. In the waveguide configuration, the functions are analytic, since there are boundary conditions in the transverse direction (i.e. metallic walls of a waveguide), and hence there are discrete eigenfunctions. Conversely, if the waveguide is unbounded in the transverse directions - i.e. free space - then the mode configuration in the transverse direction can not be stated with certainty, since there are no discrete eigenfunctions. So how can a similar algorithm for free space be constructed?

Consider in the spherical geometry that the analogous structure is a series of

concentric spheres at increasing radii instead of slices in the z-direction; θ and ϕ are the transverse directions. The advantage of the spherical geometry is that the geometry itself has implicit periodic boundary conditions which only permit discrete eigenfunctions (spherical harmonics). This then obviates the necessity in a PEE-FDTD analogy for real, physical, boundary conditions such as the metallic walls of a waveguide. The spherical coordinate system allows for a free-space waveguide. Based on this analogy, it should then be possible to develop radial amplitude functions, that only depend on r and t, for each field component.

5.2.2 Amplitude Functions

As an aid in discussion, Maxwell's curl equations in spherical coordinates, separated by components, are restated:

$$\frac{1}{r\sin\theta}\left[\frac{\partial}{\partial\theta}(\sin\theta E_\varphi)-\frac{\partial E_\theta}{\partial\varphi}\right]+\mu\frac{\partial H_r}{\partial t} = 0 \tag{5.1a}$$

$$\frac{1}{r\sin\theta}\frac{\partial E_r}{\partial\varphi}-\frac{1}{r}\frac{\partial(rE_\varphi)}{\partial r}+\mu\frac{\partial H_\theta}{\partial t} = 0 \tag{5.1b}$$

$$\frac{1}{r}\frac{\partial(rE_\theta)}{\partial r}-\frac{1}{r}\frac{\partial E_\varphi}{\partial\theta}+\mu\frac{\partial H_\varphi}{\partial t} = 0 \tag{5.1c}$$

$$\frac{1}{r\sin\theta}\left[\frac{\partial}{\partial\theta}(\sin\theta H_\varphi)-\frac{\partial H_\theta}{\partial\varphi}\right]-\epsilon\frac{\partial E_r}{\partial t} = 0 \tag{5.1d}$$

$$\frac{1}{r\sin\theta}\frac{\partial H_r}{\partial\varphi}-\frac{1}{r}\frac{\partial(rH_\varphi)}{\partial r}-\epsilon\frac{\partial E_\theta}{\partial t} = 0 \tag{5.1e}$$

$$\frac{1}{r}\frac{\partial(rH_\theta)}{\partial r}-\frac{1}{r}\frac{\partial H_\varphi}{\partial\theta}-\epsilon\frac{\partial E_\varphi}{\partial t} = 0 \tag{5.1f}$$

The analytic solution to these equations is given in Appendix D in terms of spherical wave functions in TE and TM modes, as tabulated in Table 5.1, with

$$u \text{ or } v = e^{j\omega t}z_n^{(i)}(kr)P_n^m(\cos\theta)\begin{matrix}\cos\\ \sin\end{matrix}m\varphi$$

Table 5.1: Analytic Expressions for Modes

Field Component	TE	TM
H_r	$\frac{n(n+1)u}{r}$	0
H_θ	$\frac{1}{r}\frac{\partial}{\partial\theta}\frac{\partial}{\partial r}(ru)$	$\frac{j\omega\epsilon_0}{r\sin\theta}\frac{\partial}{\partial\varphi}(rv)$
H_φ	$\frac{1}{r\sin\theta}\frac{\partial}{\partial\varphi}\frac{\partial}{\partial r}(ru)$	$-\frac{j\omega\epsilon_0}{r}\frac{\partial}{\partial\theta}(rv)$
E_r	0	$\frac{n(n+1)v}{r}$
E_θ	$-\frac{j\omega\mu_0}{r\sin\theta}\frac{\partial}{\partial\varphi}(ru)$	$\frac{1}{r}\frac{\partial}{\partial\theta}\frac{\partial}{\partial r}(rv)$
E_φ	$\frac{j\omega\mu_0}{r}\frac{\partial}{\partial\theta}(ru)$	$\frac{1}{r\sin\theta}\frac{\partial}{\partial\varphi}\frac{\partial}{\partial r}(rv)$

This provides the analogy to the rectangular waveguide field components.

As an analogy with the waveguide PEE method, the form of the transverse functions is known as $Y_{nm}(\theta,\varphi) = P_n^m(\cos\theta)\frac{\cos}{\sin}m\varphi$. However, the form of the functions in Table 5.1 is a hindrance to translation into a FDTD method because the equations are not in the time domain. Radial and time(frequency)-dependence can not be separated because radial functions are functions of the wavenumber and hence frequency.

Instead, for an arbitrary source function, assume a time-domain amplitude function $f_\lambda(r,t)$, with $\lambda \in \{r,\theta,\varphi\}$ and $f \in \{h,e\}$. The field equations resulting from specifying amplitude functions are summarized in Table 5.2. It should be possible to discretize in radius and time only, and to develop one-dimensional modal equations that can be solved by way of an FDTD method.

5.2.3 Initial Implementation

By substituting the expressions from Table 5.2 into (5.1), a set of coupled equations in r and t only is developed. The results are summarized in Table 5.3. Note that there is only one-way coupling of the radial component, so an alternate method of determining the

Table 5.2: Expressions for Modes with amplitude functions

Field Component	TE	TM
H_r	$n(n+1)h_r(r,t)P_n^m(\cos\theta)\begin{matrix}\cos\\\sin\end{matrix}m\varphi$	0
H_θ	$h_\theta(r,t)\frac{\partial P_n^m(\cos\theta)}{\partial\theta}\begin{matrix}\cos\\\sin\end{matrix}m\varphi$	$h_\theta(r,t)\frac{P_n^m(\cos\theta)}{\sin\theta}\begin{matrix}\sin\\\cos\end{matrix}m\varphi$
H_φ	$h_\varphi(r,t)\frac{P_n^m(\cos\theta)}{\sin\theta}\begin{matrix}\sin\\\cos\end{matrix}m\varphi$	$h_\varphi(r,t)\frac{\partial P_n^m(\cos\theta)}{\partial\theta}\begin{matrix}\cos\\\sin\end{matrix}m\varphi$
E_r	0	$n(n+1)e_r(r,t)P_n^m(\cos\theta)\begin{matrix}\cos\\\sin\end{matrix}m\varphi$
E_θ	$e_\theta(r,t)\frac{P_n^m(\cos\theta)}{\sin\theta}\begin{matrix}\sin\\\cos\end{matrix}m\varphi$	$e_\theta(r,t)\frac{\partial P_n^m(\cos\theta)}{\partial\theta}\begin{matrix}\cos\\\sin\end{matrix}m\varphi$
E_φ	$e_\varphi(r,t)\frac{\partial P_n^m(\cos\theta)}{\partial\theta}\begin{matrix}\cos\\\sin\end{matrix}m\varphi$	$e_\varphi(r,t)\frac{P_n^m(\cos\theta)}{\sin\theta}\begin{matrix}\sin\\\cos\end{matrix}m\varphi$

Table 5.3: Expressions for components

TE	TM
$h_\varphi = h_\theta$	$h_r = 0$
$\mu\frac{\partial}{\partial t}h_\theta = \left(\frac{1}{r}+\frac{\partial}{\partial r}\right)e_\varphi$	$\mu\frac{\partial}{\partial t}h_\theta = -\frac{n(n+1)e_r}{r}+\left(\frac{1}{r}+\frac{\partial}{\partial r}\right)e_\varphi$
$\mu\frac{\partial}{\partial t}h_\varphi = -\left(\frac{1}{r}+\frac{\partial}{\partial r}\right)e_\theta$	$\mu\frac{\partial}{\partial t}h_\varphi = \frac{n(n+1)e_r}{r}-\left(\frac{1}{r}+\frac{\partial}{\partial r}\right)e_\theta$
$e_r = 0$	$e_\varphi = e_\theta$
$\epsilon\frac{\partial}{\partial t}e_\theta = \frac{n(n+1)h_r}{r}-\left(\frac{1}{r}+\frac{\partial}{\partial r}\right)h_\varphi$	$\epsilon\frac{\partial}{\partial t}e_\theta = -\left(\frac{1}{r}+\frac{\partial}{\partial r}\right)h_\varphi$
$\epsilon\frac{\partial}{\partial t}e_\varphi = -\frac{n(n+1)h_r}{r}+\left(\frac{1}{r}+\frac{\partial}{\partial r}\right)h_\theta$	$\epsilon\frac{\partial}{\partial t}e_\varphi = \left(\frac{1}{r}+\frac{\partial}{\partial r}\right)h_\theta$

radial components must be developed.

Recall from equations (D.3), the radial component of u (and v) satisfy

$$\frac{1}{r^2}\frac{d}{dr}(r^2\frac{du_r}{dr})+\left[\frac{\omega^2}{c^2}-\frac{n(n+1)}{r^2}\right]u_r = 0 \tag{5.2}$$

which can be re-written as

$$\frac{1}{r^2}\frac{\partial}{\partial r}(r^2\frac{\partial u}{\partial r})+\left[\frac{-(j\omega)^2}{c^2}-\frac{n(n+1)}{r^2}\right]u = 0 \tag{5.3}$$

which then transforms into the time domain as

$$\frac{1}{r^2}\frac{\partial}{\partial r}(r^2\frac{\partial u}{\partial r})+\left[-\frac{1}{c^2}\frac{\partial^2}{\partial t^2}-\frac{n(n+1)}{r^2}\right]u = 0 \quad \text{or} \tag{5.4}$$

$$\frac{\partial^2 u}{\partial r^2}+\frac{2}{r}\frac{\partial u}{\partial r}-\frac{n(n+1)}{r^2}u-\frac{1}{c^2}\frac{\partial^2 u}{\partial t^2} = 0 \tag{5.5}$$

This provides an equation for u (and v) in r and t that can be discretized with a finite difference scheme.

The analogy to the waveguide case found in the PEE-FDTD method is now complete. Coupled field component equations that only depend on r and t have been derived (Table 5.3 and equation (5.5)) to which a finite difference scheme can be applied. The transverse functions for each component are determined from spherical harmonics as required.

5.2.4 Improved Implementation

Consider again Table 5.1, describing spherical waves for both TE and TM modes. All components are directly related to the functions u and v (where $\begin{matrix} u \\ v \end{matrix} = \begin{matrix} U(r,t) \\ V(r,t) \end{matrix} P_m^n(\cos\theta)e^{jm\varphi}$) through simple derivatives, so that the other components can be determined directly from the radial components via simple radial or time derivatives.

5.3 Finite Difference Approximations

5.3.1 Initial Implementation

Radial Component

First consider a discretization of (5.5). The form of the equation demands using a central difference for the second derivatives, and a forward difference for the first derivative. However, forward differences can introduce unwanted instabilities. Instead, let $u = \frac{w}{r}$, then

(5.5) is transformed to:

$$\frac{\partial^2 w}{\partial r^2} - \frac{n(n+1)}{r^2} w - \frac{1}{c^2}\frac{\partial^2 w}{\partial t^2} = 0 \tag{5.6}$$

which no longer contains a first derivative. Solutions to (5.6) are Schelkunoff functions which are related to spherical Bessel functions [76] as:

$$\widehat{Z}(r) = r z_n(r) = \sqrt{\frac{\pi r}{2}} Z_{n+1/2}(r) \tag{5.7}$$

where z refers to any of the spherical Bessel functions of first or second kind, or Hankel functions of the first or second kind. Thus the inherent numerical problems with forward and backward differences can be avoided by using (5.6), and recovering u (or v) as necessary by dividing the solution using $u = \frac{w}{r}$. The difference equation corresponding to (5.6) is

$$w_j^{i+1} = \left(\frac{c\Delta t}{\Delta r}\right)^2 \left[w_{j+1}^i - 2w_j^i + w_{j-1}^i\right] - \left(\frac{c\Delta t}{r_j}\right)^2 n(n+1) w_j^i + 2w_j^i - w_j^{i-1} \tag{5.8}$$

where the superscript i denotes the timestep index, and j is the radial index.

Angular Components

Examining Table 5.2, note that all components are of the same general form given in equation (5.9), except for a factor of ± 1. In this description f, g are the electric (e) or magnetic field (h) component as required, a_1 and a_2 are either θ or φ as required, and $\rho \in \{\varepsilon, \mu\}$ accordingly.

$$\rho \frac{\partial}{\partial t} f_{a_1} = n(n+1)\frac{g_r}{r} - \left(\frac{1}{r} + \frac{\partial}{\partial r}\right) g_{a_2} \tag{5.9}$$

To maintain consistency with the Yee formulation, and also because it provides implicitly better stability, a staggered one-dimensional grid for electric and magnetic field components

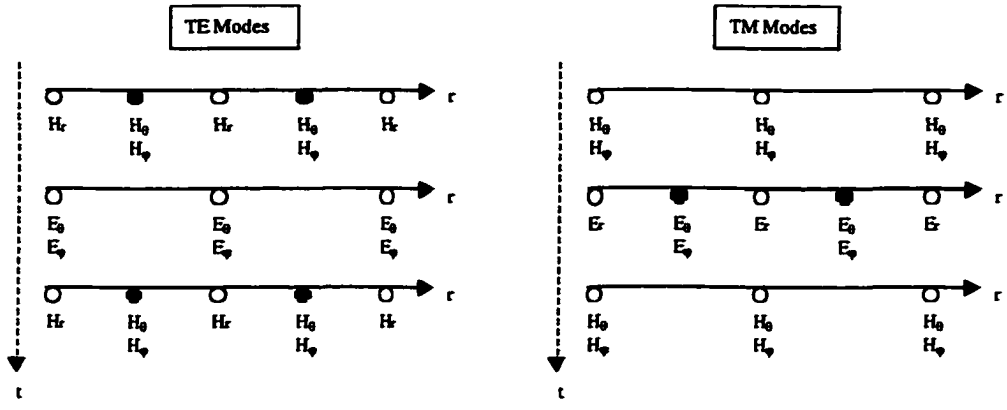

Figure 5.1: Relative placement of field components for both TE and TM modes. Note that components are staggered by half a grid cell in time and space.

is assumed. Thus, e and h are staggered by one-half of a timestep and one-half of a radial step. Discretization of (5.9) then leads to equation (5.10).

$$f_{a_1,j}^{n+1/2} = f_{a_1,j}^{n-1/2} + \frac{\Delta t}{\rho} n(n+1) \left(\frac{g_{r,j+1/2}^{n} + g_{r,j-1/2}^{n}}{2r_j} \right) - \frac{\Delta t}{\rho} \left\{ \left(\frac{g_{a_2,j+1/2}^{n} + g_{a_2,j-1/2}^{n}}{2r_j} \right) + \left(\frac{g_{a_2,j+1/2}^{n} - g_{a_2,j-1/2}^{n}}{\Delta r} \right) \right\} \quad (5.10)$$

5.3.2 Improved Implementation

Consider a discretized scheme in radius and time where in the TE modes the field components $(H_r, E_\theta, E_\varphi)$ lie at locations $k\Delta r$, and (H_θ, H_φ) lie at $(k+1/2)\,\Delta r$. For TM modes the field components $(E_r, H_\theta, H_\varphi)$ lie at locations $k\,\Delta r$, and (E_θ, E_φ) lie at $(k+1/2)\,\Delta r$. Magnetic field components are at timesteps $n\Delta t$ and electric field components at timesteps $(n+1/2)\,\Delta t$. This is shown pictorially in Figure 5.1. For this implementation, the radial components are determined exactly as before.

Radial Derivatives

The radial derivatives of concern, e.g. $h_\theta(r,t) = \frac{1}{r}\frac{\partial}{\partial r}\left[r^2 h_r(r,t)\right]$, are of a similar form. It needs to be emphasized that angular components are staggered from the radial components by half a grid cell, and therefore they lend themselves immediately to a central difference representation:

$$f_a(r,t) = \frac{1}{r}\frac{\partial}{\partial r}\left[r^2 f_r\right] = 2f_r + r\frac{\partial f_r}{\partial r} \Rightarrow$$
$$f^i_{a,k+1/2} = (f^i_{r,k+1} + f^i_{r,k}) + r_{k+1/2}\frac{(f^i_{r,k+1} - f^i_{r,k})}{\Delta r} \tag{5.11}$$

where k is the radial index, a represents a given angular component, and f represents magnetic or electric fields.

Time Derivatives

Time derivatives, e.g. $e_\theta(r,t) = -\mu\frac{\partial}{\partial t} r h_r(r,t)$, are of a similar form also. Electric and magnetic fields are staggered in time by half a time step, and the necessary components are co-located in radius. So once again, it is a simple measure to represent the time derivative with a central difference scheme:

$$g_a(r,t) = \rho\frac{\partial}{\partial t} r f_r \Rightarrow g^{i+1/2}_{a,k} = \rho r_k \frac{(f^{i+1}_{r,k} - f^i_{r,k})}{\Delta t} \tag{5.12}$$

where $\rho \in \{\epsilon, \mu\}$ and f, g are electric or magnetic fields. This scheme requires the future value of the radial component $f^{i+1}_{r,k}$. However, since the radial component depends only on previous radial components (and not on polar or azimuthal components), the i-th time step non-radial components can be evaluated after $f^{i+1}_{r,k}$ are already known, without loss of precision or any numerical overhead. Moreover, those components can be computed only in those locations where they are actually needed.

Advantages

The main advantage of the improved method is that only one component needs to be fully propagated: the radial component. This reduces some of the storage necessary for maintaining the angular components (there is no longer a need to store previous values). Finally, absorbing boundary conditions need only be implemented on the radial components. Furthermore, the method for determining the angular modes is simpler than with the previous scheme. The difference equations are simpler and require fewer operations. This should reduce runtime slightly as well.

5.4 Summary of Method

The goal of this method is to implement spherical waves as sources on the Huygens' surface in an existing total/scattered FDTD formulation. Implementation is analogous to the plane wave excitation, by way of one-dimensional source grids except in the radial direction. An alternate set of radial amplitude functions is time-stepped for each mode order n. The assumptions made are 1) that the angular positions (θ, φ) of all points on the Huygens' surface are known, for which the angular functions can be pre-computed; 2) the time excitation is used as the source function for the source grids; and 3) that the spherical wave expansion coefficients are known which are then used as weighting functions for each specific mode.

A graphic representation of the method is shown in Figure 5.2. The actions pertaining to each step are:

1. Pre-compute angular functions for points on Huygens' surface;

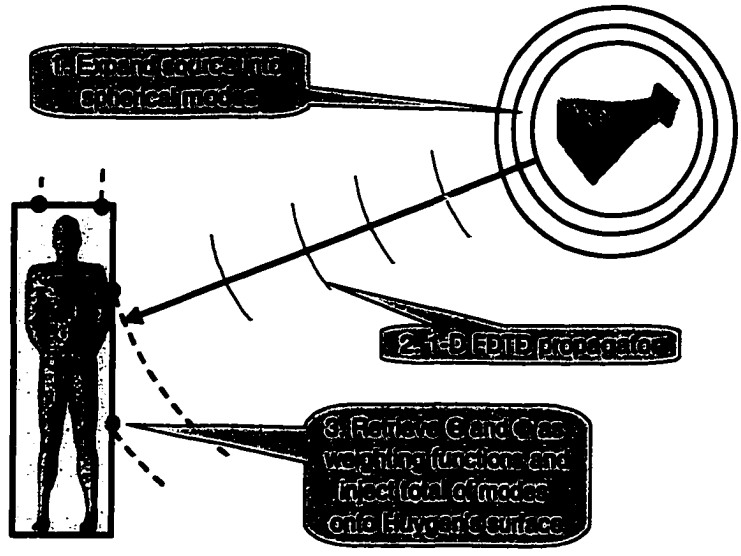

Figure 5.2: Graphic demonstrating a summary of the spherical wave FDTD method.

2. Time-step difference equations for modal amplitude functions;

3. For a particular point, at radius r, on Huygens' surface:

   - take amplitude function values from 1-d grids

   - multiply as appropriate by angular functions

   - sum all modes to recover the total incident field

The following chapters will detail some of the numerical issues related to implementation, including stability and dispersion, as well as providing numerical validation of the method. Although the initial implementation was pursued for a large part of this research, the results presented are based solely on the improved implementation. The initial implementation was successfully implemented for TM modes but difficulty was encountered while implementing the TE modes. The improved implementation offered several advantages and no apparent disadvantages, and so the initial line of research was abandoned.

Chapter 6

Numerical Issues

6.1 Numerical Calculation of Angular Functions

At some point in the implementation, the transverse functions in the form of spherical harmonics $Y_{nm}(\theta,\varphi) = P_n^m(\cos\theta)\begin{matrix}\cos\\ \sin\end{matrix} m\varphi$ and their derivatives must be incorporated to determine the total value of field components at the Huygens' surface. The azimuthal factor $\begin{matrix}\cos\\ \sin\end{matrix} m\varphi$ is simple to incorporate numerically and will not be considered further. However, numeric determination of the associated Legendre functions $P_n^m(\cos\theta)$ and their derivatives can be troublesome if not handled properly. This section details development of a stable recurrence scheme for the transverse functions.

Various recurrence relations exist for the determination of associated Legendre functions that can be used in the numerical implementation of the vector wave functions. The necessary equations are listed below (from [3] and [77]):

$$P_n^{m+1}(\cos\theta) = \frac{2m\cos\theta}{\sin\theta} P_n^m(\cos\theta) - (n-m-1)(n+m)P_n^{m-1}(\cos\theta) \qquad (6.1)$$

$$P_{n+1}^m(\cos\theta) = \frac{2n+1}{n+1-m} P_n^m(\cos\theta) - \frac{(n+m)}{n+1-m} P_{n-1}^m(\cos\theta) \tag{6.2}$$

$$\frac{\partial}{\partial\theta} P_n^m(\cos\theta) = \frac{(n-m+1)\, P_{n+1}^m(\cos\theta) - (n+1)\cos\theta P_n^m(\cos\theta)}{\sin\theta} \tag{6.3}$$

From [78], equation (6.2) is always stable, but (6.1) and (6.3) are questionable. One must be especially cautious about values near $\theta = 0, \pi$. However, Boerner et al. [79] show that alternate polar functions can be constructed, for which relations exist that do not include singularities. Defining [79]

$$^1G_n^m(\cos\theta) = \frac{m}{\sin\theta} P_n^m(\cos\theta) \text{ and} \tag{6.4}$$

$$^2G_n^m(\cos\theta) = \frac{\partial}{\partial\theta} P_n^m(\cos\theta) \tag{6.5}$$

it can be shown that:

$$\begin{aligned} ^1G_n^m(\cos\theta) = \frac{1}{2}\cos\theta\{&P_n^{m+1}(\cos\theta) \\ &+ (n-m+1)(n+m) P_n^{m-1}(\cos\theta)\} \\ &+ m\sin\theta P_n^m(\cos\theta) \end{aligned} \tag{6.6}$$

and:

$$^2G_n^m(\cos\theta) = \frac{1}{2}\{(n-m+1)(n+m) P_n^{m-1}(\cos\theta) - P_n^{m+1}(\cos\theta)\} \tag{6.7}$$

so that the apparent singularity is removed. A lesser problem is then encountered, namely how to use (6.6) and (6.7) for the case of $m = 0$ and $m = n$ (since then terms of $m = -1$ and $m = n+1$ are involved). There is no problem for $m = n$ because $P_n^{n+1} = 0$ from the fundamental definition. For (6.6), $m = 0$ and hence $^1G_n^0 = 0$ automatically from (6.4).

For (6.7) however, there appears to be a problem because of the lack of a definition for $P_n^{-1}(\cos\theta)$. From (6.6) it is known that:

$$
\begin{aligned}
{}^1G_n^0(\cos\theta) &= 0 = \frac{1}{2}\cos\theta\left[(n+1)(n)P_n^{-1}(\cos\theta) + P_n^1(\cos\theta)\right] \\
\therefore \quad P_n^{-1}(\cos\theta) &= \frac{-P_n^1(\cos\theta)}{n(n+1)}
\end{aligned}
\tag{6.8}
$$

which when substituted into (6.7) with $m = 0$ gives:

$$
\begin{aligned}
{}^2G_n^0(\cos\theta) &= \frac{1}{2}\left[(n+1)(n)P_n^{-1}(\cos\theta) - P_n^1(\cos\theta)\right] \\
&= \frac{1}{2}\left[n(n+1)\frac{-P_n^1(\cos\theta)}{n(n+1)} - P_n^1(\cos\theta)\right] \\
&= -P_n^1(\cos\theta)
\end{aligned}
\tag{6.9}
$$

Therefore, spherical wave vectors can be expressed in terms of the modified wave functions (6.10, 6.11):

$$
\begin{aligned}
\vec{m}^{(i)}_{\substack{e\\o}mn} &= \left(\mp z_n^{(i)}(kr)\,{}^1G_n^m(\cos\theta)\begin{matrix}\sin\\\cos\end{matrix} m\varphi\right)\widehat{\theta} \\
&\quad - \left(z_n^{(i)}(kr)\,{}^2G_n^m(\cos\theta)\begin{matrix}\cos\\\sin\end{matrix} m\varphi\right)\widehat{\varphi}
\end{aligned}
\tag{6.10}
$$

$$
\begin{aligned}
\vec{n}^{(i)}_{\substack{e\\o}mn} &= \left(\frac{n(n+1)}{kr}z_n^{(i)}(kr)P_n^m(\cos\theta)\begin{matrix}\cos\\\sin\end{matrix} m\varphi\right)\widehat{r} \\
&\quad + \left(\frac{1}{kr}\frac{\partial}{\partial r}\left[rz_n^{(i)}(kr)\right]\,{}^2G_n^m(\cos\theta)\begin{matrix}\cos\\\sin\end{matrix} m\varphi\right)\widehat{\theta} \\
&\quad + \left(\mp\frac{1}{kr}\frac{\partial}{\partial r}\left[rz_n^{(i)}(kr)\right]\,{}^1G_n^m(\cos\theta)\begin{matrix}\sin\\\cos\end{matrix} m\varphi\right)\widehat{\varphi}
\end{aligned}
\tag{6.11}
$$

Another point of numerical consideration is that essentially single field values are the target for every point on the Huygens' surface. These are obtained through summation over all calculated modes. One concern is that the higher order values of the Legendre functions attain very large values, i.e. of order 10^{20} or greater for $n \simeq 25$. Thus, in numerical implementation of this approach, consideration must be given to a) the initial

determination of such numbers to a useful degree of accuracy; and b) the summation of these numbers which could have changing signs. The result could be large overflow or round off errors which may cause inaccuracies in the determination of the resultant field. However, in general large values in higher order wave functions are mitigated by very small values in the corresponding mode coefficients. This may aid in the numerical implementation. As well, double precision arithmetic in the FORTRAN 90 coding of the above should aid in limiting overflow/underflow errors.

6.2 Stability

As a prelude to the full implementation of spherical waves in the FDTD method, it is useful to investigate the stability conditions of the underlying one dimensional source grid. The analytic solution of the spherical field components leads to spherical Hankel functions, in contrast to pure complex exponentials for the plane wave case. As a result, there are algebraic difficulties encountered with the traditional stability analysis. In this section, the stability criterion for the FDTD equations for radial field modes is derived by taking advantage of the similarities of the wave operators in spherical and Cartesian coordinate systems.

6.2.1 Cartesian Wave Equation

Consider first the wave equation (6.12) in Cartesian coordinates:

$$\frac{\partial^2 f}{\partial t^2} + \mathbf{L}f = 0 \tag{6.12}$$

When no y-dependency is assumed, the operator $\mathbf{L} = -c^2\left(\frac{\partial^2}{\partial x^2} + \frac{\partial^2}{\partial z^2}\right)$ is the Laplacian operator in two dimensions, with c being the speed of light in vacuum. Although the stability analysis has been demonstrated in many publications [2, 80], it is useful to outline the process here, since in the next section the analogy with the Cartesian case is utilized. If the typical field variation of $\exp(-j\beta_z z)$ in the z-direction is assumed, the operator takes the form $\mathbf{L} = -c^2\left(\frac{\partial^2}{\partial x^2} - \beta_z^2\right)$.

Casting the operator in discrete form with familiar central differences, and investigating the eigenvalue problem for the discrete operator gives:

$$\lambda = -c^2\left(\frac{\frac{f_{i+1}}{f_i} - 2 + \frac{f_{i-1}}{f_i}}{(\Delta x)^2} - \beta_z^2\right)$$

where i is the index for nodes in the x-direction, and Δx is the distance between nodes (i.e. mesh size). Performing a Fourier analysis for the discretized space by letting $f_i = \exp(-j\widetilde{\beta}_x i\Delta x)$ (here $\widetilde{\beta}_x$ is the numerical phase constant analogous to the analytic phase constant β_x) produces:

$$\lambda = -c^2\left(\frac{2\cos\left(\widetilde{\beta}_x\Delta x\right) - 2}{(\Delta x)^2} - \beta_z^2\right)$$

From [80], for a self-adjoint operator $\mathbf{L}$ defined in the Hilbert space $\mathcal{H}$, the norm of the operator is defined as:

$$\|\mathbf{L}\| = \sup_{y\in\mathcal{H},\|y\|=1} |\langle \mathbf{L}y, y\rangle| = |\lambda_{\max}|$$

Examining the limits of the cosine operator gives $|\lambda_{\max}|$ and, hence, the norm of the operator as

$$\|\mathbf{L}\| = |\lambda_{\max}| = c^2\left(\frac{4}{(\Delta x)^2} + \beta_z^2\right) \tag{6.13}$$

Following the functional analysis approach of [80], (6.13) provides the time-step stability condition for (6.12) expressed as:

$$\Delta t \leq \frac{2}{\sqrt{\|\mathbf{L}\|}} \tag{6.14a}$$

$$= \frac{2}{c\sqrt{\frac{4}{(\Delta x)^2}+\beta_z^2}} \tag{6.14b}$$

$$= \frac{1}{c\sqrt{\frac{1}{(\Delta x)^2}+\left(\frac{\beta_z}{2}\right)^2}} \tag{6.14c}$$

6.2.2 Radial Wave Equation

For the purposes of the spherical waves in FDTD, we focus on the Schelkunoff form of the radial wave equation (5.6) . Consider again (6.12), and compare it with the Schelkunoff operator $\mathbf{L} = -c^2\left(\frac{\partial^2}{\partial r^2} - \frac{n(n+1)}{r^2}\right)$ governing the modal solutions in spherical coordinates, where r is the radius and n is a positive integer indicating the mode number. The Schelkunoff operator has a very similar form to the Cartesian case, except that the zeroth order term is now dependent on the variable r. Normally a rigorous stability analysis is required, but in this case a more relaxed approach is considered. This approach provides a stability criterion that is more stringent than necessary (it is an over-approximation). The radial operator is of the form $\mathbf{L} = -c^2\left(\frac{\partial^2}{\partial r^2} - b(r)\right)$ with b as a function of r. When $\mathbf{L} = -c^2\left(\frac{\partial^2}{\partial r^2} - b\right)$, the norm $\|\mathbf{L}\|$ takes the value from (6.13). Notice, however, that:

$$\|\mathbf{L}\| \leq \left\|c^2\left(\frac{\partial^2}{\partial r^2} + b(r)\right)\right\| \leq \left\|c^2\left(\frac{\partial^2}{\partial r^2} + b_{\max}\right)\right\| \tag{6.15}$$

where $b_{\max} = \sup b(r)$.

To find a value for $b_{\max}$, the system that is discretized for some minimum radius $r = r_0$ is considered. In this case $b_{\max} = \frac{n(n+1)}{r_0^2}$. The corresponding value for the necessary

time-step is then:

$$\Delta t \leq \frac{1}{c\sqrt{\frac{1}{(\Delta r)^2} + \frac{n(n+1)}{4r_0^2}}} \tag{6.16}$$

This result has been tested rigorously with the difference equation for the radial mode (5.8) in isolation, and no early or late time instabilities were manifested when the time-step was kept within the bounds of (6.16). Furthermore, the tests showed that the method did go unstable on the other side of the upper bound (at 5% greater in the test case).

The implication of (6.16) is that the maximum time-step allowable in the spherical wave FDTD method depends on the maximum mode number used, and the minimum radius of the expansion. To aid in assessing the numerical effort required, a typical spherical wave expansion can be studied. For such a case, the number of modes N necessary to accurately describe the source depends on the wave number k and the radius of the minimum sphere enclosing the source r_0, typically as $N \simeq kr_0$ from [63]. So if the highest frequency of interest (hence the corresponding maximum for k) and the minimum sphere radius r_0 are known, then a useful guideline for the required time-step is:

$$\Delta t \leq \frac{1}{c\sqrt{\frac{1}{(\Delta r)^2} + \frac{kr_0(kr_0+1)}{4r_0^2}}} \tag{6.17}$$

6.3 Dispersion Analysis of the Schelkunoff Equation

$$\frac{\partial^2 f}{\partial r^2} - \frac{n(n+1)}{r^2} f = \frac{1}{c^2}\frac{\partial^2 f}{\partial t^2} \tag{6.18}$$

The focus of this section is on the analysis of the numerical dispersion in the discretization of the Schelkunoff equation (6.18) in radius and time, which describes the propagation of the radial component of TE and TM modes in spherical waves. This equation is discretized as (6.19), where i represents the time index, and m represents the radial index. The dispersion analysis follows the method outlined in [2].

$$\frac{f_m^{i+1} - 2f_m^i + f_m^{i-1}}{(\Delta t)^2} = c^2 \left[\frac{f_{m+1}^i - 2f_m^i + f_{m-1}^i}{(\Delta r)^2} \right] - c^2 \frac{n(n+1)}{r^2} f_m^i \tag{6.19}$$

Assume Fourier modes of frequency ω and numerical wave number $\tilde{k}$ by letting $f_m^i = e^{j(\tilde{k}m\Delta r - \omega i \Delta t)}$. Then (6.19) becomes

$$e^{j(\tilde{k}m\Delta r - \omega i\Delta t)} \left(\frac{e^{-j\omega\Delta t} - 2 + e^{j\omega\Delta t}}{(\Delta t)^2} \right) = c^2 e^{j(\tilde{k}m\Delta r - \omega i\Delta t)} \left[\frac{e^{\tilde{k}\Delta r} - 2 + e^{-\tilde{k}\Delta r}}{(\Delta r)^2} - \frac{n(n+1)}{r^2} \right]$$

which with trigonometric substitutions leads to the final dispersion relation

$$\left[\frac{1}{c\Delta t} \sin(\frac{\omega \Delta t}{2}) \right]^2 = \left[\frac{1}{\Delta r} \sin(\frac{\tilde{k}\Delta r}{2}) \right]^2 + \frac{n(n+1)}{4r^2} \tag{6.20}$$

This compares well with the expressions for dispersion in the Cartesian case in [2], except for the second factor on the right hand side of the equation. This term indicates that dispersion is dependent on the mode number n, as expected. It also shows that the dispersion is dependent on the radius. This is related to the cutoff phenomena of spherical waves, as discussed in Appendix D; higher order modes are essentially evanescent up to a particular radius which increases with mode number n.

The dispersion relation (6.20) can be solved directly to give the numerical wave number $\tilde{k}$, if we assume a single frequency and a radius $r = m\Delta r$, as

$$\tilde{k}_{nm} = \pm \frac{2}{\Delta r} \sin^{-1} \left[\frac{\sqrt{(2m\Delta r)^2 \sin^2(\frac{\omega\Delta t}{2}) - n(n+1)(c\Delta t)^2}}{2mc\Delta t} \right] \tag{6.21}$$

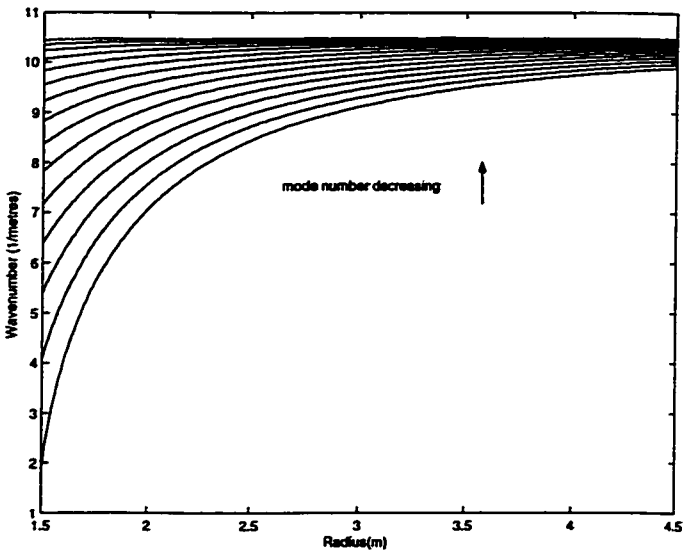

Figure 6.1: Plots of the numerical wavenumber versus radius for $n = 1$ to $n = 15$

Figure 6.1 shows an example of how the wavenumber changes with increasing order of n. In this example, $dt = 1.4 \times 10^{-11}$ sec, $\omega = 10\pi \times 10^{8}\,\mathrm{sec}^{-1}$ and $dr = 0.01m$. It can be stated that as the mode order increases, the dispersion increases. This is because the imaginary part of the Hankel function starts to dominate as $kr \rightarrow 0$ with a turning point at $kr = n$. In essence, this means the wavelength becomes extremely long. Alternatively it can be said that the region of large dispersion lies in the reactive near-field of the source.

6.3.1 Some Results of Dispersion

Figures 6.2-6.4 show some computed radial component values versus analytic ones, where the computed source function (at $r = r_{\mathrm{min}}$) has been initiated by implementing the analytic function, but windowed with a Hamming window for the first 50 time-steps. No window was used in the analytic function.

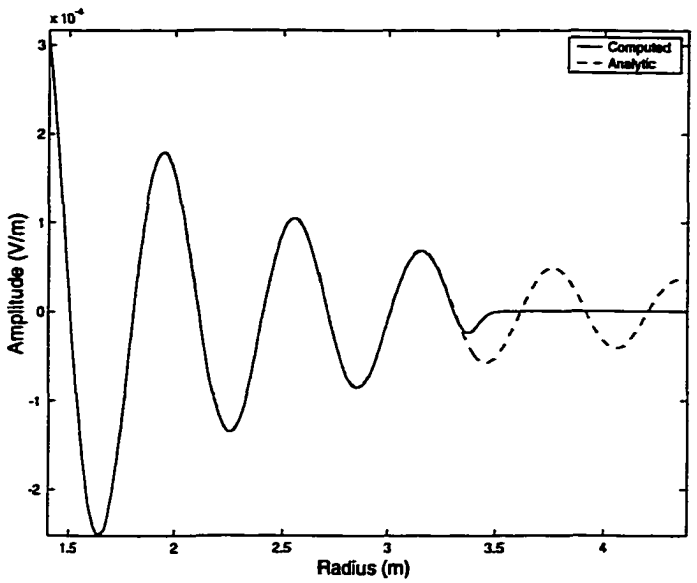

Figure 6.2: Solutions of the $n = 1$ radial electric field component E_r - computed (—) vs. analytic (- - -)

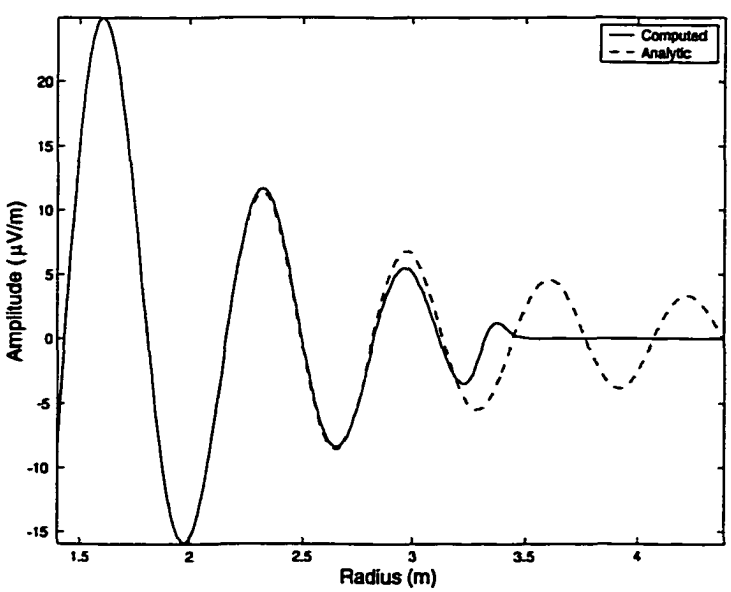

Figure 6.3: Solutions of the $n = 10$ radial electric field component E_r - computed (—) vs. analytic (- - -)

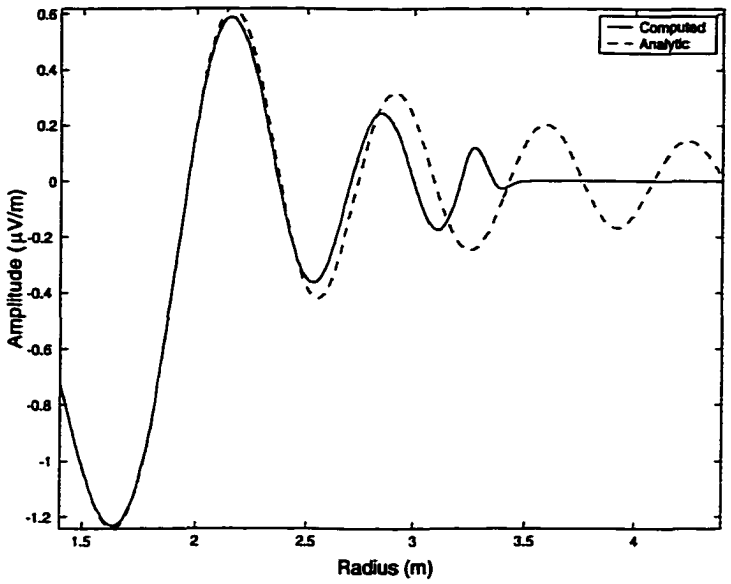

Figure 6.4: Solutions of the $n = 15$ radial electric field component E_r - computed (—) vs. analytic (- - -)

Note that as the mode index n increases, the wave packet of the computed solution seems to compress as the radius increases. This may be because the windowing function introduces a frequency shift on the signal, which then has a different wave number. Alternatively we must consider the initial conditions used in the numerical scheme. For a second order system, the difference equations rely on the two previous time-steps - in essence, an initial condition is needed for the function and its first derivative. However, the initial conditions were implemented on the "previous time-steps" by simply setting them to zero (for $t = 0$). This does not accurately reflect the initial conditions (the derivative is wrong), which introduces numerical errors at the start of the wavefront. In either case, it is clear that the numerical solution to (6.18) is dispersive, with higher dispersion accompanying increasing orders of n.

6.4 Boundary Conditions

This section discusses preliminary implementation of absorbing boundary conditions (ABC) for the spherical wave FDTD method. Appendix A detailed the general development of ABCs, classifying them in two distinct types: annihilators and material absorbers. For implementation in this method, the concentration has been solely on annihilator types. The type used is derived from the Mur ABC, modified for the spherical geometry. Following description of the modified Mur equations is a short discussion on filter type ABCs. These show promise for further improvement for modal absorption.

6.4.1 Mur by Way of the Enquist-Majda One-Way Wave Equations

A way of constructing the radial derivative operator used for annihilator type ABCs was introduced by Enquist and Majda through *one-way wave equations* (summarized in [2]). The wave equation is factored into two, one-way partial derivative operators. This is introduced by relating this to the radial Schelkunoff equation (6.18), repeated here for convenience,

$$\frac{\partial^2 f}{\partial r^2} - \frac{n(n+1)}{r^2} f - \frac{1}{c^2}\frac{\partial^2 f}{\partial t^2} = 0$$

which can be written compactly as $Lf = 0$.

Now consider that factoring L such that $Lf = L^+L^-f = 0$. In this case, the factored operators are $L^+ = D_r + \frac{D_t}{c}\sqrt{1+S^2}$ and $L^- = D_r - \frac{D_t}{c}\sqrt{1+S^2}$, with $D_r = \frac{\partial}{\partial r}$ and $D_t = \frac{\partial}{\partial t}$, and $S = \frac{c\sqrt{n(n+1)}}{D_t r}$ represents a pseudo-differential operator. The factored operators allow for waves to propagate only in the outward or inward directions, respectively. So by using L^+ at the outer boundary the domain can be terminated, since it only allows

for wave travel in one direction. This is accomplished by approximating $\sqrt{1+S^2}$.

1st Approximation In the first approximation, let $\sqrt{1+S^2} \simeq 1$, and so $L^+ \simeq D_r + \frac{D_t}{c}$. For this case then, the equation for the outer boundary becomes

$$\frac{\partial f}{\partial r} + \frac{1}{c}\frac{\partial f}{\partial t} = 0 \tag{6.22}$$

2nd Approximation In the second approximation, let $\sqrt{1+S^2} \simeq 1 + \frac{1}{2}S^2$, and so $L^+ \simeq D_r + \frac{D_t}{c}\left(1 + \frac{n(n+1)}{2r^2}\left(\frac{c}{D_t}\right)^2\right)$ or equivalently

$$\frac{\partial^2 f}{\partial r \partial t} + \frac{1}{c}\frac{\partial^2 f}{\partial t^2} + \frac{n(n+1)}{2r^2} f = 0. \tag{6.23}$$

Either of these approximations is then applied to the field component lying at the outer boundary of the domain. Let the field at the outer grid point be $f = f_k^i$, where k is at r_m (at the outer grid point) and i is the time index. Following Mur, the derivatives are expanded as difference equations about an auxiliary grid point half a cell inside the domain at $r_d = r_m - \frac{\Delta r}{2}$. Equation (6.23) is then:

$$\begin{aligned}
\left.\frac{\partial^2 f}{\partial r \partial t}\right|_{r_d}^{i} &= \frac{1}{2\Delta t}\left(\left.\frac{\partial f}{\partial r}\right|_{r_d}^{i+1} - \left.\frac{\partial f}{\partial r}\right|_{r_{di}}^{i-1}\right) \\
&= \frac{1}{2\Delta t}\left[\left(\frac{f_k^{i+1} - f_{k-1}^{i+1}}{\Delta r}\right) - \left(\frac{f_k^{i-1} - f_{k-1}^{i-1}}{\Delta r}\right)\right]
\end{aligned}$$

$$\begin{aligned}
\left.\frac{\partial^2 f}{\partial t^2}\right|_{r_d}^{i} &= \frac{1}{2}\left(\left.\frac{\partial^2 f}{\partial t^2}\right|_{r_m}^{i} + \left.\frac{\partial^2 f}{\partial t^2}\right|_{r_m - \Delta r}^{i}\right) \\
&= \frac{1}{2}\left[\left(\frac{f_k^{i+1} - 2f_k^i + f_k^{i-1}}{(\Delta t)^2}\right) + \left(\frac{f_{k-1}^{i+1} - 2f_{k-1}^i + f_{k-1}^{i-1}}{(\Delta t)^2}\right)\right]
\end{aligned}$$

$$\frac{cn(n+1)}{2r^2} f = \frac{cn(n+1)}{4r_d^2}\left(f_k^i + f_{k-1}^i\right)$$

and thus,

$$\frac{1}{2\Delta t}\left[\left(\frac{f_k^{d+1}-f_{k-1}^{d+1}}{\Delta r}\right)-\left(\frac{f_k^{d-1}-f_{k-1}^{d-1}}{\Delta r}\right)\right] + \frac{1}{2c}\left[\left(\frac{f_k^{d+1}-2f_k^d+f_k^{d-1}}{(\Delta t)^2}\right)+\left(\frac{f_{k-1}^{d+1}-2f_{k-1}^d+f_{k-1}^{d-1}}{(\Delta t)^2}\right)\right] + \frac{cn(n+1)}{4r_i^2}\left(f_k^d+f_{k-1}^d\right)=0$$

which reduces to the update equation for the outer field component,

$$f_k^{i+1} = -f_{k-1}^{i-1}+\frac{c\Delta t-\Delta r}{c\Delta t+\Delta r}\left(f_{k-1}^{i+1}+f_k^{i-1}\right) - \frac{2c(\Delta t)^2\,\Delta r\left(\frac{cn(n+1)}{4r_d^2}-\frac{1}{c(\Delta t)^2}\right)}{c\Delta t+\Delta r}\left(f_k^i+f_{k-1}^i\right) \tag{6.24}$$

In an analogous manner, the difference equation can be created for the Mur 1st order condition (6.22) as,

$$f_k^{i+1}=-f_{k-1}^i+\frac{c\Delta t-\Delta r}{c\Delta t+\Delta r}\left(f_{k-1}^{i+1}-f_k^i\right) \tag{6.25}$$

6.4.2 Filter Type

ABCs can be constructed in the manner of filters by employing time domain diakoptics. Here, the impulse response of a section of a guide is used and a convolution integral determines the field at the ABC. The digital filter is used to implement the convolution operator in an efficient and fast manner. The filter coefficients are found by a simple "tuning process" which consists of curve-fitting in a least-squares sense after a very short simulation in the computational domain.

Mrozowski and Kreczkowski [81, 82] have demonstrated several implementations of these filters, using either zero-pole filters or orthonormal filters. Even for low order

filters of either type, the performance is at least on par with Mur boundary conditions. PMLs, which are considered to be the de facto standard in all FDTD simulations, can be outperformed with higher order filters.

Given their relative ease of implementation, and the reported performance, a filter ABC may prove superior to the Mur boundary conditions for modal absorption.

Chapter 7

Method Validation

Chapter 5 described the method by which spherical waves can be propagated in a FDTD method, and the previous chapter outlined some of the numerical issues anticipated in implementation of the method. This chapter describes validation of the method, by examining results obtained at increasingly complex stages of the programming. All programming was completed in FORTRAN 90, and results have been examined in MATLAB, unless otherwise noted.

The validation is divided into two sections focussed around incorporation of the spherical waves as sources in an existing Cartesian FDTD program. In the first section, validation of the development of the spherical wave FDTD (SW-FDTD) program component alone is provided, being uncoupled to the Cartesian FDTD program component. In the second section, the SW-FDTD program component is incorporated as a source for the total/scattered field formulation, and results are provided to demonstrate the efficacy of the program incorporation.

7.1 SW-FDTD Program Component Validation

Validation of the SW-FDTD program component development is progressively demonstrated in three stages. In the first stage, the key difference equations used for the method are verified against expected modes in a spherical resonant cavity. In the second stage, these equations are further verified for the free space modes of a simple, infinitesimal dipole. The first and second stages demonstrate initial verification of the method. The final stage demonstrates validation for a more complex source involving multiple modes, for which an analytic solution exists.

In each case of verification, it should be noted that the analytic solution provided for reference is not the true, fully causal signal. Rather, for ease of representation, the time-harmonic, continuous wave solution is provided. The correct phase is maintained by taking into account both the spatial and temporal component of the complex exponential representing the signal according to spherical wave theory. For instance, the analytic solution is represented with radial and time dependence as the product of a spherical Hankel function in radius, and a complex exponential in time and frequency, say $f_n(r,t;k,\omega) = h_n(kr)e^{j\omega t}$. For the simulation, the real part of the analytic solution, $\mathrm{Re}(f_n)$, is used as the source for the one dimensional modal grids. In sections to follow, the simulated and numerically propagated solutions are then compared with the real part of analytic solutions, $\mathrm{Re}(f_n)$. As a result, the analytic solutions provided will seem to indicate a signal that initiated well before time $t = 0$, whereas the computed solutions, that are overlaid graphically, demonstrate proper causality.

7.1.1 Initial Verification

The one-dimensional coupled modal amplitude difference equations (5.8), (5.11), and (5.12), and the analytic angular functions, have been implemented in a program module written in FORTRAN 90. The program allows for the following inputs: specification of the maximum mode order n, the minimum radius r_0, the timestep increment dt, the radial increment dr, the number of radial steps nr, the number of timesteps nt, the angular increments $d\theta$ and $d\varphi$, and the number of angular nodes $n\theta$ and $n\varphi$. The outputs are the modal amplitudes for each mode, each component, each timestep and radius, and the total field component (including the angular function) for each mode at each timestep and each radius. Absorbing boundary conditions have been implemented as 1st order Mur conditions. Also, for this initial program, the specification of the time excitation is made explicitly in the program on a case by case basis as required.

Initial verification of the program has been performed using two simple cases. First, equation (5.8) was verified by simulating a spherical resonator for both TE and TM modes. Secondly, the fields radiating from an infinitesimal dipole into free space were investigated by comparing with the analytic solutions.

7.1.2 Spherical Resonator Modes

Analytic Solutions

A spherical cavity resonator is formed as a spherical perfectly conducting shell of radius $r = a$ filled with free space. The wave function for this arrangement admits the Schelkunoff function $\widehat{J}_n(kr)$ (5.7) in the radial direction, where k is the wave number. The

Table 7.1: Ordered zeros and resonant frequencies for $n = 1$, for a spherical cavity of radius $r = 1\,\mathrm{m}$.

p	u_{1p}	$(f_r)^{TE}_{m1p}$ (MHz)	u'_{1p}	$(f_r)^{TM}_{m1p}$ (MHz)
1	4.493	214.52	2.744	131.01
2	7.725	368.84	6.117	292.06
3	10.904	520.63	9.317	444.85
4	14.066	671.60	12.486	596.16
5	17.221	822.24	15.644	746.94
6	20.371	972.64	18.796	897.44

conducting walls impose boundary conditions such that for TE modes $\widehat{J}_n(ka) = 0$ and for TM modes $\widehat{J}'_n(ka) = 0$ (the prime indicating the first derivative with respect to r). The boundary conditions are satisfied by choosing $k = \frac{u_{np}}{a}$ for TE modes and $k = \frac{u'_{np}}{a}$ for TM, where u_{np} and u'_{np} are the denumerably infinite set of zeros of the Schelkunoff function and its derivative, respectively. Relating the wave number to frequency, the resonant frequencies are then found [76] as:

$$(f_r)^{TE}_{mnp} = \frac{u_{np}}{2\pi a\sqrt{\varepsilon\mu}} \tag{7.1}$$

$$(f_r)^{TM}_{mnp} = \frac{u'_{np}}{2\pi a\sqrt{\varepsilon\mu}} \tag{7.2}$$

The zeros and resonant frequencies for a sphere of radius $r = 1\,\mathrm{m}$ are tabulated in Table (7.1) for $n = 1$ [76]. The resonant frequency is not dependent on the mode index m, indicating degeneracies.

Computed Results

The difference equation for the Schelkunoff function (5.8) was tested for a spherical cavity resonator of radius $r = 1\,\mathrm{m}$ for both TE and TM modes of the lowest index $n = 1$. In both cases the spatial discretization was $dr = 0.01\,\mathrm{m}$, the time-step was $dt = 14\,\mathrm{ps}$, and

the simulation was allowed to proceed for 10,000 time-steps. The cavities were excited at $r = 0.1\,\mathrm{m}$ with a unit amplitude function at the initial timestep, with zero excitation at all other timesteps.

The only difference between the two simulations was in the specification of the boundary conditions. In the TE case, boundaries are handled by specifying the value at each end of the domain (i.e. $r = 0\,\mathrm{m}$ and $r = 1\,\mathrm{m}$) to be zero for all time steps. For the TM case, the domain is extended beyond each physical boundary by one grid increment each, with appropriate image values specified at each time-step to simulate the boundary condition of continuity.

To examine the results, the Fourier transform of the time signal at $r = 0.5\,\mathrm{m}$ was taken at a frequency resolution of 1 MHz, and the resultant frequency components were compared with the analytic frequencies expected, as outlined in Table (7.1). The results are shown in Figures (7.1) and (7.2). Excellent agreement is found between computed and analytic frequencies, demonstrating that equation (5.8) is valid and accurately simulates the radial mode.

7.1.3 Infinitesimal Dipole in Free Space

Analytic Solution

Next, the SW-FDTD module was verified more rigourously by comparing with the analytic solutions for an infinitesimal dipole. Every mode in a spherical wave is actually a combination of the radiation from rudimentary dipoles and loops (i.e. multi-poles), and so it is useful to examine the lowest order $n = 1$ TM mode, which represents the infinitesimal

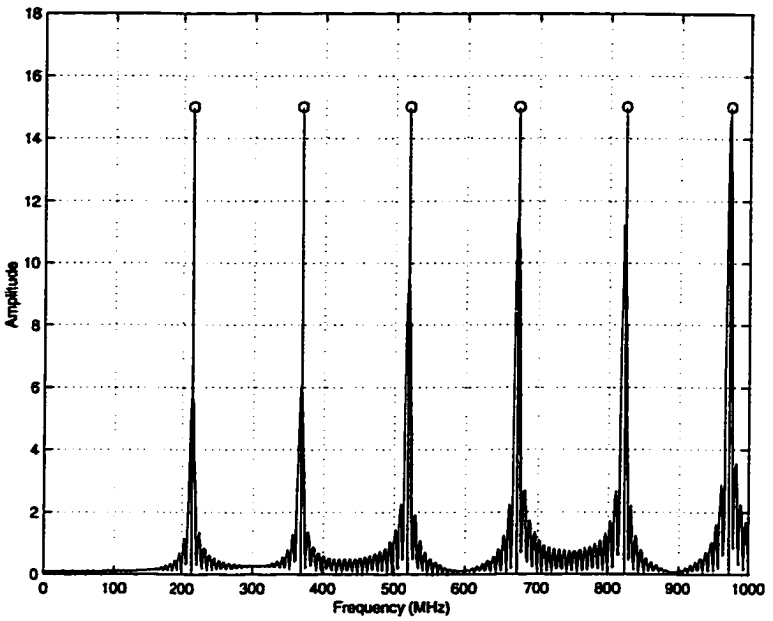

Figure 7.1: TE resonances for a conducting sphere of radius 1m and for the mode index $n = 1$. Stem-lines indicate the analytic solutions and the continuous line indicates the computed solution.

dipole. The z-directed dipole is represented by the $m = 0$ mode. The analytic radiation fields [74] are given as equations (7.3). All other fields are zero everywhere.

$$E_r = ke^{j(\omega t - kr)} \cos\theta \left[-\frac{1}{(kr)^2} + \frac{j}{(kr)^3} \right] \tag{7.3a}$$

$$E_\theta = \frac{k}{2} e^{j(\omega t - kr)} \sin\theta \left[-\frac{j}{kr} - \frac{1}{(kr)^2} + \frac{j}{(kr)^3} \right] \tag{7.3b}$$

$$H_\varphi = \frac{k}{2} \sqrt{\frac{\varepsilon}{\mu}} e^{j(\omega t - kr)} \sin\theta \left[-\frac{j}{kr} - \frac{1}{(kr)^2} \right] \tag{7.3c}$$

Computed Results and Interpretations

The infinitesimal dipole is simulated by utilizing equations (5.8), (5.11), and (5.12) for the TM mode and $n = 1$. The angular dependencies are ignored. It is sufficient to focus on the discretized modal amplitude equations, as angular functions are added as required by

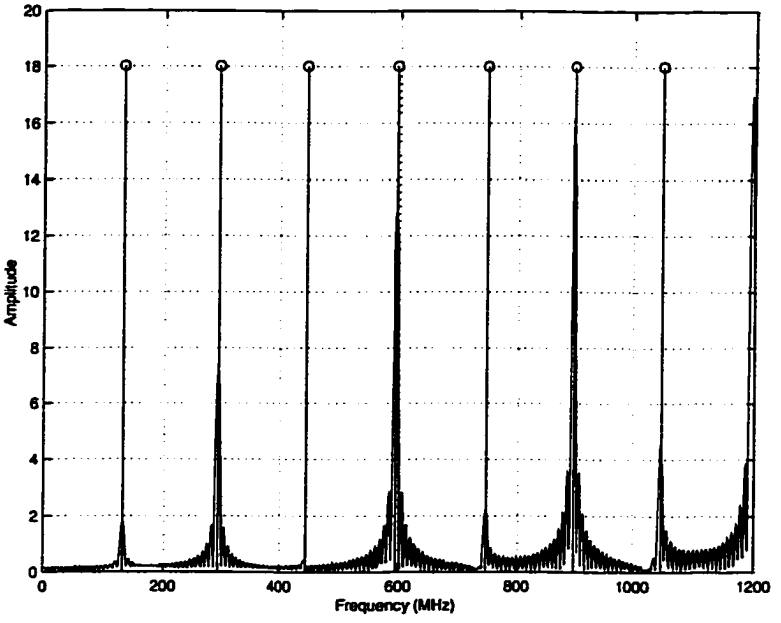

Figure 7.2: TM resonances for a conducting sphere of radius 1m and for the mode index $n = 1$. Stem-lines indicate the analytic solutions and the continuous line indicates the computed solution.

pre-processing analytic values. A discretized domain is established with minimum radius $r_{\min} = 1\,\mathrm{m}$ and maximum radius $r_{\max} = 4\,\mathrm{m}$ at a discretization of $dr = 0.01\,\mathrm{m}$. The first order Mur boundary condition (6.25) has been implemented at the boundary. The time discretization is set to $dt = 14\,\mathrm{ps}$, and the simulation is allowed to progress for 1000 time-steps.

A sinusoidal time-dependence is assumed for the source at a frequency of 1 GHz. To initiate the source function properly for each component, the proper phase shift is applied between components as determined from equations (7.3). The time functions are instituted as hard sources at the minimum radius for each component.

The computed signal for the radial and polar electric field amplitude functions at timestep 1000 (for the entire domain) are plotted in Figures 7.3 and 7.4, showing the

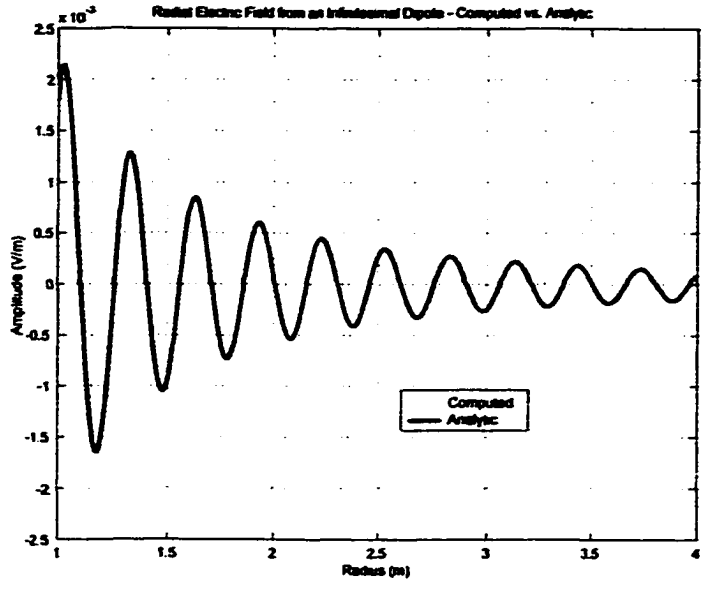

Figure 7.3: Radial electric field amplitude function from an infinitesimal dipole - Computed vs. Analytic, with Mur 1st order boundary bondition

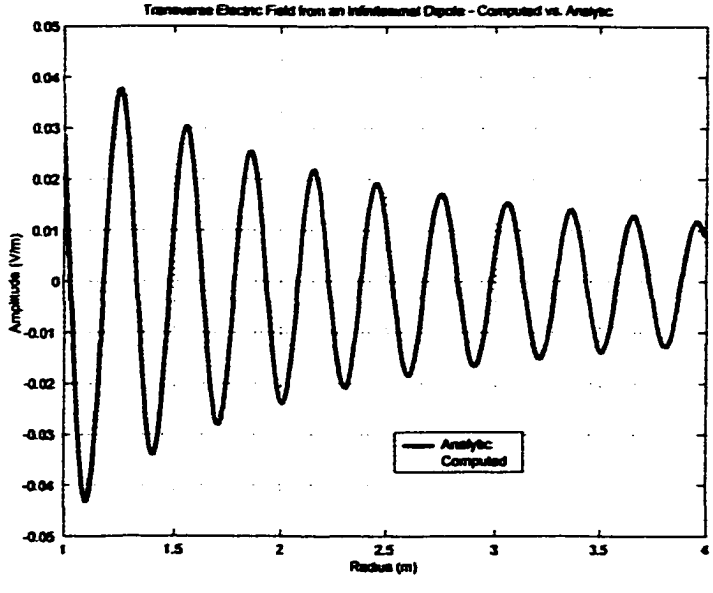

Figure 7.4: Polar electric field amplitude function from an infinitesimal dipole - Computed vs. Analytic, with Mur 1st order boundary condition

computed signal versus the analytic. Qualitatively very good results are shown. When the difference in the computed versus analytic signal is calculated, and referenced to an analytic maximum field value near the boundary, the typical error is in the range of 1-5%. This is similar to the error reported for Mur first order boundary conditions for standard FDTD programs. These results show that the Mur first order boundary condition is successful in terminating the computational boundary with a reasonable error.

Second order Mur conditions (6.24) were programmed and the comparison performed as well, but with no significant decrease in the error. This indicates that there is some other mechanism that is introducing reflection into the computational domain. At this time, it is postulated that this could be the result of three reasons:

1. Dispersion: the numerical phase velocity of the signal is not exactly the same as the analytic solution. As a result the computed signal may lag the analytic by a small percentage. Virtually all numerical schemes have such a dispersive nature.

2. Velocity Mismatch at the Boundary: the Mur boundary condition imposes the theoretical phase velocity c at the outer grid point. Because of the dispersive nature of the numerical scheme, the phase velocity is less than this. As a result, at the boundary there is a mismatch in numerical velocities, and numerical reflections result.

3. Abrupt Signal Start: the source signal used is not truly harmonic, since for $t < 0$ the signal is zero. Hence there is an abrupt "turn-on" of the signal at $t = 0$. When this signal edge reaches the outer boundary, it may introduce reflections back into the domain which continue to "ring" throughout the simulation.

7.1.4 Multi-Mode Test: Dipole Near a Sphere

This section compares computed results with analytic distributions for a more complicated structure involving multiple modes: a dipole near a conducting sphere. The aim of this comparison is threefold. The first aim is simply to confirm that higher order modes, and a combination and summation of modes, can be simulated accurately and completely. This includes incorporation of the angular functions as elements to be considered. The second aim is to quantify the computational savings that can be achieved. For this goal, we must select test cases that can be implemented within the existing FDTD program as well as in the spherical wave FDTD program. This way comparisons can be made to assess computer resource usage. The final aim is to provide more data on the limitations of the method.

Bowman et al. [83] provide the solution for electromagnetic scattering from a perfectly conducting sphere with an infinitesimal dipole located in the vicinity of the sphere (see figure 7.5). In this discussion, the following notation will be used:

$$
\begin{aligned}
\psi_n(x) &= x j_n(x) \\
\zeta_n(x) &= x h_n^{(2)}(x) \\
\psi_n'(x) &= \frac{d}{dx}\left[x j_n(x)\right] \\
\zeta_n'(x) &= \frac{d}{dx}\left[x h_n^{(2)}(x)\right] \\
a_n &= \frac{\psi_n(ka)}{\zeta_n(ka)} \\
b_n &= \frac{\psi_n'(ka)}{\zeta_n'(ka)}
\end{aligned}
$$

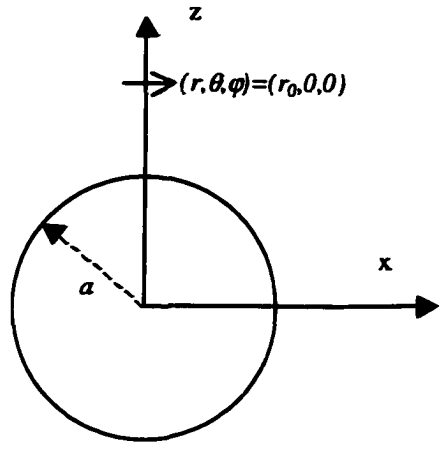

Figure 7.5: Geometry for the problem of a Hertzian dipole near a conducting sphere

with a being the radius of the sphere. For an x-directed electric dipole at $\overrightarrow{r}_0 = (r_0, 0, 0)$, with moment $(4\pi\epsilon_0/k)\hat{x}$, the total fields in polar coordinates are given by,

$$\overrightarrow{E} = jk^2 \sum_{n=1}^{\infty} \left(a_{oln}^{(2)} \overrightarrow{m}_{oln}^{(2)} + b_{eln}^{(2)} \overrightarrow{n}_{eln}^{(2)} \right) e^{j\omega t} \tag{7.4}$$

$$\overrightarrow{H} = k^2 Y \sum_{n=1}^{\infty} \left(a_{oln}^{(2)} \overrightarrow{n}_{oln}^{(2)} + b_{eln}^{(2)} \overrightarrow{m}_{eln}^{(2)} \right) e^{j\omega t} \tag{7.5}$$

where

$$a_{oln}^{(2)} = \frac{2n+1}{n(n+1)} \frac{1}{kr_0} \left[\psi_n(kr_0) - a_n \zeta_n(kr_0) \right] \tag{7.6}$$

$$b_{eln}^{(2)} = \frac{2n+1}{n(n+1)} \frac{1}{kr_0} \left[\psi_n'(kr_0) - b_n \zeta_n'(kr_0) \right] \tag{7.7}$$

This case only consists of $m = 1$ modes.

Sample Cases, Results and Discussion

For comparing analytic solutions to computed solutions, three test cases of differing sphere size are presented. The cases are chosen to test situations where the sphere is 1)

Table 7.2: Test Cases

Label	small	medium	large
Radius of sphere a (metres)	0.1	0.2	1.0
$kr_0 = k(a + 0.25)$	3.5	4.5	12.5
Number of Modes Used N	5	7	15
Start Radius (metres)	0.4	0.5	1.4

much smaller than a wavelength; 2) approximately half a wavelength (in diameter); and 3) larger than one wavelength. The cases are referred to as small, medium, and large, henceforth. For all cases, the frequency of the radiated signal is chosen as $f = 0.5\,\text{GHz}$, giving a wavelength $\lambda = 0.6\,\text{m}$, for a wavenumber $k = \frac{10\pi}{3}\,\text{m}^{-1} \simeq 10.47\,\text{m}^{-1}$. The radial and time resolutions are $dr = 0.01\,\text{m}$ and $dt = 14\,\text{ps}$, respectively; and 300 radial steps are used (starting at the Start Radius). Simulations are allowed to progress for 1000 time-steps. Also, the dipole is always located 0.25 m from the sphere surface. Table 7.2 summarizes the cases.

Computed results for E_θ are shown in Figures 7.6 through 7.11 for $0 \leq \theta \leq \pi$ in $\frac{\pi}{60}$ increments, and for $\varphi = 0$. Therefore, the horizontal axis is the z-axis, and the vertical axis is the x-axis. Solutions are also only shown for the last 200 or so radial steps, to avoid having nearer-field wave amplitudes swamping out the further-field amplitudes. Comparing the figures qualitatively, very good accuracy is attained once again. Errors still are in the 1-5% range due to dispersion and/or boundary condition errors.

7.1.5 Discussion

The previous subsections have progressively shown that the propagation of spherical waves can be successfully and relatively accurately modeled in an explicit finite difference

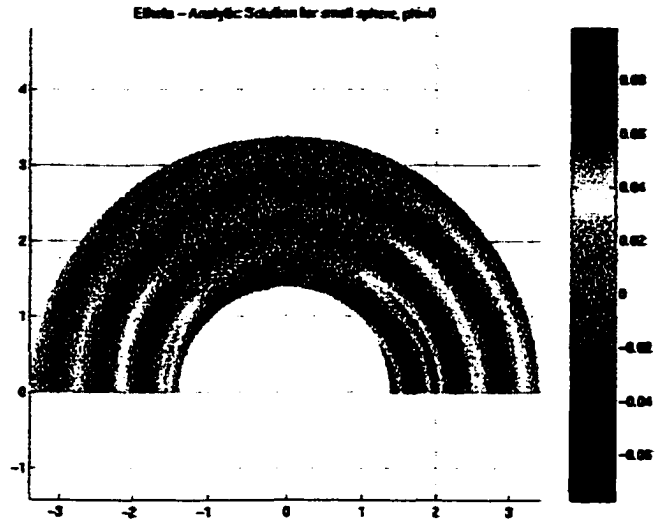

Figure 7.6: Analytic electric field amplitude E_θ in V/m at $\varphi = 0$ for the small sphere case

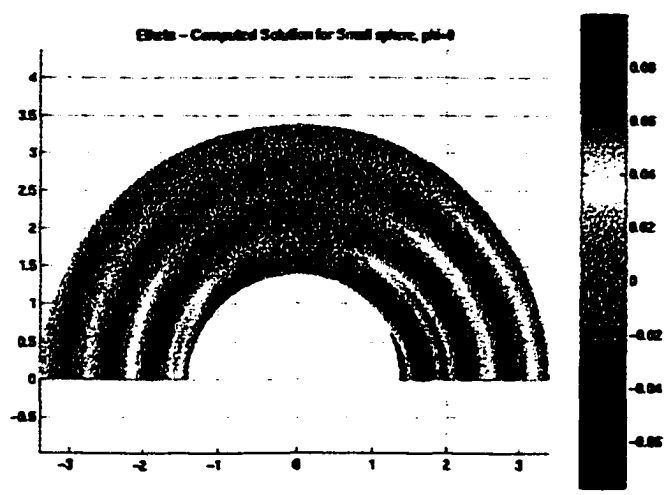

Figure 7.7: Computed electric field amplitude E_θ in V/m at $\varphi = 0$ for the emall sphere case

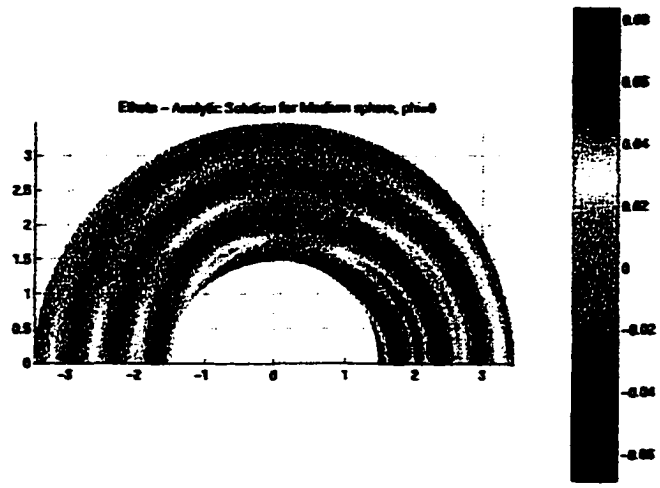

Figure 7.8: Analytic electric field amplitude E_θ in V/m at $\varphi = 0$ for the medium sphere case

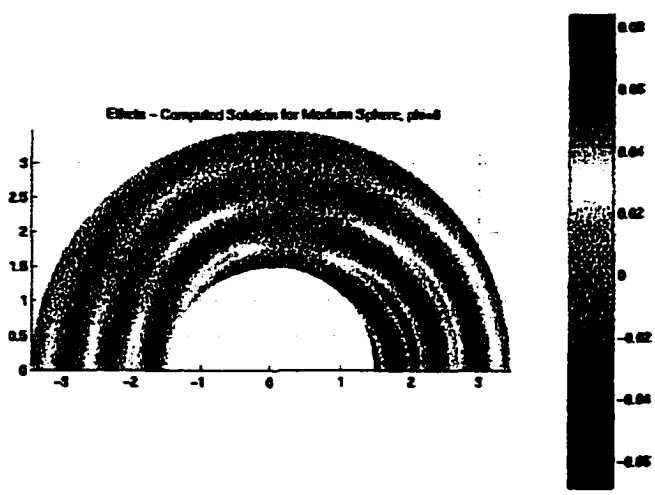

Figure 7.9: Computed electric field amplitude E_θ in V/m at $\varphi = 0$ for the Medium sphere case

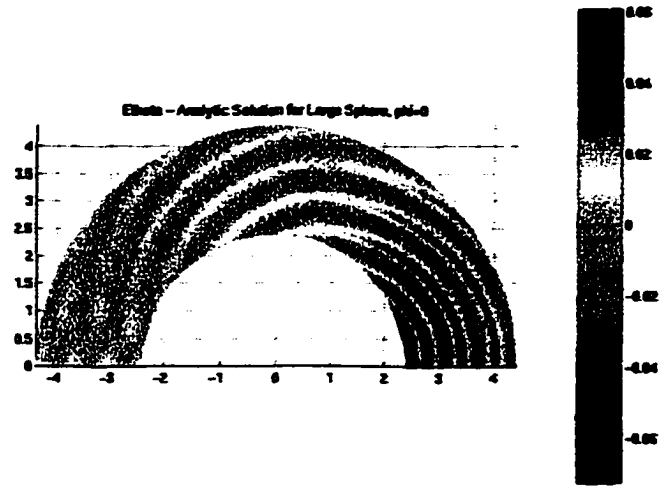

Figure 7.10: Analytic electric field amplitude E_θ in V $/m$ at $\varphi = 0$ for the Large sphere case

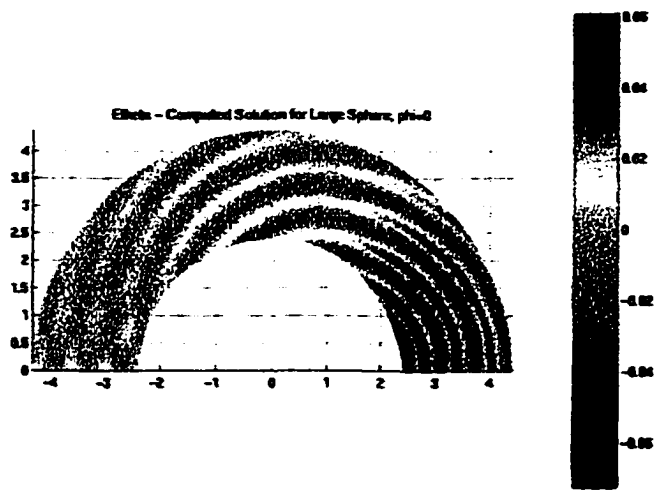

Figure 7.11: Computed electric field amplitude E_θ in V $/m$ at $\varphi = 0$ for the Large sphere case

time domain method. Although there are still some errors, these can be accounted for, and the method at least represents very good promise for successful modeling with a reasonable degree of accuracy. The amplitude functions determined from the difference equations represent the radial and time dependence well, and the multi-mode cases demonstrate that the angular functions have been successfully incorporated. The method should then be useful as a source condition in the total/scattered field FDTD formulation.

7.2 Incorporation With Cartesian FDTD

7.2.1 Method of Synthesis

The SW-FDTD program component has been synthesized with an existing FDTD program in Cartesian coordinates. This synthesis treats the spherical wave modes as source conditions for the total/scattered field methodology described in earlier chapters. To accomplish this, the SW-FDTD program must run concurrently with the standard FDTD, with modal incident values being interpolated at each time step for each point on the Huygens' surface.

For each point on the Huygens' surface, the angular function values determined in pre-processing for each mode are stored. Since field components are not physically co-located, these function values are calculated for each of the six field components as well. Assuming a Huygens' surface spanning a region of size $N_x \times N_y \times N_z$, and for three angular functions and six field components, and for a modal expansion to order N, the total number of values required to be stored is then $2\,(N_xN_y + N_xN_z + N_yN_z) \cdot 2N(N+2) \cdot 3 \cdot 6 = 72\,(N_xN_y + N_xN_z + N_yN_z) \cdot N(N+2)$ values.

To maintain consistency with the Cartesian FDTD program, the radial increment dr and the time increment dt in the SW-FDTD program is set to be the same as in the Cartesian FDTD program. Each point on the Huygens' surface also lies at a distance r from the spherical wave origin. This distance is calculated "on-the-fly" during program execution, and spherical component amplitude functions are interpolated from the modes propagated via the difference equations. The spherical components are then projected onto Cartesian components to get the final value of the incident field for a particular point on the surface.

7.2.2 Method of Validation

The synthesis of the programs is validated with two simple cases, and in three different ways. In each case, the computational domain for the spherical wave part of the test is a $50\,\text{cm} \times 50\,\text{cm} \times 50\,\text{cm}$ empty domain in the positive x, y, and z directions with Huygens' surfaces at 3 cm and 47 cm in each direction. The spatial increment is $\Delta x = \Delta y = \Delta z = \Delta r = 1\,\text{cm}$, giving a computational domain of $50 \times 50 \times 50$ cells. The frequency of the source is 500 MHz, and the simulation is allowed to progress for 400 timesteps. The Cartesian FDTD domain is truncated by $PML(7, P, 70dB)$ on all sides.

The first case is a simple, z-directed infinitesimal dipole, located at $(x, y, z) = (25\,\text{cm}, -10\,\text{cm}, 25\,\text{cm})$. It is expected that the dominant electric field in the domain is the E_z field. In terms of spherical waves, this consists of only the one mode indicated earlier for equations (7.3). The geometry is indicated in figure 7.12a).

The second case studied is the same general configuration of the dipole near a conducting sphere indicated in an earlier section. Due to the memory restrictions of the

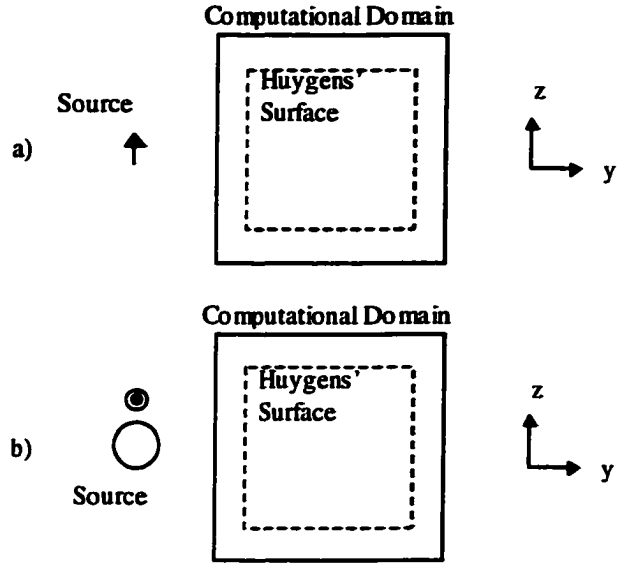

Figure 7.12: Geometry for validation tests: a) simple dipole source; and b) dipole near conducting sphere

computer used, a different configuration is used than that previously investigated. Instead, a configuration with $N = 4$ modes is utilized, assuming a sphere of radius $r_s = 15\,\text{cm}$ with the dipole situated 7 cm directly above the sphere. The spherical wave origin for this configuration is located at $(x, y, z) = (25\,\text{cm}, -30\,\text{cm}, 25\,\text{cm})$. The geometry is indicated in figure 7.12b).

First, the cases are compared with the analytic solutions in the entire volume at timestep 300 to determine accuracy. Second, representative time series are taken inside the total field region at $(x = 25\,\text{cm}, y = \{4, 15, 25, 40\}\,\text{cm}, z = 25\,\text{cm})$ and just outside the total field region at $(x = 25\,\text{cm}, y = 2\,\text{cm}, z = 25\,\text{cm})$. These are used to give an indication of any error fields, and the relative strength of these error fields. Finally, for the second case, the sphere and dipole are modeled explicitly within another computational domain of size $50\,\text{cm} \times 100\,\text{cm} \times 50\,\text{cm}$, with the sphere centred at $(x = 25\,\text{cm}, y = 20\,\text{cm}, z = 25\,\text{cm})$. This

is used to compare the computational efficiency of the method by comparing runtimes.

Note that the results computed with the SW-FDTD method can *not* be compared with explicit FDTD simulations temporally, because there is no way to ensure that the comparisons are in phase. This can be understood in the following way. Imagine that a simple dipole source is modeled explicitly; an electric field location representing the source is essentially utilized as a hard source from the point of view of simulation. To model the dipole implicitly requires setting up a one-dimensional modal grid that represents the source starting *from some minimum radius*. There is no way to ensure that the phases of both simulations are matched for direct comparison at some other set of field points. For this reason, validation is presented by comparison with analytic solutions determined from spherical wave theory.

7.2.3 Simple Dipole Results

The electric field components at representative cross-sections are plotted in figures 7.13-7.15 for an x-plane off centre from the spherical wave origin, and in figures 7.16-7.18 for an x-plane aligned close to the spherical wave origin. Analytic versus computed fields are shown. The analytic fields are determined exactly at the node vertex locations, whereas computed fields are derived from their physical location in the Yee cell, and so some asymmetries may exist in the figures. Note that the dipole simulated is located to the left of the graphs, and thus propagation is, in general, going from left to right.

Figures 7.19 - 7.23 show the time progression of the signal at the locations discussed in the previous section. Figure 7.20 shows the field in the scattered field region (at $y =$ 2cm), which indicates the error. These fields should be compared in terms of relative

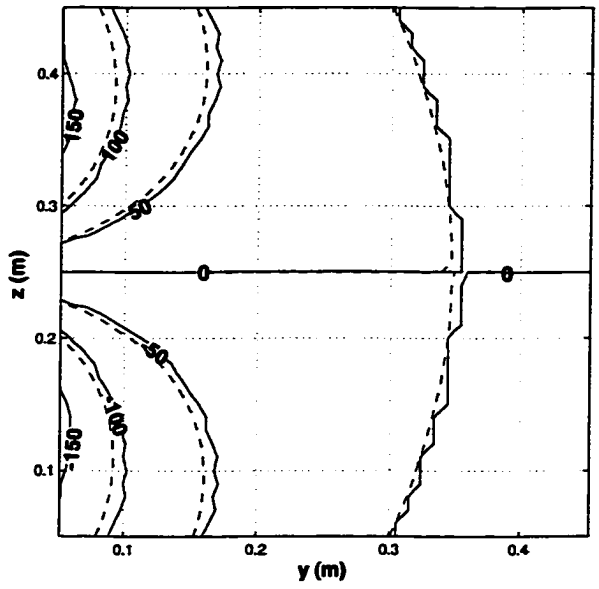

Figure 7.13: Simple dipole - electric field amplitude ($m\,\mathrm{V}\,/\,\mathrm{m}$) E_x at the $x = 14\,\mathrm{cm}$ plane, analytic (—) vs. computed (- - -) at timestep 300

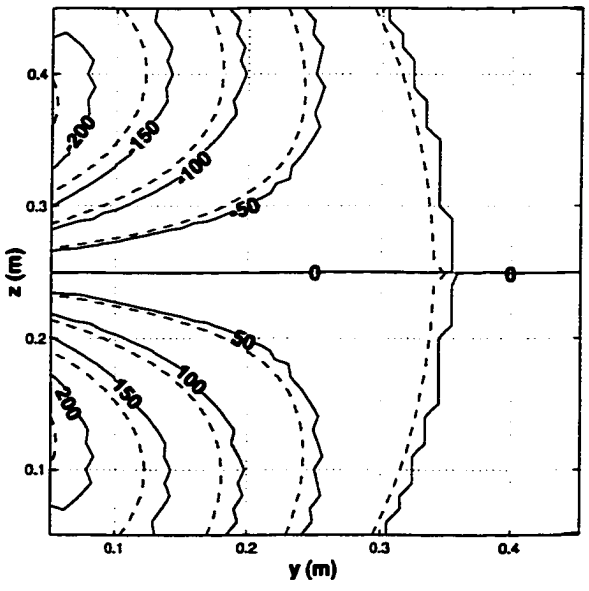

Figure 7.14: Simple dipole - electric field amplitude ($m\,\mathrm{V}\,/\,\mathrm{m}$) E_y at the $x = 14\,\mathrm{cm}$ plane, analytic (—) vs. computed (- - -) at timestep 300

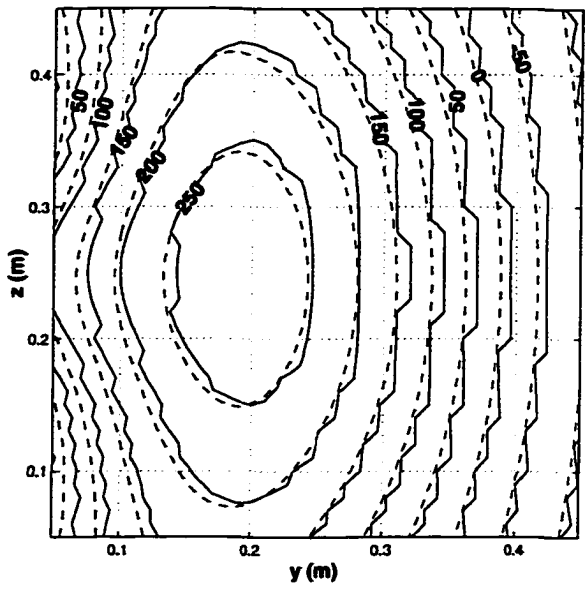

Figure 7.15: Simple dipole - electric field amplitude ($m\,\mathrm{V}\,/\,\mathrm{m}$) E_z at the $x = 14\,\mathrm{cm}$ plane, analytic (—) vs. computed (- - -) at timestep 300

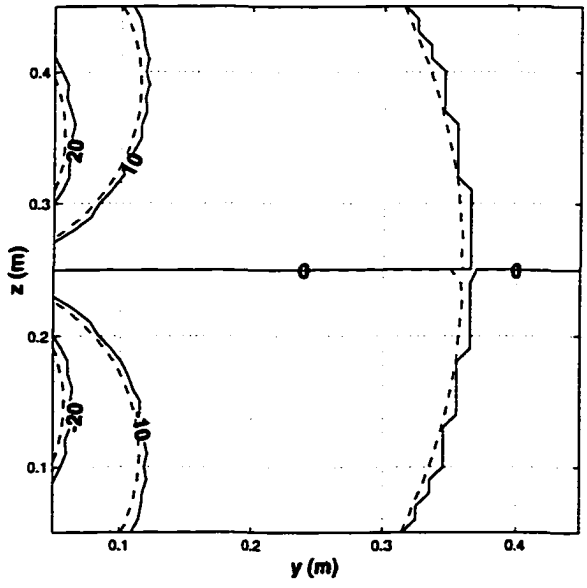

Figure 7.16: Simple dipole - electric field amplitude ($m\,\mathrm{V}\,/\,\mathrm{m}$) E_z at the $x = 24\,\mathrm{cm}$ plane, analytic (—) vs. computed (- - -) at timestep 300

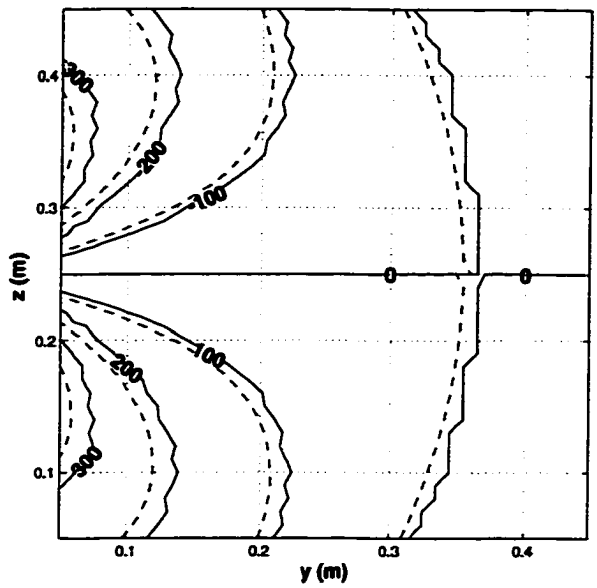

Figure 7.17: Simple dipole - electric field amplitude ($m\,\mathrm{V}\,/\,\mathrm{m}$) E_y at the $x = 24\,\mathrm{cm}$ plane, analytic (—) vs. computed (- - -) at timestep 300

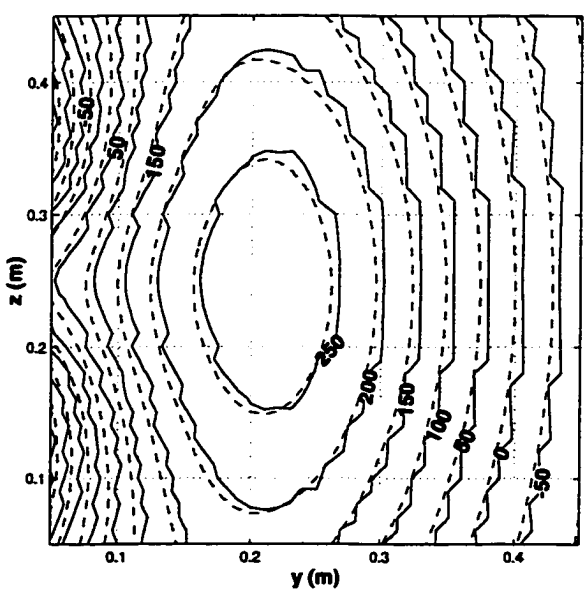

Figure 7.18: Simple dipole - electric field amplitude ($m\,\mathrm{V}\,/\,\mathrm{m}$) E_z at the $x = 24\,\mathrm{cm}$ plane, analytic (—) vs. computed (- - -) at timestep 300

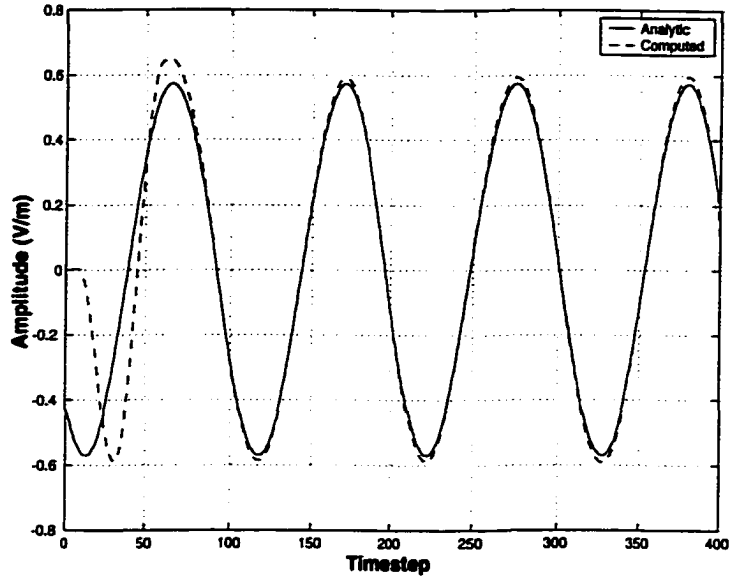

Figure 7.19: Simple Dipole - E_z electric field amplitude (V / m) at $y = 4\,\text{cm}$ - computed vs. analytic

amplitude with Figure 7.19, which indicates the time signal at the next closest point (at $y = 4\,\text{cm}$) . Successive figures indicate time signals at points progressively further from the source.

The contour figures 7.13 - 7.18 appear to show the simulated spherical waves lagging behind the analytic solutions in all instances. A plausible explanation is that the contour lines of the computed signal may be skewed because of slightly different amplitudes in computed and analytic signals.

Despite these concerns, the spherical wave solution seems to propagate well while coupled with the Cartesian FDTD, and with reasonable accuracy. The error field is approximately 0.16% relative to the propagating field (nearest point).

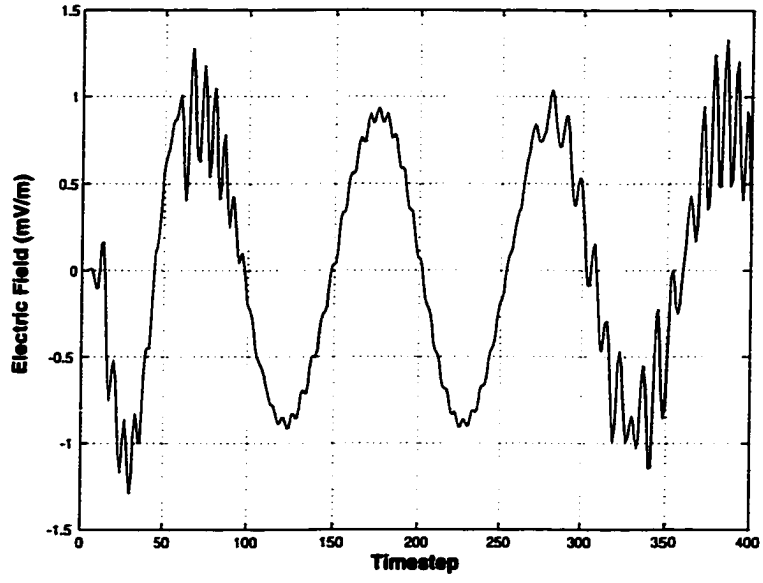

Figure 7.20: Simple Dipole - E_z electric field amplitude ($m\,\mathrm{V}/\mathrm{m}$) in the scattered field region at $y = 4\,\mathrm{cm}$ indicating the error field.

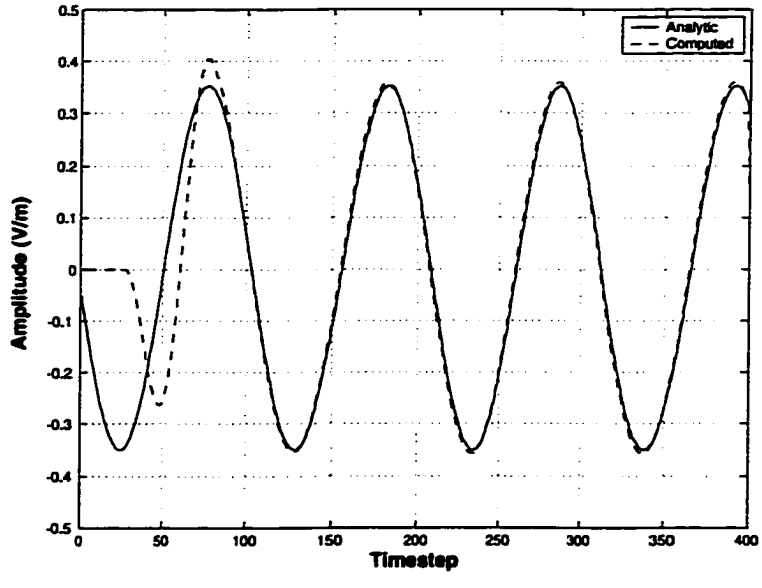

Figure 7.21: Simple Dipole - E_z electric field amplitude (V/m) at $y = 15\,\mathrm{cm}$ - computed vs. analytic

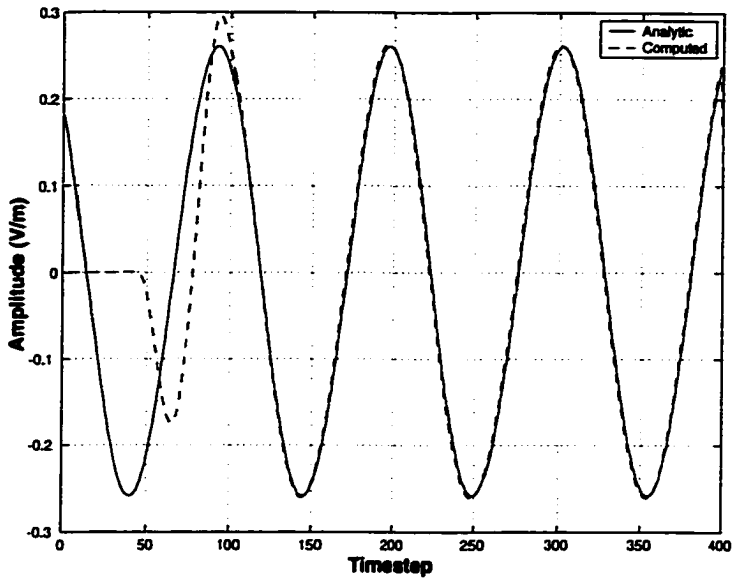

Figure 7.22: Simple Dipole - E_z electric field amplitude (V / m) at $y = 25\,\text{cm}$ - computed vs. analytic

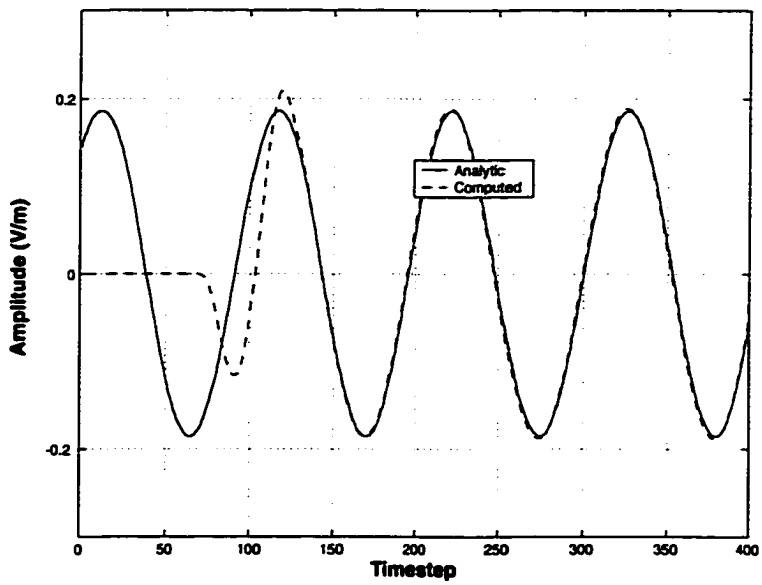

Figure 7.23: Simple Dipole - E_z electric field amplitude (V / m) at $y = 40\,\text{cm}$ - computed vs. analytic

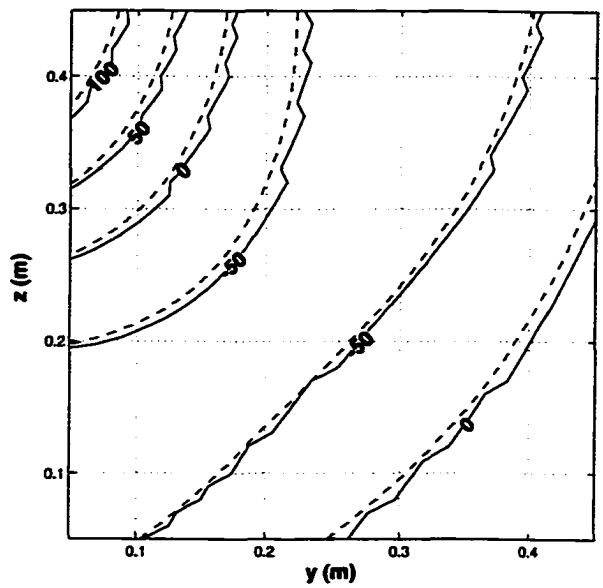

Figure 7.24: Multi-mode - E_x electric field amplitude ($m\,\mathrm{V/m}$) at the $x = 24\,\mathrm{cm}$ plane, analytic (—) vs. computed (- - -) at timestep 300

7.2.4 Multi-Mode Results

The electric field components in the multi-mode case are plotted in two perpendicular representative planes ($x = 24\,\mathrm{cm}$, $z = 24\,\mathrm{cm}$) near the centreline of the spherical wave origin. The y-direction indicates the general direction of propagation. Figures 7.24-7.26 plot the x-plane, and figures 7.27-7.29 plot the z-plane. Once again the simulated fields seem to lag the analytic solutions. We believe the same postulates regarding the reasons behind such behaviour still hold true.

Plots of the time signals at points progressively further from the source are indicated in Figures 7.30 - 7.33. In this case the error field indicated in figure 7.30 is much larger in relative terms (approximately 5%), and shows the same periodicity as the total field. For the previous case, only one mode was present in the simulation, whereas for this

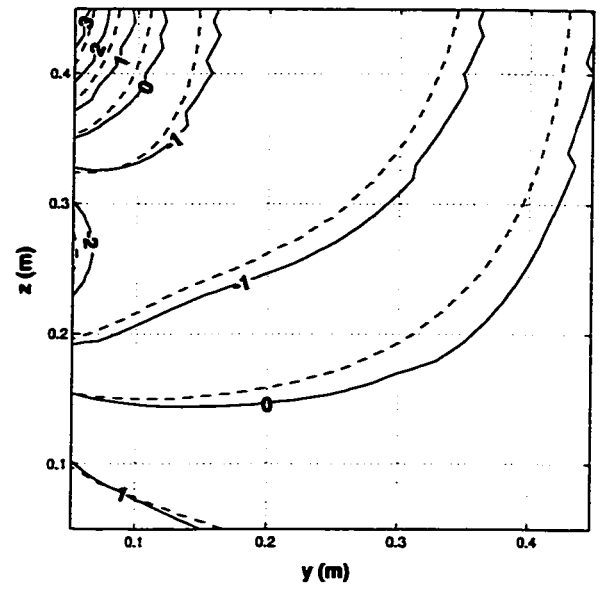

Figure 7.25: Multi-mode - E_y electric field amplitude ($m\,\mathrm{V/m}$) at the $x = 24\,\mathrm{cm}$ plane, analytic (—) vs. computed (- - -) at timestep 300

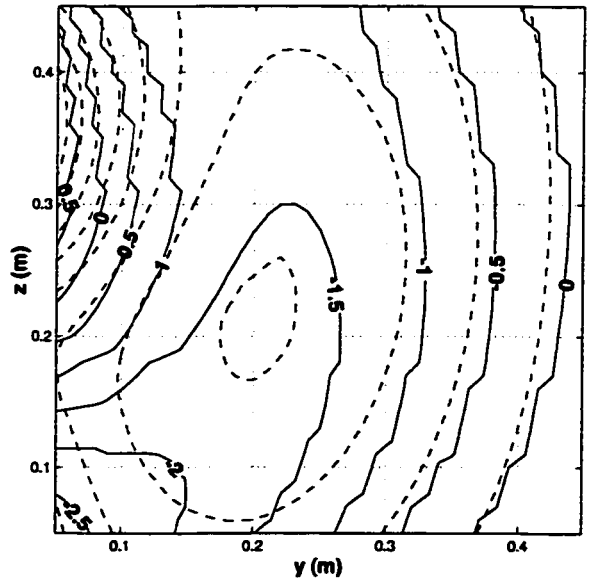

Figure 7.26: Multi-mode - E_z electric field amplitude ($m\,\mathrm{V/m}$) at the $x = 24\,\mathrm{cm}$ plane, analytic (—) vs. computed (- - -) at timestep 300

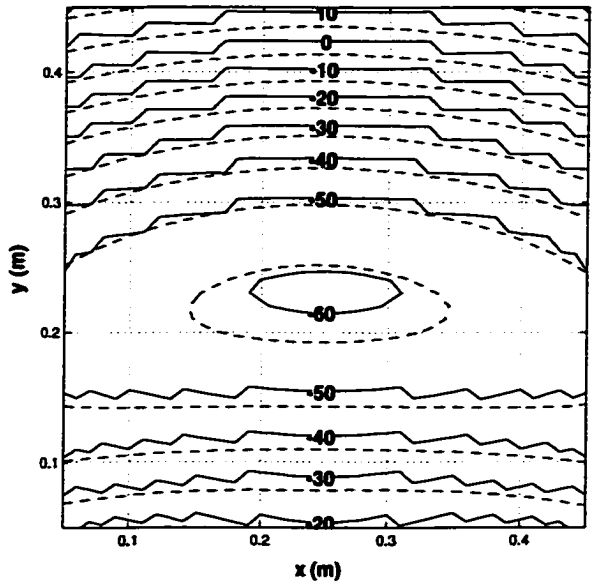

Figure 7.27: Multi-mode - E_x electric field amplitude ($m\,\mathrm{V}/\mathrm{m}$) at the $z = 24\,\mathrm{cm}$ plane, analytic (—) vs. computed (- - -) at timestep 300

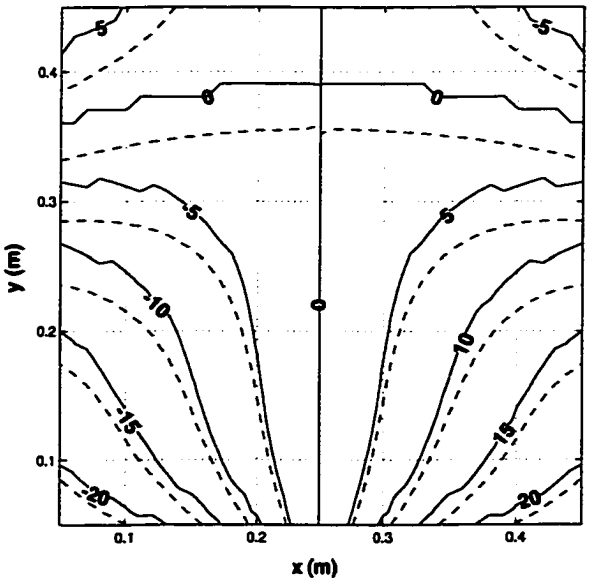

Figure 7.28: Multi-mode - E_y electric field amplitude ($m\,\mathrm{V}/\mathrm{m}$) at the $z = 24\,\mathrm{cm}$ plane, analytic (—) vs. computed (- - -) at timestep 300

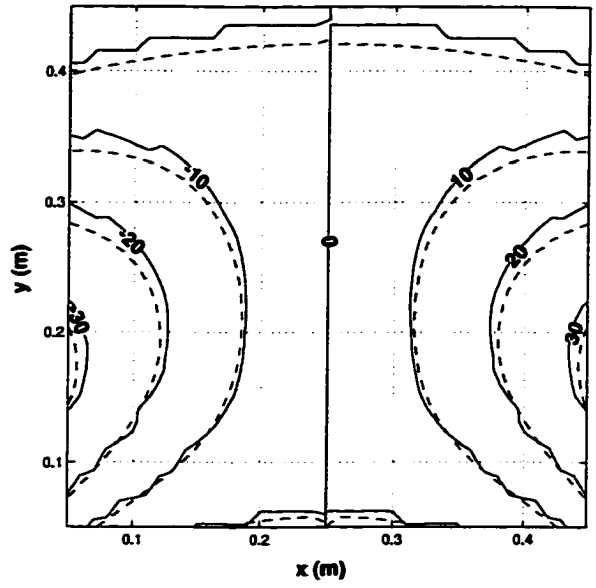

Figure 7.29: Multi-mode - E_z electric field amplitude ($m\,\mathrm{V}/\mathrm{m}$) at the $z = 24\,\mathrm{cm}$ plane, analytic (—) vs. computed (- - -) at timestep 300

case, there are eight modes with non-zero modal coefficients.

Finally, a cursory investigation of the computational efficiency of the implicit spherical wave source and the explicit modeling is made. Table 7.4 indicates the results of this comparison.

	Runtime	**Memory Usage**
Explicit	13 min	280 MBytes
Implicit	48 min	1300 MBytes

Table 7.3: Comparison of Computational Efficiency for the SW-FDTD method

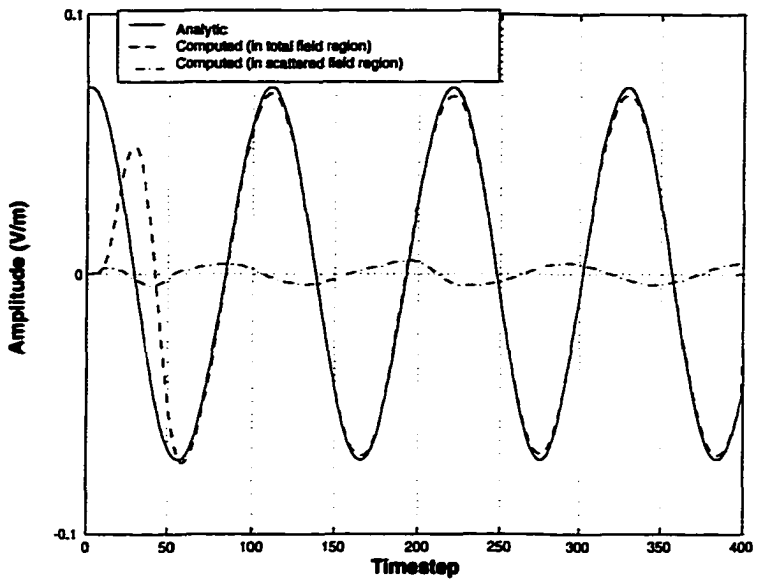

Figure 7.30: Multi-mode - E_x electric field amplitude (V / m) at $y = 4\,\text{cm}$ - computed vs. analytic, and the error field

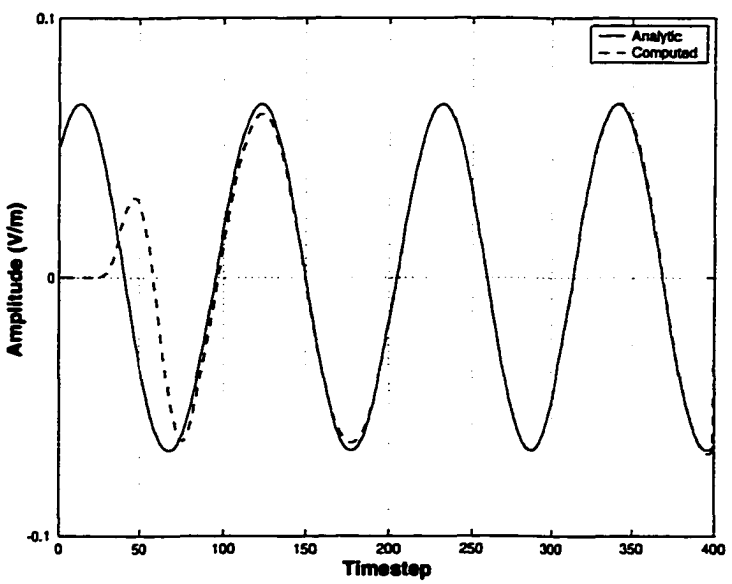

Figure 7.31: Multi-mode - E_x electric field amplitude (V / m) at $y = 15\,\text{cm}$ - computed vs. analytic

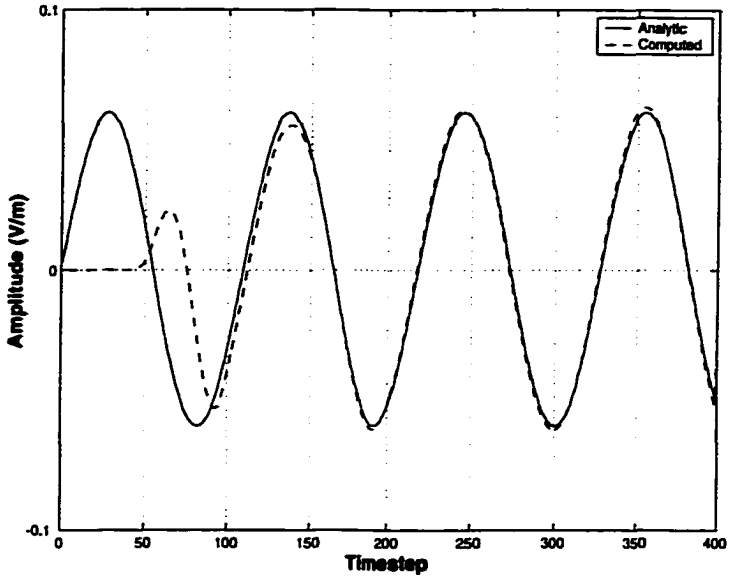

Figure 7.32: Multi-mode - E_z electric field amplitude (V / m) at $y = 25\,\text{cm}$ - computed vs. analytic

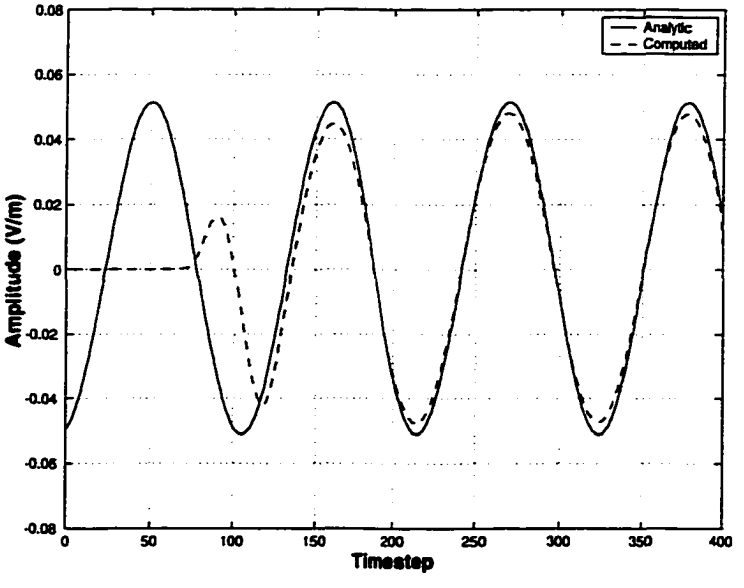

Figure 7.33: Multi-mode - E_z electric field amplitude (V / m) at $y = 40\,\text{cm}$ - computed vs. analytic

7.2.5 Discussion

Efficiency

The SW-FDTD method does not appear to be as efficient as initially expected. This is due to two main reasons: the memory usage of the look-up table for the angular functions, and for the modal grids. Both these reasons will be discussed shortly, but first the crude results presented need to be evaluated. It must be noted that the comparison of the computational efficiency is meant to give a rough indication of how the SW-FDTD method is performing. It is not necessarily a fair comparison to make for several reasons. First, the explicit modeling is performed with a computer program which is fully optimized and runs partially in parallel. The SW-FDTD modules are not optimized, nor are they running in parallel. In particular, there is no sophisticated memory access via multi-layer pointers. This approach needs to be examined further in future renditions of the SW-FDTD code. Furthermore, it is worthwhile to examine some of the inefficiencies that could be alleviated in the future.

The increase in memory usage is understandable, especially since the number of values to be stored for the angular functions is

$$N_a = \{72\,(N_xN_y + N_xN_z + N_yN_z) \cdot N(N+2)\}\,.$$

It is anticipated that for a certain domain size $\{N_x \times N_y \times N_z\}$ and with a certain number of modes in the expansion, N, it will be more efficient to simply calculate the angular functions during runtime. These calculations may prove faster than accessing values from a lookup table. Another way to alleviate this problem may be to calculate a grid of simple angular function values for the Huygens' surface. Using this grid for interpolation, other

function values could be calculated through clever use of recurrence relations.

Referring to the storage required for the modal equations, it is expected that some savings can still be achieved. For instance, in Table 5.1 it can be seen that the radial and time dependence (i.e. in essence, the amplitude function) for the angular components for the TE and TM modes are identical aside from a sign change in some instances. Currently, each of the components is still calculated and stored. Memory requirements could be reduced by only calculating and storing one of these, and applying the sign change as required when calling for a field value. The number of values that need to be stored for the modal equations extending for N_r gridpoints is $24N_rN(N+2)$ (six fields, TE and TM, even and odd, and for two timesteps). With the anticipated savings this can be reduced by a factor of three to $8N_rN(N+2)$.

It should be emphasized that the efficiency comparison is made for the case where the area of interest is directly adjacent to the radius of the spherical wave expansion $r_{\min}$. The radiative near-field of the source is approximately defined where $N < kr < N^2$, and the rule-of-thumb used for determining the expansion order is $N \simeq kr_{\min}$. This means that the region of applicability can be represented by

$$L = \frac{r}{r_{\min}} < N$$

Thus, if the area of interest is chosen to be L more wavelengths beyond $r_{\min}$, then the runtime for the SW-FDTD would remain the same but the explicit method requirements would increase by the factor L. For electrically larger sources (i.e. larger N) the SW-FDTD method should, therefore, have an advantage. This argument indicates that the method presented here is still likely a viable option for simulations. Further investigation needs

to be carried out to quantify the computer resource issues for the SW-FDTD. Another likely possibility is that, for specific configurations at larger distances, fewer modes may be required for accurate representation, thereby speeding up computations.

Errors

In both the single mode (simple dipole) and multi-mode test cases, the computed time signals indicate deviations from the analytic solutions. The multi-mode case shows far greater error, and this is probably a result of carrying multiple modes. It is postulated that any error in this regard is most likely because of a "mismatch" between the finite difference grids.

The coupling of the spherical wave modes to the Cartesian FDTD method can be conceptualized as a transmission line network: one section of line, representing a mode, connected to the network representing the Huygens' surface. Since these sections are represented by different finite-difference schemes, there is a mismatch at the interface, resulting in a reflected field at the Huygens' surface. The additive error of all these modes then leads to an increase in the overall error. The mismatch is likely a result of different dispersion characteristics in the finite difference methods, especially considering that dispersion increases with increasing mode order n, as indicated in Chapter 6.

A way to confirm that dispersion for higher order modes is indeed another principal contributor to the errors would be to study the coupling effects of higher order modes one by one, and investigate their contribution to the total error. It is quite reasonable to expect that these problems can be mitigated by proper matching of each mode to the standard grid. Similar problems were encountered with incorporation of plane waves as sources in

the total/scattered field method; and by compensating for the numerical phase velocity, a better match and smaller errors were achieved. Further research needs to be performed to investigate these solutions.

Another possible source of error is the reflected signal from imperfect boundary conditions. This may have caused greater errors at the Huygens' surface locations far from the source in these simulations, but these errors should have decayed closer to the source. However, from Figure 7.30, it can be noted that the increased error appears immediately, indicating it is not be the result of boundary reflections. This indicates that the most probable, dominant error source is due to the mismatch.

Summary

Overall, the SW-FDTD method is able to simulate sources implicitly with a reasonable degree of accuracy, without having to model the source explicitly. There are still issues to investigate including how to match the two difference schemes, and how to account for numerical dispersion. The method has been implemented in a rudimentary manner to date, and further means can be explored to increase its efficacy and accuracy.

Chapter 8

Conclusions and Future Work

The uniform plane wave source, in combination with the total/scattered field formulation and the equivalence principle, have provided significant impetus in the application of the FDTD method to scattering problems. In particular, the use of an alternate one-dimensional source presents an efficient and attractive method for the solution of such problems. Also, utilizing the FDTD formulation allows for easy application to complex and heterogeneous structures. The main disadvantage resides in the inherent far-field modeling implied in the use of plane wave sources.

This thesis has shown how the total/scattered field formulation can be extended to the efficient modeling of non-uniform wave sources. This in turn leads to the ability to undertake modeling of problems involving scattering in the near-field of sources.

The specific case of modeling of a low frequency, infinite line-source was demonstrated in Chapter 4. In this case, small changes to the existing plane wave source formulation allowed for an efficient method to predict scattering problems in the vicinity of, e.g.

power lines. Verification was provided by comparisons with free-space fields, and with the analytic solutions for a lossy sphere. Finally, a practical example examined the exposure of the human body in proximity to high voltage transmission lines, with the conclusion that the plane wave source is not accurate enough in this near-field scenario.

To extend the utility of the method, Chapter 5 described a method whereby known sources were described by their spherical wave expansion. Utilizing this expansion, an analogy was derived to the one-dimensional plane wave sources that allowed for the propagation of spherical waves by way of modal amplitude equations. Numerical issues regarding the implementation of this method were investigated and classified in Chapter 6. Chapter 7 provided validation of the method by examining the SW-FDTD method as a program module in and of itself, and then by incorporating it with an existing Cartesian FDTD program.

8.1 Summary and Contributions

It is useful at this time to once again refer to figure 5.2, and summarize how close the SW-FDTD method is to realization of this figure. This discussion is broken down into three parts, representing the three parts indicated in the figure.

The first part incorporates expansion of the source configuration into spherical wave modes. The assumption throughout this thesis has been that the modal expansion for the source is a known quantity. In that sense we have fully realized this part of the diagram since the expansion is assumed known a priori. But the method also allows great latitude for an expansion off the algorithm. For instance, the method currently assumes

a mono-chromatic source, but in future can be expanded to include sources with a greater frequency band. This would necessitate a change in the way the one dimensional modes are stimulated with a source function. Furthermore, another extension to the method could be to allow for explicit source modeling with modal expansion computed "on-the-fly." This may be the only method for complicated sources.

The second part of the diagram indicates the one dimensional propagating grids. This thesis has demonstrated that spherical waves can be successfully propagated and simulated numerically with a reasonable degree of accuracy. To realize better accuracy with this method will require i) appropriate modal absorbing boundary conditions; and ii) investigation, classification, and mitigation of dispersion problems.

The final part of the diagram indicates where the angular functions are incorporated in the algorithm, and also how the modes are injected as Huygens' sources. This thesis has shown that incorporation of the angular functions can be done successfully, though not necessarily efficiently. Furthermore, the coupling of the modal grids into the Cartesian grid seems to be where the dispersion problem seems to manifest itself in a mismatch. It is expected that these problems can be mitigated in the future.

Overall, the method as diagrammed in figure 5.2 has been realized, albeit in a preliminary format. The goal of this thesis was simply to indicate that such a method is possible and reasonable. As such, the information presented represents a work in progress, for which refinements to the discussed method will follow in due course. In general, the main contribution of this thesis is to show that non-uniform sources can be accurately modeled, and that efficient methods of implementing these sources can be developed. The

implication is that complicated situations involving near-field object illumination can be modeled in an alternative and attractive manner.

8.2 Future Work

The SW-FDTD method shows promise, but there is still a significant amount of work to be performed before it can be further utilized. There are three tasks that demand attention in the near future: the development of better boundary conditions, the reduction of error and improvement of efficiencies, and the use of time-domain spherical wave coefficients.

Absorbing boundary conditions have not been implemented currently with the modal amplitude equations. It is anticipated that the abundance of methods available for domain termination in the literature provides ample background for a simple method to accomplish this task. There are not any significant challenges anticipated in the successful completion of this task.

The main source of error for impressed fields in the total field domain for the SW-FDTD implementation is believed to be the mismatch in coupling the finite difference methods. For plane wave sources, Taflove elucidates [2] how the phase velocity for waves at different angles of incidence can be corrected by adjusting the propagation constant used in the one-dimensional source grid. Conversely, for the spherical waves, each mode will travel in all directions defined by the Huygens' surface. This will complicate phase velocity adjustment in the SW-FDTD.

Furthermore, the SW-FDTD method can be implemented in a more efficient man-

ner as outlined in Chapter 7. Some changes to memory allocation are simple, whereas further investigation into interpolation schemes and/or look-up table optimization would benefit the method immensely.

Validation to date has assumed a mono-chromatic source, where the spherical wave coefficients are a function of frequency. There is no reason to restrict the modal weights determined from these to single frequencies, however. If the expansion for a particular source can be tracked in the time domain (for instance, as a single FDTD computation for the source radiating into free space), then that time track can be stored and used as a lookup table of propagating modes for timestep-to-timestep . This will greatly enhance the applicability of the method, but possibly at the expense of efficiency.

The demonstration of the viability of non-uniform sources with the line-source, and the validation of the SW-FDTD method show great promise for the progress of modeling near-field situations as an extension to the FDTD method. The main benefit will be the computational savings that can be achieved by not explicitly modeling the source. With the successful accomplishment of the three tasks outlined above, spherical waves as sources in the FDTD method will become a viable alternative to examining problems in the near-field of radiating structures. With this further development, it is believed that better efficiencies and accuracy will be achieved with the SW-FDTD method, providing for attractive modeling options for complicated near-field electromagnetic situations.

Bibliography

[1] K.S.Yee, "Numerical Solutions to Initial Boundary Value Problem Involving Maxwell's Equations in Isotropic Media," *IEEE Transactions on Antennas and Propagation*, vol. 14, pp. 302–307, 1966.

[2] A. Taflove, *Computational Electrodynamics: The Finite Difference Time Domain Method.* Artech House, 1995.

[3] J. Stratton, *Electromagnetic Theory.* New York and London: McGraw-Hill, 1941.

[4] A. Taflove, *Computation of the Electromagnetic Fields and Induced Temperatures Within a Model of the Microwave-Irradiated Human Eye.* Ph.d. dissertation, Northwestern University, Evanston, IL, June 1975.

[5] K. R. Umashankar and A. Taflove, "A Novel Method to Analyze Electromagnetic Scattering of Complex Objects," *IEEE Transactions on Electromagnetic Compatibility*, vol. 24, pp. 397–405, 1982.

[6] G. Mur, "Absorbing Boundary Conditions for the Finite-Difference Approximation of the Time-Domain Electromagnetic Field Equations," *IEEE Transactions on Electromagnetic Compatibility*, vol. 23, pp. 377–382, 1981.

[7] K. S. Kunz and K. M. Lee, "A Three-Dimensional Finite-Difference Solution of the External Response of an Aircraft to a Complex Transient EM Environment: I - The Method and Its Implementation," *IEEE Transactions on Electromagnetic Compatibility*, vol. 20, pp. 328–333, 1978.

[8] K. S. Kunz and K. M. Lee, "A Three-Dimensional Finite-Difference Solution of the External Response of an Aircraft to a Complex Transient EM Environment: II - Comparison of Predictions and Measurements," *IEEE Transactions on Electromagnetic Compatibility*, vol. 20, pp. 333–341, 1978.

[9] R. Holland, "THREDE: A Free-Field EMP Coupling and Scattering Code," *IEEE Transactions on Nuclear Science*, vol. 24, pp. 2416–2421, 1977.

[10] D. E. Merewether, R. Fisher, and F. W. Smith, "On Implementing a Numeric Huygen's Source Scheme in a Finite-Difference Program to Illuminate Scattering Bodies," *IEEE Transactions on Nuclear Science*, vol. 27, pp. 1829–1833, 1980.

[11] D. E. Merewether, "Transient Currents on a Body of Revolution by an Electromagnetic Pulse," *IEEE Transactions on Electromagnetic Compatibility*, vol. 13, pp. 41–44, 1971.

[12] A. Taflove and M. E. Brodwin, "Numerical Solution of Steady-State Electromagnetic Scattering Problems Using the Time-Dependent Maxwell's Equations," *IEEE Transactions on Microwave Theory and Techniques*, vol. 23, pp. 623–630, 1975.

[13] A. Taflove and K. Umashankar, "Radar Cross Section of General Three-Dimensional Scatterers," *IEEE Transactions on Electromagnetic Compatibility*, vol. 25, pp. 433–440, 1983.

[14] A. Taflove, K. R. Umashankar, and T. G. Jurgens, "Validation of FDTD Modeling of the Radar Cross Section of Three-Dimensional Structures Spanning Up to Nine Wavelengths," *IEEE Transactions on Antennas and Propagation*, vol. 33, pp. 662–666, 1985.

[15] C. D. Taylor, D. H. Lam, and T. H. Shumpert, "Electromagnetic Pulse Scattering in Time-Varying Inhomogeneous Media," *IEEE Transactions on Antennas and Propagation*, vol. 17, pp. 585–589, 1969.

[16] K. S. Yee, "A Subgridding Method for the Finite Difference Time Domain Algorithm to Solve Maxwell's Equations." Technical Report UCRL-96772, Lawrence Livermore National Laboratory, 1987.

[17] J. C. Kasher and K. S. Yee, "A Numerical Example of a 2-D Scattering Problem Using a Subgrid," *Applied Computational Electromagnetic Society Journal and Newsletter*, vol. 2, pp. 75–102, 1987.

[18] I. S. Kim and W. J. R. Hoefer, "A Local Mesh Refinement Algorithm for the Time Domain Finite Difference Method Using Maxwell's Curl Equations," *IEEE Transactions on Microwave Theory and Techniques*, vol. 38, pp. 821–815, 1990.

[19] J. Anderson, M. Okoniewski, and M. A. Stuchly, "Subcell Treatment of 90 Degree Metal Corners in FDTD," *Electronics Letters*, vol. 31, pp. 2159–2160, 1995.

[20] K. P. Esselle, M. Okoniewski, and M. A. Stuchly, "Analysis of Sharp Metal Edges at 45 Degrees to the FDTD Grid," *IEEE Microwave and Guided Wave Letters*, vol. 9, pp. 221–223, June 1999.

[21] R. Holland, "Finite Difference Solutions of Maxwell's Equations in Generalized Non-Orthogonal Coordinates," *IEEE Transactions on Nuclear Science*, vol. 30, pp. 4589–4591, 1983.

[22] D. H. Schaubert, D. R. Wilton, and A. W. Glisson, "A Tetrahedral Modeling Method for Electromagnetic Scattering by Arbitrarily Shaped Inhomogeneous Dielectric Bodies," *IEEE Transactions on Antennas and Propagation*, vol. 32, pp. 77–85, 1984.

[23] D. E. Livesay and K. M. Chen, "Electromagnetic Fields Induced Inside Arbitrarily Shaped Biological Bodies," *IEEE Transactions on Micorwave Theory and Techniques*, vol. 22, pp. 1273–1280, 1974.

[24] D. M. Sullivan, O. P. Gandhi, and A. Taflove, "Use of the Finite-Difference Time-Domain Method in Caculating EM Absorption in Man Models," *IEEE Transacations on Biomedical Engineering*, vol. 35, pp. 179–186, 1988.

[25] M. J. Piket-May, A. Taflove, W. C. Lin, D. S. Katz, V. Sathiaseelan, and B. B. Mittal, "Initial Results for Automated Computational Modeling of Patient-Specific Electromagnetic Hyperthermia," *IEEE Transactions on Bioemedical Engineering*, vol. 39, pp. 226–237, 1992.

[26] J.-Y. Chen and O. P. Gandhi, "Numerical Simulation of Annular Phased Arrays of Dipoles for Hyperthermia of Deep-Seated Tumors," *IEEE Transactions on Biomedical Engineering*, vol. 39, pp. 209–216, 1992.

[27] P. C. Cherry and M. F. Iskander, "FDTD Analysis of Power Deposition Patterns of an

Array of Interstitial Antennas for Use in Microwave Hyperthermia," *IEEE Transactions on Microwave Theory and Techniques*, vol. 40, pp. 1692–1700, 1992.

[28] B. J. James and D. M. Sullivan, "Creation of Three-Dimensional Patient Models for Hyperthermia Treatment Planning," *IEEE Transactions on Biomedical Engineering*, vol. 39, pp. 238–242, 1992.

[29] R. W. Lau, R. J. Sheppard, G. Howard, and N. M. Bleehen, "The Modeling of Biological Systems in Three Dimensions Using the Time-Domain Finite-Difference Method: I. The Implementation of the Model; II. The Application and Experimental Evaluation of the Method in Hyperthermia Applicator Design," *Physics in Medicine and Biology*, vol. 31, pp. 1247–1266, 1986.

[30] D. M. Sullivan, D. T. Borup, and O. P. Gandhi, "Use of the Finite-Difference Time-Domain Method in Calculating EM Absorption in Human Tissues," *IEEE Transactions on Biomedical Engineering*, vol. 34, pp. 148–157, 1987.

[31] D. M. Sullivan, "Three-Dimensional Computer Simulation in Deep Regional Hyperthermia Using the Finite-Difference Time-Domain Method," *IEEE Transactions on Microwave Theory and Techniques*, vol. 38, pp. 204–211, 1990.

[32] C.-Q. Wang and O. P. Gandhi, "Numerical Simulation of Annular Phased Arrays for Anatomically Based Models Using the FD-TD Method," *IEEE Transactions on Microwave Theory and Techniques*, vol. 37, pp. 118–126, 1989.

[33] J.-Y. Chen and O. P. Gandhi, "Currents Induced in an Anatomically Based Model of

a Human for Exposure to Vertically Polarized Electromagnetic Pulses," *IEEE Transactions on Microwave Theory and Techniques*, vol. 39, pp. 31–39, January 1991.

[34] P. J. Dimbylow and O. P. Gandhi, "Finite-Difference Time-Domain Calculations of SAR in a Realistic Heterogeneous Model of the Head for Plane-Wave Exposure from 600 MHz to 3 GHz," *Physics in Medicine and Biology*, vol. 36, pp. 1075–1089, 1991.

[35] H. O. Ruoss and F. M. Lanstofer, "Slot Antenna for Hand Held Mobile Telephones Showing Significant Reduced Interaction With the Human Body," *Electronic Letters*, vol. 32, pp. 513–514, March 1996.

[36] J. Toftgrad, S. Hornsleth, and J. B. Andersen, "Effects on Portable Antennas of the Presence of a Person," *IEEE Transactions on Antennas and Propagation*, vol. AP-41, pp. 739–746, 1993.

[37] M. A. Jensen and Y. Rahmat-Samii, "EM Interaction of Handset Antennas and Human in Personal Communications," *Proceedings of the IEEE*, vol. 83, no. 1, pp. 7–17, 1995.

[38] J. S. Colburn and Y. Rahmat-Samii, "Human Proximity Effects on Circularly Polarized Handset Antennas in Personal Satellite Communications," *IEEE Transactions on Antennas and Propagation*, vol. 46, pp. 813–820, July 1998.

[39] M. Okoniewski and M. A. Stuchly, "A Study of the Handset Antenna and Human Body Interaction," *IEEE Transactions on Microwave Theory and Techniques*, vol. 44, pp. 1855–1864, October 1996.

[40] S.-I. Watanabe, M. Taki, T. Nojima, and O. Fujiwara, "Characteristics of the SAR Distributions in a Head Exposed to Electromagnetic Fields Radiated by a Hand-Held

Portable Radio," *IEEE Transactions on Microwave Theory and Techniques*, vol. 44, pp. 1874–1883, October 1996.

[41] A. D. Tinniswood, C. M. Furse, and O. P. Gandhi, "Computations of SAR Distributions for Two Anatomical Based Models of the Human Head Using CAD Files of Commercial Telephones and the Parallelised FDTD Code," *IEEE Transactions on Antennas and Propagation*, vol. 46, pp. 828–833, 1998.

[42] O. P. Gandhi and J. Y. Chen, "Numerical Dosimetry at Power-Line Frequencies Using Anatomically Based Models," *Bioelectromagnetics Supplement*, vol. 1, pp. 43–60, 1992.

[43] J. D. Moerloose, T. Dawson, and M. Stuchly, "Application of the Finite Difference Time Domain Algorithm to Quasi-Static Field Analyis," *Radio Science*, vol. 2, pp. 329–342, 1997.

[44] A. Taflove and K. Umashankar, "A Hybrid Moment Method/Finite-Difference Time-Domain Approach to Electromangetic Coupling and Aperture Penetration Into Complex Geometries," *IEEE Transactions on Antennas and Propagation*, vol. 30, pp. 617–627, 1982.

[45] A. R. Bretones, R. Mittra, and R. G. Martin, "Hybrid NEC/FDTD Approach for Analysing Electrically Short Thin-Wire Antennas Located in Proximity of Inhomgeneous Scatterers," *Electronics Letters*, vol. 35, pp. 1594–1596, September 1999.

[46] A. R. Bretones, R. Mittra, and R. G. Martin, "A Hybrid Technique Combining the Method of Moments in the Time Domain and FDTD," *IEEE Microwave and Guided Wave Letters*, vol. 8, pp. 281–283, August 1998.

[47] G. Cerri, R. D. Leo, V. M. Primiani, P. Russo, and G. Tribellini, "Development of a Hybrid MOMTD/FDTD Technique for EMC Problems: Analysis of the Coupling Between ESD Transient Fields and Slotted Enclosures," *International Journal of Numerical Modelling Techniques: Electronic Networks, Devices and Fields*, vol. 12, pp. 245–255, 1999.

[48] R. A. Abd-Alhameed, P. S. Excell, J. A. Vaul, and M. A. Mangoud, "Hybrid Treatment for Electromagnetic Field Computation in Multiple Regions," *Electronics Letters*, vol. 34, pp. 1925–1926, October 1998.

[49] A. C. Cangellaris, M. Gribbons, and G. Sohos, "A Hybrid Spectral/FDTD Method for the Electromagnetic Analysis of Guided Waves in Periodic Structures," *IEEE Microwave and Guided Wave Letters*, vol. 3, pp. 375–377, 1993.

[50] R. Lee and T. T. Chia, "Analysis of Electromagnetic Scattering From a Cavity With a Complex Termination by Means of a Hybrid-Ray FDTD Method," *IEEE Transactions on Antennas and Propagation*, vol. 41, pp. 1560–1569, 1993.

[51] F. L. Bolzer, R. Gillard, J. Citerne, V. F. Hanna, and M. F. Wong, "A Time-Domain Hybrid Method Combining the Finite-Difference and Physical-Optics Methods," *Microwave and Optical Technology Letters*, vol. 21, pp. 82–88, April 1999.

[52] H. Rogier, F. Olysager, and D. D. Zutter, "A New Hybrid FDTD-BIE Approach to Model Electromagnetic Scattering Problems," *IEEE Microwave and Guided Wave Letters*, vol. 8, pp. 138–140, March 1998.

[53] M. Martinez-Burdalo, L. Nonidez, A. Martin, and R. Villar, "Using a Combination of

FDTD with a Surface Integration Method for Electromagnetic Scattering Analysis in Large Regions," *Microwave and Optical Technology Letters*, vol. 22, pp. 74–78, July 1999.

[54] B. S. Randhawa, A. C. Marvin, and A. D. Papatsoris, "Hybrid Uniform Theory of Diffraction Finite-Difference Time-Domain Method for Scattered Waves," *Electronics Letters*, vol. 35, pp. 459–460, March 1999.

[55] J. M. Johnson and Y. Rahmat-Samii, "MR/FDTD: A Multiple Region Finite Difference Time Domain Method," *Microwave and Optical Technology Letters*, vol. 14, pp. 101–105, February 1997.

[56] P. H. Aoyagi, J.-F. Lee, and R. Mittra, "A Hybrid Yee Algorithm/Scalar-Wave Equation Approach," *IEEE Transactions on Microwave Theory and Techniques*, vol. 41, pp. 1593–1600, September 1993.

[57] M. Okoniewski, "Vector Wave Equation 2-D FDTD Method for Guided Wave Problems," *IEEE Microwave and Guided Wave Letters*, vol. 3, pp. 307–309, September 1993.

[58] M. Mrozowski, "Function Expansion Algorithms for the Time-Domain Analysis of Shielded Structures Supporting Electromagnetic Waves," *International Journal of Numerical Modelling: Electronic Networks, Devices and Fields*, vol. 7, pp. 77–84, 1994.

[59] M. Mrozowski, "Eigenfunction Expansion Techniques in the Numerical Analysis of Inhomogeneously Loaded Waveguides and Resonators," *Elektronika (Polish)*, vol. 81, no. 512, pp. 3–154, 1994.

[60] M. Mrozowski, "A Hybrid PEE-FDTD Algorithm for Acclerated Time Domain Analysis of Electromangetic Waves in Shielded Structures," *IEEE Microwave and Guided Wave Letters*, vol. 4, pp. 323–325, October 1994.

[61] F. Alimenti, P. Mezzanotte, L. Roselli, and R. Sorrentino, "Efficient Analysis of Waveguide Components by FDTD Combined with Time Domain Modal Expansion," *IEEE Microwave and Guided Wave Letters*, vol. 5, pp. 351–353, October 1995.

[62] M. Mrozowski, M. Okoniewski, and M. A. Stuchly, "Hybrid PEE-FDTD Method for Efficient Field Modelling in Cylindrical Co-Ordinates," *Electronics Letters*, vol. 32, pp. 194–195, February 1996.

[63] A. W. Rudge, K. Milne, A. D. Oliver, and P. Knight, eds., *The Handbook of Antenna Design*, vol. 1. London, UK: Peter Peregrinus Ltd., 1982.

[64] R. Holland, "THREDS: A Finite-Difference Time-Domain EMP Code in 3D Spherical Coordinates," *IEEE Transactions on Nuclear Science*, vol. NS-30, pp. 4592–4595, December 1983.

[65] I. Zubal, C. Harrell, E. Smith, Z. Rattner, G. Gindi, and P. Hoffer, "Computerized Three-Dimensional Segmented Human Anatomy," *Physics in Medicine and Biology*, vol. 21, pp. 299–302, 1994.

[66] J. Berenger, "A Perfectly Matched Layer for the Absorption of Electromagnetic Waves," *Journal of Computational Physics*, vol. 114, pp. 185–200, 1994.

[67] J. D. Moerloose and M. Stuchly, "Reflection Analysis of PML ABCs for Low-Frequency Applications," *IEEE Micowave and Guided Wave Letters*, pp. 177–179, 1996.

[68] J. Berenger, "An Effective PML for Absorption of Evanescent Waves in Waveguides," *IEEE Microwave and Guided Wave Letters*, vol. 8, pp. 188–190, 1998.

[69] S. Gedney, "An Anisotropic PML Absorbing Media for the FDTD Simulation of Fields in Lossy Anisotropic Media," *Electromagnetics*, vol. 16, pp. 399–415, 1996.

[70] T. Dawson, J. D. Moerloose, and M. Stuchly, "Hybrid Finite-Difference Method for High-Resolution Modeling of Low-Frequency Electric Induction in Humans," *Journal of Computational Physics*, vol. 136, pp. 640–653, 1997.

[71] T. Dawson and M. Stuchly, "High-Resolution Organ Dosimetry for Human Exposure to Low Frequency Magnetic Fields," *IEEE Transactions on Magnetics*, vol. 34, pp. 708–718, 1998.

[72] M. E. Potter, M. Okoniewski, and M. A. Stuchly, "Low Frequency Finite Difference Time Domain (FDTD) for Modeling of Induced Fields in Humans Close to Line Sources," *Journal of Computational Physics*, vol. 162, pp. 82–103, 2000.

[73] S. Gabriel, R. Lau, and C. Gabriel, "The Dielectric Properties of Biological Tissues: III Parametric Models for the Dielectric Spectrum of Tissues," *Physics in Medicine and Biology*, vol. 41, pp. 2271–2293, 1996.

[74] J. Slater and N. Frank, *Electromagnetism*. McGraw-Hill Book Company, Inc., 1947.

[75] J. E. Hansen, *Spherical Near-Field Antenna Measurements*. London, U.K.: Peter Peregrinus, 1988.

[76] R. F. Harrington, *Time-Harmonic Electromagnetic Fields.* McGraw-Hill Book Company, Inc., 1961.

[77] P. Morse and H. Feshbach, *Methods of Theoretical Physics*, vol. I and II. McGraw-Hill Book Company, Inc., 1953.

[78] W. H. Press, *Numerical Recipes in FORTRAN 77 and FORTRAN 90: The Art of Scientific Computing.* New York: Cambridge University Press, 1996.

[79] W. M. Boerner and F. H. Vandenberghe, "Calculation of the Electrical Radius Ka of a Spherical Scatterer from the Scattered Field," *Canadian Journal of Physics*, vol. 49, pp. 1507–1535, 1971.

[80] M. Mrozowski, "Stability Condtion for the Explicit Algorithms of Time Domain Analysis of Maxwell's Equations," *IEEE Microwave and Guided Wave Letters*, vol. 4, pp. 279–281, August 1994.

[81] A. Kreczkowski, T. Rutkowski, and M. Mrozowski, "Fast Modal ABCs in the Hybrid PEE-FDTD Analysis of Waveguide Discontinuities," *IEEE Microwave and Guided Wave Letters*, vol. 9, pp. 186–188, May 1999.

[82] M. Mrozowski, M. Niedzwiecki, and P. Suchomski, "Improved Wideband Highly Dispersive Absorbing Boundary Condition," *Electronics Letters*, vol. 32, pp. 1109–1111, June 1996.

[83] J. Bowman, T. Senior, and P. Uslenghi, eds., *Electromagnetic and Acoustic Scattering by Simple Shapes.* Amsterdam: North-Holland Publishing Company, 1969.

[84] A. Taflove, ed., *Advances in Computational Electrodynamics - The Finite-Difference Time-Domain Method.* Boston: Artech House, Inc., 1998.

[85] J. D. Moerloose and M. A. Stuchly, "Behaviour of Berenger's ABC for Evanescent Waves," *IEEE Microwave and Guided Wave Letters*, vol. 5, pp. 344–346, 1995.

[86] A. Taflove, K. R. Umashankar, B. Beker, F. Harfoush, and K. S. Yee, "Detailed FD-TD Analysis of Electromagnetic Fields Penetrating Narrow Slots and Lapped Joints in Thick Conducting Screens," *IEEE Transactions on Antennas and Propagation*, vol. 36, pp. 247–257, 1988.

[87] K. R. Umashankar, A. Taflove, and B. Beker, "Calculation and Experimental Validation of Induced Currents on Coupled Wires in an Arbirtrarily Shaped Cavity," *IEEE Transactions on Antennas and Propagation*, vol. 35, pp. 1248–1257, 1987.

[88] W. Yu and R. Mittra, "A Conformal FDTD Algorithm for Modeling Perfectly Conducting Objects with Curve-Shaped Surfaces and Edges," *Microwave and Optical Technologies Letters*, vol. 27, pp. 136–138, October 2000.

[89] W. Yu and R. Mittra, "A Conformal Finite Difference Time Domain Technique for Modeling Curved Dielectric Surfaces," *IEEE Microwave and Wireless Components Letters*, vol. 11, pp. 25–27, January 2001.

[90] K. P. Esselle, M. Okoniewski, and M. A. Stuchly, "Accurate Modeling of Field Singularities at Metal Edges Diagonal to the FDTD Grid," *Proceedings of the IEEE Antennas and Propagation Society International Symposium*, pp. 2176–2179, 1997. Montreal, Canada.

[91] T. Dawson, "Low-Frequency Induction in a Homogeneous Sphere by Line Sources I - Formulation and Line Current Excitation," *Radio Science*, vol. 35, no. 3, pp. 691–702, 2000.

[92] T. Dawson, "Low-Frequency Induction in a Homogeneous Sphere by Line Sources II - Line Charge Excitation and Discussion," *Radio Science*, vol. 35, no. 3, pp. 703–712, 2000.

[93] "Validation of computational methods for evaluation of electric fields and currents induced in humans exposed to electric and magnetic fields," Electric Power Research Institue (EPRI), Palo Alto, CA, 1998. Report TR-111768.

Appendix A

Finite-Difference Time-Domain Method

A.1 The Yee Grid

The FDTD method in electromagnetics was initiated by the seminal paper by Kane Yee over thirty years ago [1], which was an attempt to explicitly solve Maxwell's equations for initial value problems. It is a numerical time-domain technique that solves the differential form of Maxwell's equations by discretizing both time and space. Starting with initial conditions, solutions for the field values at each point in the numerical grid are iterated through time, where fields are updated at each time-step based on simple difference equations involving neighbouring field values. The difference equations are developed from the electromagnetic curl equations.

The curl equations for electromagnetics in a linear, isotropic medium are:

$$\vec{\nabla} \times \vec{H} = \vec{J} + \epsilon \frac{\partial \vec{E}}{\partial t} \tag{A.1}$$

$$\vec{\nabla} \times \vec{E} = -\vec{M} - \mu \frac{\partial \vec{H}}{\partial t} \tag{A.2}$$

Equations (A.1, A.2) are translated into explicit difference equations by approximating the differentials by central difference equations. An example of a central difference equation in one dimension for the first derivative of a function f is given in (A.3), where Δx is the grid resolution or discretization step in that dimension. The advantage of central differences is that they are second order accurate. By separation of variables in rectangular coordinates, equations (A.1, A.2) produce a set of six scalar difference equations, in which field values at each point in time and space are related only to neighbouring points. The advantage of this formulation is that evaluation of large matrices is avoided, but field values must be calculated at each node.

$$\frac{\partial f(x)}{\partial x} \approx \frac{f(x + \Delta x) - f(x - \Delta x)}{2\Delta x} \tag{A.3}$$

One of the innovations provided by Yee was that he staggered the positions of co-indexed electric and magnetic fields by half a grid cell in both time and space (see Figure A.1). Material parameters are maintained in separate media files for computation, and are assigned to each node individually. This offers many advantages [2], namely:

- the grid simultaneously satisfies the differential and integral form of Maxwell's equations;
- the continuity of tangential fields is maintained at an interface of dissimilar materials.

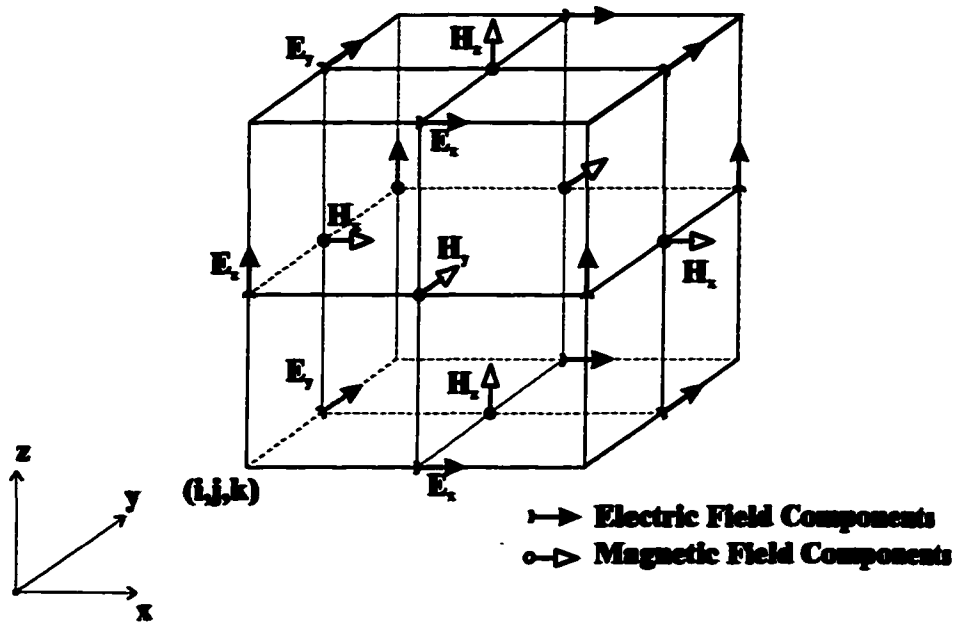

Figure A.1: The Yee cell in the FDTD method.

This yields a "stair-cased" approximation to materials (further discussion of this issue is given in section A.5);

- the location of the field components ensures that the scheme is divergence free in a source-free space; and
- by staggering electric and magnetic fields in time, the FDTD method becomes fully explicit, with no necessity to solve simultaneous equations or perform matrix inversions.

As a matter of notation, from henceforth a specific node location in a grid is referred to by its index number. Thus, in a uniform rectangular lattice a space point is denoted by $(i, j, k) = (i\Delta x, j\Delta y, k\Delta z)$, where Δx, Δy, and Δz are the lattice space

increments in the x, y, and z directions, and i, j, and k are integers. Likewise, the commonly used index for time is n. Furthermore, any function f of space and time evaluated at a particular point on the grid is $f(i\Delta x, j\Delta y, k\Delta z, n\Delta t) = f^n_{i,j,k}$, where Δt is the time interval between updating field components. These indices should not be confused with complex number notations, the wave number, or the mode number unless specified, but their meaning should be obvious from the context.

A.2 Stability

The finite-difference system developed from the approximation of Maxwell's equations allows for the specification of the time step Δt, and the spatial increment in each dimension. In the standard rectangular Yee grid, the spatial grid increments Δx, Δy, and Δz can be arbitrarily selected, but due to the nature of the finite-difference system, there is a constraint imposed which takes the form of a relation between the time and space increments. In Chapter 4 of [2], Fourier modes are used to demonstrate that the stability constraint in the Yee grid given by Courant criterion is (A.4).

When $\Delta x = \Delta y = \Delta z = \Delta$, then (A.4) reduces to $\Delta t \leq \frac{\Delta}{c\sqrt{3}}$, with c representing the wave phase velocity in the medium.

$$\Delta t \leq \frac{1}{c\sqrt{\frac{1}{(\Delta x)^2} + \frac{1}{(\Delta y)^2} + \frac{1}{(\Delta z)^2}}} \tag{A.4}$$

A.3 Boundary Conditions

Many of the problems of interest that are investigated with the FDTD method involve geometries defined in "open" regions. This terminology means that the spatial

domain in one or more coordinate directions is unbounded (i.e. extends to infinity - representing a radiation problem). Virtually all scattering problems are in this category, as are antenna measurement performance evaluation e.g. antenna pattern determination. Since no computer can store unlimited data, there must be a way of constructing a boundary condition in the model that allows for termination of the computational domain.

Such a boundary condition must simulate the extension of the "open" dimension to infinity, and therefore must permit outward propagating numerical waves to exit the computational domain. In the process, it must suppress numerical reflections of the wave back into the domain, which would represent non-physical waves that could interfere with the solution. These boundary conditions have been called *absorbing boundary conditions* (ABC) or radiation boundary conditions. The former is used throughout the rest of this thesis. Because the FDTD method utilizes a central difference scheme, ABCs cannot be developed directly from the numerical algorithms. Knowledge is required of fields one-half cell to each side of a particular node, and cells on the outermost boundary have no outer neighbour points. As a result, ABCs are based on two general approaches to simulate the open problem: a differential-based approach, or an approach employing a material absorber.

Differential-based ABCs seek to "annihilate" outgoing waves by creating a differential operator which effectively only allows wave propagation in one direction. The differential operator is approximated as a difference operator, and in theory any order of accuracy can be obtained by better and better approximations to the differential. In practice, stability limits the accuracy that can be obtained [84].

A.3.1 Material Absorbers

Material absorbers have been an avenue of intense research since the development of the perfectly matched layer (PML) by Berenger in 1994 [66]. In essence, the computational domain is surrounded by a layer of lossy material that dampens outgoing fields. Berenger provided a "split-field" approach in the lossy material region that allowed substantial absorption without affecting the numerical phase velocity. As a result, Berenger's method produced $30dB$ greater attenuation than any other existing method at that time. The impact of this technique was staggering because it allowed modeling that coincides with the greater than $70dB$ dynamic range available in anechoic chambers. The material absorber approach, and in particular the Berenger's PML, has been the method of choice for many years. This is because of the greater absorption that can be attained with the PML over differential-based methods.

PML absorbers consist of several layers of the absorbing medium at one or more outer boundaries in the computational domain. The absorption of waves is controlled by the conductivity that is assigned to each layer of the absorber. In fact, it is the conductivity *profile* (i.e. the way the conductivity changes from layer to layer) that provides the perfectly matching boundary condition the ability to simulate the transmission of outgoing waves. In the discretized model, a perfect match is unattainable; nevertheless, excellent absorption can be achieved. A PML in the FDTD method is specified by three parameters as in equation (A.5). *Layers* specifies the number of layers in the full PML in that direction; *level* specifies the level of absorption at normal incidence required in dB; and *type* specifies the profile of the conductivity from layer to layer which can take on the value of a power

profile or a geometric profile.

$$PML = PML(layers, type, level) \tag{A.5}$$

For both types of profiles, a parameter p specifies the rule to be followed in determining the conductivity of each layer. For the power profile the rule is $\sigma = z^p$, and for the geometric profile the rule is $\sigma = p^z$, where σ is the conductivity and z is the layer number.

One of the limitations of PMLs is that their performance is not acceptable in low frequency regions. De Moerloose and Stuchly [67, 85] showed that reflectivity levels in the low frequency (evanescent) regions can be high, but due to a retardation effect in the PML layers the reflected signal does not manifest itself until later in the simulation. This suggested that judicious choice of the PML parameters allows the user to set a long retardation time, thereby permitting a problem simulation to be performed and recorded before reflections can interfere with a solution. It is shown that the best profile for this condition is to utilize an exponential profile of the form $\sigma = e^{z/A}$ where A is related to the parameter p. The retardation times then become dependent only on frequency. In practice, a given problem demands specific PML parameters and empirical studies must be performed to optimize modeling, but the analysis in [67] provides a starting point.

A.3.2 Annihilator Type

The discretized Maxwell's equations utilized in the FDTD method involve the curl operator relating spatial derivatives to nearest neighbour field differences. However, at the edge of the computational domain there is no knowledge of the field components beyond the boundary and another method must be developed to find the spatial partial derivative

transverse to the wave direction.

Bayliss-Turkel

As outlined in [2], radiating solutions of the wave equation in spherical coordinates can be expressed as a convergent series:

$$\begin{aligned} U(r,\theta,\varphi,t) &= \sum_{i=1}^{\infty} \frac{u_i(ct-r,\theta,\varphi)}{r^i} \\ &= \frac{u_1(ct-r,\theta,\varphi)}{r} + \frac{u_2(ct-r,\theta,\varphi)}{r^2} + \ldots \end{aligned} \tag{A.6}$$

where the leading terms dominate far from the origin. Forming the partial differential operator,

$$L \equiv \frac{1}{c}\frac{\partial}{\partial t} + \frac{\partial}{\partial r} \tag{A.7}$$

and applying it to (A.6) gives an asymptotic expression for large r:

$$LU = \frac{-u_1}{r^2} + \frac{-2u_2}{r^3} = O(r^{-2}) \tag{A.8}$$

In this respect, L is the Sommerfeld radiation condition. Solving for the required radial derivative gives

$$\frac{\partial U}{\partial r} = -\frac{1}{c}\frac{\partial U}{\partial t} + O(r^{-2}) \tag{A.9}$$

which can in principle be used to terminate the domain.

Bayliss and Turkel showed that a slightly augmented version of the radiation operator $B_1 = L + \frac{1}{r}$ gives annihilation of order $O(r^{-3})$, i.e. it diminishes faster to zero. To seek even better performance, an operator of order n can be formed that annihilates the

first n terms in (A.6). This is formed by successive application of Bayliss-Turkel operators as

$$\begin{aligned} B_n &= \prod_{k=1}^{n}\left(L+\frac{2k-1}{r}\right) \\ &= \left(L+\frac{2k-1}{r}\right)\ldots\left(L+\frac{3}{r}\right)\left(L+\frac{1}{r}\right) \end{aligned}$$

In practice, the complexity of the operator increases significantly with higher order. In the literature, B_2 has been used as a good compromise between complexity and effectiveness, with reflection coefficients on the order of 1% being obtained.

Another way of constructing the radial derivative operator was introduced by Enquist and Majda through *one-way wave equations* (summarized in [2]). The wave equation is factored into two, one-way partial derivative operators. This approach is detailed in Appendix D in more detail.

A.4 Quasi-Static FDTD

Quasi-static approximations can be applied when the dimensions of the object of study are a fraction of a wavelength. Since using the quasi-static approximation implies that the electric and magnetic fields become decoupled, it is possible to study their effects in isolation. If one were to attempt to study extremely low frequency problems using the standard FDTD formulation, simulation times of the order of a few periods of the source would have to be used to reach steady-state. For instance, for a problem at 60 Hz, with spatial discretizaton of $\Delta x = \Delta y = \Delta z = 0.5\,\text{cm}$, from the Courant stability criterion (A.4), the duration of one timestep would be $\Delta t = \frac{\Delta x}{\sqrt{3}c} = 9.6\,\text{ps}$. Allowing for 4 periods of

the source field, the number of timesteps required for the simulation would be $N_{\Delta t} = 7 \times 10^9$. Even on a fast computer, the simulation would run for over *one hundred years*. For some simulations frequency scaling is used, but this approach has limitations - among them is that the fields are not decoupled. However, quasi-static approximations can be used to advantage in certain situations with the FDTD method, and thus the prohibitively long simulation time constraint is removed.

The quasi-static FDTD method, as introduced in [43], is only briefly summarized here. The standard FDTD algorithm can be used to advantage with certain objects, since the phase relationships of fields in good conductors and dielectrics is known. Because conduction currents dominate displacement currents in conductors, and the opposite is true in dielectrics, the steady-state behaviour of fields can be predicted beforehand. Fields external to a conductor have the same phase as an incident field, whereas interior fields are first order in the quasi-static approximation and are therefore proportional to the time derivative of the incident field. By using a ramp function (which can be interpreted as an approximation to the start of a sinusoid), all fields in steady state attain either a linear (in good dielectrics) or constant (in conductors) time behaviour after a short simulation time (a fraction of a period of the approximated sinusoid). To obtain a solution, it is therefore sufficient to obtain field values at two time steps after the transient response has decayed.

To reduce high-frequency contamination in simulations, a smoothed ramp function

is used for the incident electric field E_{inc}:

$$E_{inc} = \begin{cases} 0 & -\infty < t \leq t_0 \\ \cosh(t) - 1 & t_0 < t \leq \tau \\ A \cdot (t - \tau) + h & t > \tau \end{cases} \tag{A.10}$$

where t is the time increment, t_0 is the starting point of the ramp (usually zero), and A is the desired slope of the ramp which is related to the peak amplitude and frequency of the sinusoid that is approximated. The constants τ and h are dependent on simulation parameters such as the grid and time discretization, and serve to preserve continuity between the three sections of the ramp function.

In a standard FDTD program, the use of a single plane wave necessarily implies the fields are coupled. Quasi-static exposure can still be accomplished by creating a standing wave within the FDTD domain. This is achieved by exciting two plane waves in opposite directions using the total/scattered field formulation. By controlling the phase and amplitude, exposure either to only electric or magnetic field can be created within a limited volume with dimensions much smaller than the wavelength.

In summary, the quasi-static FDTD method may be used when:

i) in the object of study either the conduction or displacement current dominates the other; and

ii) the size of the object is much smaller than the incident field wavelength.

When these conditions are satisfied, electric or magnetic field exposure can be studied in isolation by creating an appropriate standing wave condition, and by utilizing a ramp excitation function.

From Maxwell's equations in the quasi-static limit it can be demonstrated that the time to steady state for electric or magnetic exposure is governed by relaxation or diffusion equations respectively. For each, there is a characteristic time constant which governs the transient response, or conversely marks the transition to steady-state. These time constants are $\tau_{relaxation} = \frac{\epsilon}{\sigma}$ and $\tau_{diffusion} = \mu\sigma l^2$, where ϵ is the dielectric constant, σ is the conductivity, μ is the permeability, and l is the largest characteristic dimension of the object (i.e. diameter for a sphere). This in turn indicates when steady-state is reached, and when the simulation can be halted.

Although the exposure processes are governed by either relaxation or diffusion in real life, in the FDTD approach the coupling of the magnetic and electric fields can not be separated to perfectly simulate a quasi-static situation. This can be accomplished indirectly by creating a standing wave, but both field vectors are still excited. For the case of a lossy object with conductivity, but relative permittivity and permeability of one, the diffusion time constant dominates. Consequently, for both types of FDTD simulations (standing wave created for magnetic or electric exposure) the time to reach steady-state is governed by the diffusion constant.

A.5 Material Modeling

One of the main advantages of the FDTD method over other methods is its ability to handle large and complex heterogeneous structures. Material properties are assigned values at each node directly analogous to the system being modeled. In other words, a discretized version of the modeled object must be constructed and material properties

must be known beforehand. A good example of this is the human body, where the body model consists of many different tissue and organ types, each having been classified with permittivity, permeability, and conductivity values over a wide range of frequencies.

Due to the discretized nature of the method, it is necessary to discuss the numerical implications of this quantization. For instance, materials with continuously varying property values in one or several directions take on a quantized nature in modeling. What effect this has on the solution must be quantified and guidelines of validity established. A brief examination is given of the existing methodology as it exists in the most general FDTD algorithm, the approximations this introduces, and the problems to validity that can be manifested. The discussion continues with methods to efficiently compensate for these apparent problems.

A.5.1 Staircasing Approximation

In the FDTD algorithm, the update of a particular field value depends in part on neighbouring field values and neighbouring material properties. Since the modeled structure is discretized, this implies that the transition from one material region to another is abrupt (or quantized). Also, a smoothly varying contour can not be perfectly represented unless an infinitely small grid resolution is assumed. The result is that the modeled structure is approximated by one that is *staircased* depending on the grid scheme used (e.g. rectangular, cylindrical, etc.).

Consider the case of a rectangular grid with equal discretization in each direction $\Delta = \Delta x = \Delta y = \Delta z$. The result of quantizing the structure into discrete material regions is to construct a "building block" model of small cubes (or *voxels* - the three dimensional

analogue of pixels) of one material type or another. The cubes are stacked together as appropriate, and an overall model of the structure is created. Even for a non-uniform grid scheme, one can visualize the block-shaped nature of the computational model.

Some of the problems associated with this approximation have been mentioned above: smooth contours can not be perfectly represented, and the discretization provides abrupt material parameter changes at boundaries. One other problem is the representation of fine features. For instance, for a narrow slot a very fine grid resolution is necessary to accurately represent the slot. The drawback of this is the enormous increase in the number of nodes; modeling can quickly become unfeasible in this case due to limited computer resources.

As expected, there has been a large research investiture in attempting to mitigate the errors introduced by the staircasing approximation. Several methods have been proposed to overcome these problems. There are basically two ways to overcome the difficulties: adopting a different grid methodology *globally* that better conforms to the structure at hand, or *locally* modifying the algorithm near identified areas of complication. Schemes that fit in the former include conformal grid techniques, where update equations are found by expressing fields in terms of covariant and contravariant components, where the grid is actually flexible and conforms to the structure modeled e.g.[21]. This method involves a fundamental change in the FDTD algorithm that is not relevant to this discussion.

Methods that alter local algorithms for fine features include the contour path (CP) technique [86, 87, 88, 89], sub-gridding [16, 17, 18], and subcellular techniques [19, 90]. The CP-FDTD technique looks at the integral form of the curl equations applied to the

immediate neighbouring points surrounding a particular field location (effectively a closed, square contour surrounding a field location). When a structure edge passes through such a contour, the path integral is altered by whatever material is on either side of the edge. The CP-FDTD method identifies such nodes (and their respective contours), and modifies the local update equations according to the integral form.

Sub-gridding applies fine meshing of the grid where the modeled structure demands, and a coarser grid in regions of uniform material properties. For example, a large plate with one small slot is modeled with a coarse grid over the entire domain, excepting the area of the slot where the grid is refined. The advantage of this techniques is that computer resource requirements are increased only where they are needed, and not across the entire domain. In implementation, some of the drawbacks are that the stability of the method can be adversely affected, and that errors can be introduced at the transition from one grid size to another.

Subcellular techniques are an attempt to trade off the benefits of drawbacks of the previous two. In essence, a more accurate depiction of boundaries between materials is established by influencing the value of material parameters on either side of the boundary. Since this can be done in pre-processing and the grid size is not actually changed, there is not a substantial increase in the computer resources required. The concept of subcellular averaging arises from the integral expression of Ampere's law (A.11) and Faraday's law

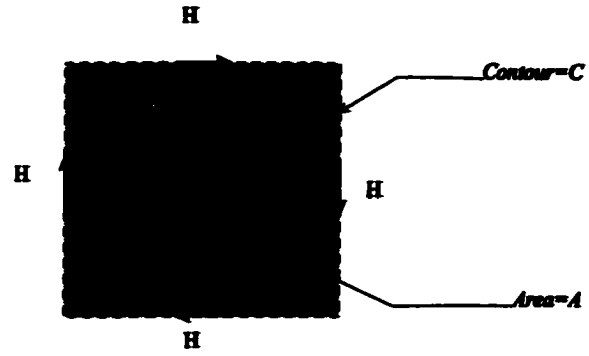

Figure A.2: Offset grid contour surrounding a particular electric field point.

(A.12).

$$\iint_A \frac{d}{dt}\left(\epsilon\vec{E}\right) = \oint_C \vec{H}\cdot\vec{dl} \tag{A.11}$$

$$\iint_A \frac{d}{dt}\left(\mu\vec{H}\right) = -\oint_C \vec{E}\cdot\vec{dl} \tag{A.12}$$

Considering (A.11) and the Yee grid in two dimensions for a given electric field component (Figure A.2), the contour C can be imagined as following an offset grid from the original grid which lies parallel with all electric field vectors. Now assuming that the electric field is constant across the area A, equation (A.13) shows that the dielectric parameter ϵ can still vary across A. But what value should ϵ take on? Sub-cell averaging answers this question by determining an *effective* dielectric constant ϵ_{eff}.

$$\iint_A \frac{d}{dt}\left(\epsilon\vec{E}\right)dA = \frac{d\vec{E}}{dt}\iint_A \epsilon dA \tag{A.13}$$

To demonstrate sub-cell modeling, the regular FDTD grid is considered and the area of interest for averaging is illustrated in Figure A.3. In this case, the standard grid is

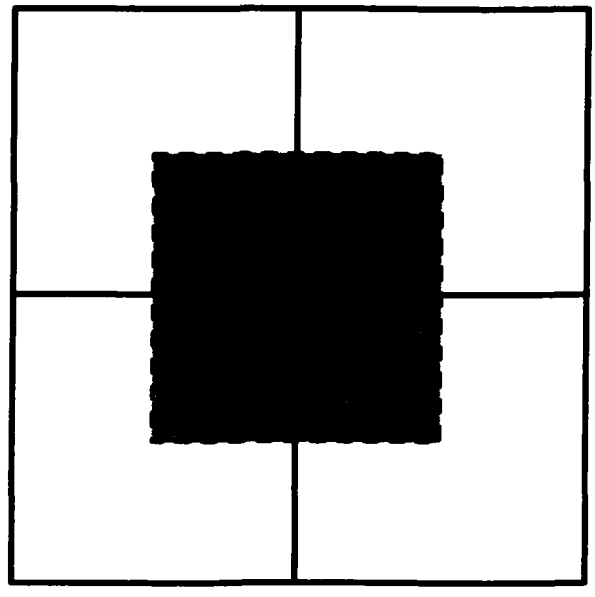

Figure A.3: Offset grid superimposed on regular FDTD grid.

represented by solid lines, and the shaded area is the region of interest corresponding to A from above. If the standard grid is considered coincident with the page, then the electric field at the centre of A actually hovers half a grid cell above the page. Allowing A (and indeed the rest of the structure) to be filled with a heterogeneous mix of dielectrics, the effective dielectric constant ϵ_{eff} for the node at the centre of A is determined as a weighted sum of the dielectric constants $\epsilon_1, \epsilon_2, \epsilon_3, ..., \epsilon_n$ within A. The weights are determined by the percentage of the area that ϵ_i fills in A.

The determination of the weighted sum depends on the level of accuracy desired in the sub-cell averaging. The accuracy level is set by an integer index N which is directly correlated to the subdivisions of the contour C and the area A. Examples for $N = 1, 2$ are demonstrated in Figure A.4. The probe points (large dots) represent the physical location

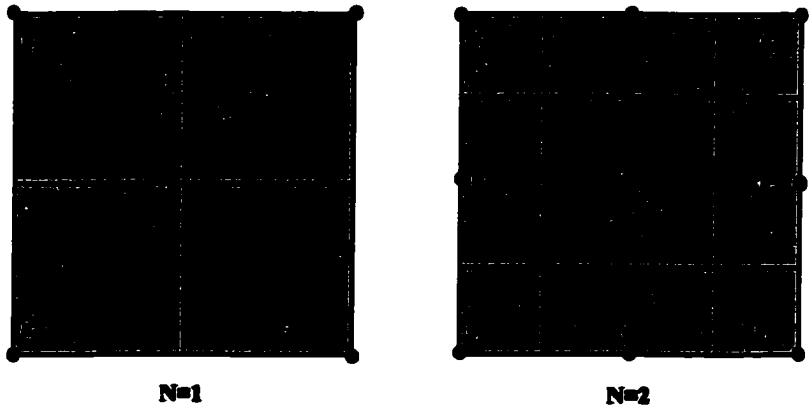

Figure A.4: Graphical representation of subcell averaging for $N = 1$ and $N = 2$ subdivisions. Note the positions of the probing points, and the percentage of A that each corresponds to.

from where the material values are taken. The weight assigned to each probe point depends on the percentage area of A that their corresponding sub-cell occupies. For the $N = 1$ case then, the effective material parameter is

$$\epsilon_{eff} = \frac{\epsilon_1 + \epsilon_2 + \epsilon_3 + \epsilon_4}{4}$$

and for the $N = 2$ case the material parameter is

$$\epsilon_{eff} = \frac{\frac{\epsilon_1+\epsilon_3+\epsilon_5+\epsilon_7}{4} + \frac{\epsilon_2+\epsilon_4+\epsilon_6+\epsilon_8}{2} + \epsilon_9}{4 \cdot (\frac{1}{4}) + 4 \cdot (\frac{1}{2}) + 1}$$

Note that this procedure is valid for each of the material parameters: conductivity, permittivity, and permeability.

Appendix B

Verification of the Line-Source Method in FDTD

The method described in Chapter 4 is verified in three ways. First, a line-source is modeled in free space where it is known that resultant fields should follow a $\frac{1}{r}$ behaviour (r is the distance from the line-source to the point of observation). Recollecting that the motivation for this work is to investigate electric fields induced in humans at powerline frequencies by a line-source, it is helpful to study a simple object for which the problem has an analytic solution, e.g. a lossy sphere of a size comparable to the human body. The material parameters of the sphere are chosen to represent nominal values in the human body. In order to validate the FDTD method at low frequencies for the line-source, both the electric field and magnetic field exposures are investigated. Comparisons are made based on average, root-mean-square (RMS), and maximum induced electric fields in the sphere. The closed form solutions for fields induced in a homogeneous lossy sphere by an

infinite current line (magnetic field) and an infinite line of charge (electric field) are reported in [91, 92]. The relative and absolute errors are also investigated to establish validity of the method, and to identify locations of large errors.

B.1 Results of Method Verification

B.1.1 Free Space

First the cylindrical TEM line-source implementation was validated by exciting an empty computational domain (free space) with the infinite line-source function. To model this situation, a domain of $20\,\text{cm} \times 110\,\text{cm} \times 110\,\text{cm}$ was utilized, with a grid resolution of $1\,\text{cm}$ in each direction, and the timestep is chosen to satisfy the Courant stability condition. The line-source was oriented in the x-direction, centered $50\,\text{cm}$ over the domain, i.e. $(yh, zh) = (55\,\text{cm}, 155\,\text{cm})$. The domain was terminated by a PML (6, P, 40dB) (6 layers, with a parabolic profile, and with 40 dB attenuation for normal incidence), on all sides. The time excitation was the function given by equation (A.10). The simulation was run for 200 timesteps to allow for the wave to traverse fully the domain. The fields at the last timestep $N_{\Delta t} = 200$ were then compared with the analytic solution. As shown in Table B.1, the resultant fields are in excellent agreement globally with the analytic results. As expected, the Cartesian mesh representation of cylindrical fields introduces longitudinal fields that are non-physical, but they are negligibly small, i.e. of the same order of magnitude as the error fields in the transverse directions.

Table B.1: Relative Errors in Electric Field for the Empty Domain

	Maximum		Average	
Grid Resolution	Horizontal (y)	Vertical (z)	Horizontal (y)	Vertical (z)
Coarse (2 cm)	0.0910 %	0.0188 %	0.0078 %	0.0022 %
Fine (1 cm)	0.0114 %	0.0036 %	0.0018 %	0.0005 %

B.1.2 Lossy Sphere

For both electric and magnetic exposure for a lossy sphere the problem simulation was formulated as follows. A conductive sphere of similar size and conductivity to those of the human body (conductivity = 0.1 S/m, radius = 50 cm) was selected. With these parameters, at low frequencies, the conduction current is much greater than the displacement current, and so quasi-static approximations apply. The staircased sphere was centered in a computational domain of size 110 cm ×110 cm ×110 cm, terminated on all sides by a PML (9, P, 60 dB). From previous research [93], large errors are expected at the surface of the staircased sphere. Their magnitude depends on the shape of the staircasing and conductivity contrast. To partially mitigate these effects, sub-cell averaging of material parameters is used in the modeling.

As previously, a standing wave was created for a magnetic or electric field excitation with two waves of proper orientations traveling from the opposite directions on a line-source. The line was assumed oriented in the x-direction, centered over the sphere at a distance of 50 cm. Source function parameter values were chosen to simulate a 1 A (peak) current of 60 Hz in the magnetic field case. For the electric field case, source function parameters were chosen to simulate a field of 1000 V / m at the center of the domain (1 m from the line) in the absence of the sphere; this corresponds to a line charge density of $\rho = 2000\pi\varepsilon_0$ C / m.

Simulations were performed with a grid resolution of 1 cm. Steady-state was reached after 2000 timesteps.

Figures B.1 to B.3 show the individual calculated field components at representative cross-sections in the three directions, along with the corresponding analytic solution. It is apparent that the field spatial distributions are very similar, except that in a few cases (especially the E_z and E_y fields) the numerical solution shows larger field values in some locations. These tend to obscure the visual representation of the actual field distribution. Figure B.4 shows the total field $E_{tot} = \sqrt{E_x^2 + E_y^2 + E_z^2}$ distribution throughout the sphere, which is in excellent agreement with the analytic solution. Point-by-point relative errors were examined, with the observation that the locations of high relative error are concentrated at the surface of the sphere. There are large relative errors at the very center also that are associated with zero field value in the analytic solution. A computed field there, however small, represents an infinitely large relative error.

Table B.2 provides a quantitative evaluation of the errors. The computed maximum field is much greater than the analytic maximum field. However the average field is very close to the analytic average field, as is the RMS field. Relative errors in the total fields are larger in the upper half of the sphere compared to the lower half, and range around 25-30% on average at the surface of the sphere. Relative errors in the total fields at interior points are less than 0.5% in general. The last row in the table represents the maximum error in the respective fields, computed point by point.

Combining the qualitative and quantitative results, the following observations can be made: the quasi-static FDTD method with the line-source accurately models the induced

Table B.2: Computed vs. Analytic Results for Magnetic Induction - no subcell averaging

	Maximum	Average	RMS
Computed Total Electric Field (μV / m)	37.778	11.142	12.162
Analytic Total Electric Field (μV / m)	28.502	11.138	12.154
% Difference $\left(\left\|\frac{Computed-Analytic}{Analytic}\right\| \times 100\right)$	33 %	0.03 %	0.07 %
Error Field ($\|Computed - Analytic\|$) (μV / m)	10.404	0.0811	0.377

field distribution and field values in the interior of lossy objects, but field values close to object boundaries are over-predicted by up to 33%.

The problem of large errors at the boundaries of the staircased sphere are a direct result of the abrupt transition in material properties, and the staircasing that causes enforcement of boundary conditions different from the original object. This abrupt transition can be mitigated by the use of sub-cell averaging of material properties in the pre-processing stage of a FDTD simulation. In the case of the test sphere, the effect is to create a layer at the boundary whose conductivity values range from 0 to 0.1 S/m

The same simulations as above were performed with sub-cell averaging utilized. Table B.3 provides the quantitative look at the errors with sub-cell averaging of $N = 2$ and $N = 8$. It is evident that the computed maximum field is larger than the analytic maximum field (18.7% with $N = 2$, 5.5% with $N = 8$), but less than that with no averaging. The average field is still very close to the analytic average field, as is the RMS value. The absolute and relative errors have been reduced, meaning more accurate prediction of fields point by point has been achieved. The relative errors are still larger in the upper half of the sphere compared to the lower half, but have reduced overall. For instance, on the sphere boundary the relative errors range from 15 to 25% on average.

The conclusion that can be made at this point is that simulations for magnetic

Table B.3: Computed vs. Analytic Results for Magnetic Induction with Subcell Averaging

	Maximum		Average		RMS	
Subcell Averaging	$N=2$	$N=8$	$N=2$	$N=8$	$N=2$	$N=8$
Computed Total Electric Field (μV / m)	33.824	30.079	11.196	11.233	12.215	12.253
Analytic Total Electric Field (μV / m)	28.502	28.502	11.188	11.222	12.205	12.241
% Difference $\left(\left\|\frac{Computed-Analytic}{Analytic}\right\| \times 100\right)$	18.7 %	5.5 %	0.07 %	0.1 %	0.08 %	0.1 %
Error Field ($\|Computed - Analytic\|$) (μV / m)	8.689	3.131	0.0426	0.0109	0.195	0.0650

induction using sub-cell averaging produce more accurate results and can significantly improve the determination of maximum field values with higher levels of sub-cell averaging. Field values at object boundaries are still over-predicted, but the error in these fields can be greatly reduced.

The results for electric induction in the sphere are shown qualitatively in Figures B.5 through B.7. No figure is presented for the E_x field, as the analytic solution is zero everywhere. Similar to the magnetic induction case, there are very large field values on the surface of the sphere, but in contrast the errors are greater. The field distributions are still matched to the analytic field configurations. Relative errors are still highly concentrated on the surface of the sphere.

Table B.4 provides quantitative results. The computed maximum field is much greater than the analytic maximum field. In this instance the location of maximum absolute error is actually the location of maximum relative error, and exists around the entire boundary of the topmost part of the staircased sphere. That is the location of the maximum source field as well. However, the average field is very close to the analytic average field, as is the RMS value, though it is not as well predicted as in magnetic field induction case.

These results indicate that the FDTD method is not satisfactory at predicting maximum induced fields, but is still valuable for predicting field distributions and average

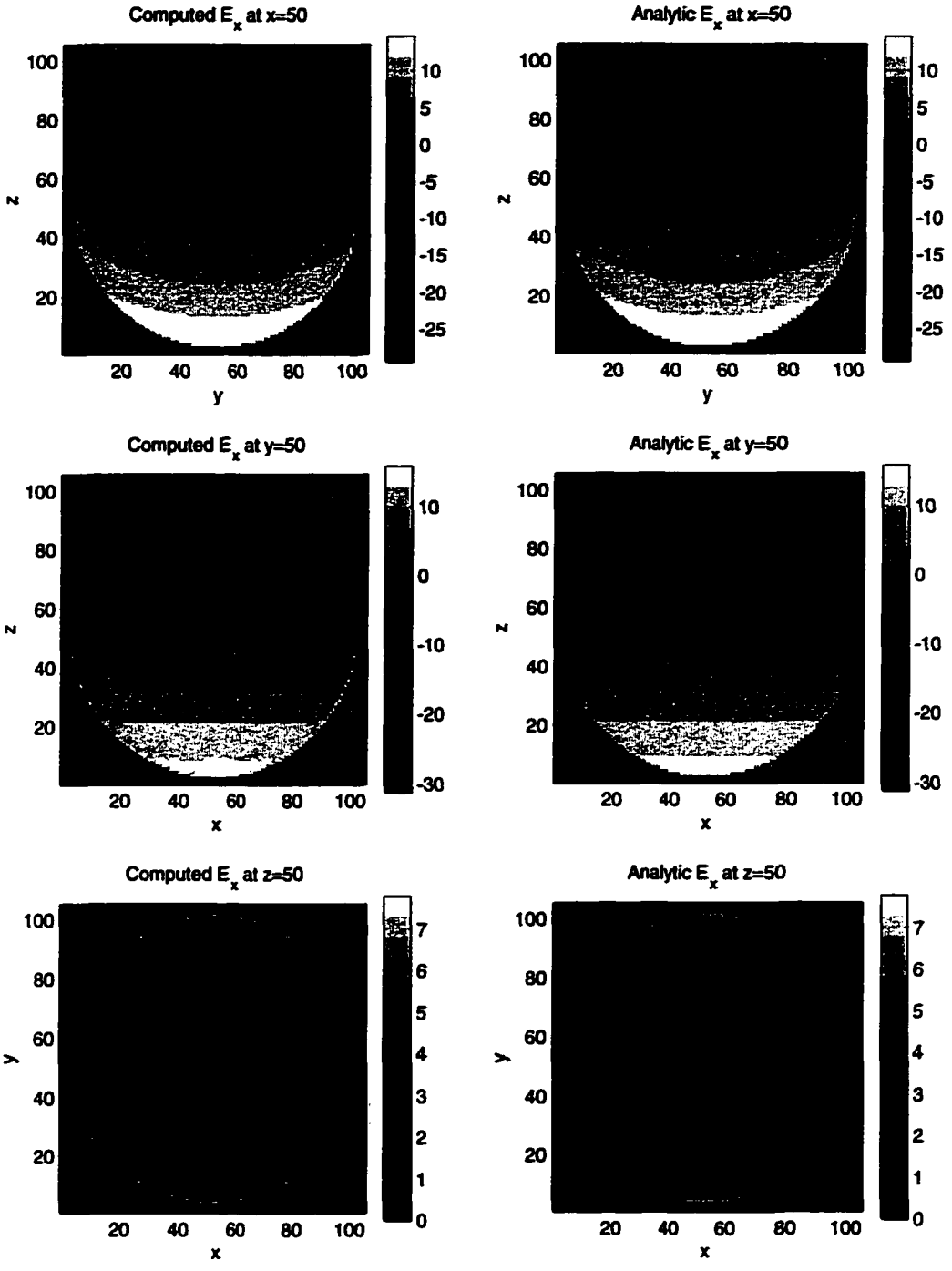

Figure B.1: Magnetic Induction in a lossy sphere from a 60 Hz line-source (1000 V/m at $r = 1$ m) - Induced E_x-field (in μV/m) for cross-sections in the three principal planes (computed vs. analytic).

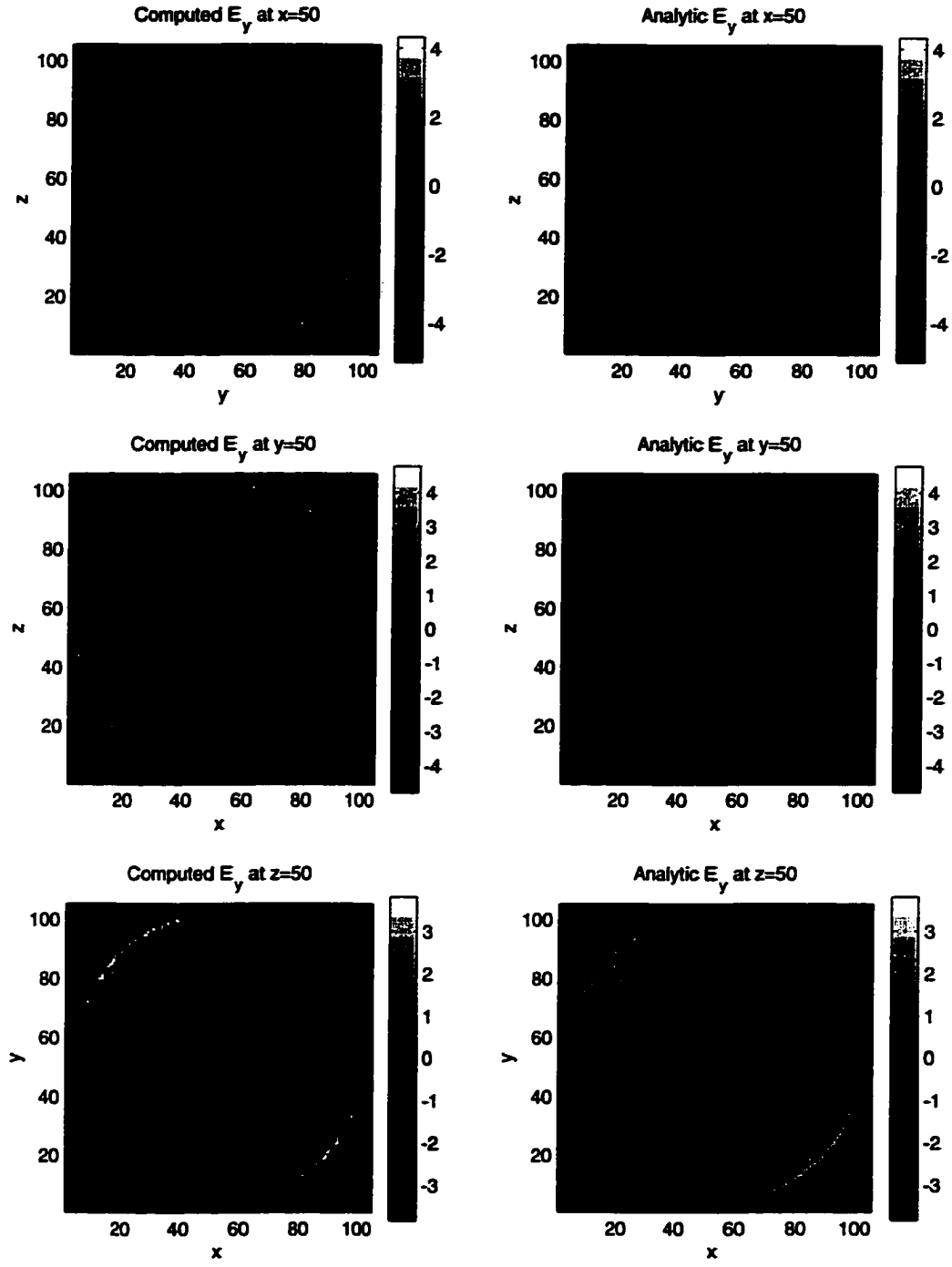

Figure B.2: Magnetic Induction in a lossy sphere from a 60 Hz line-source (1000 V / m at $r = 1\,\mathrm{m}$) - Induced E_y-field (in $\mu\,\mathrm{V}\,/\,\mathrm{m}$) for cross-sections in the three principal planes (computed vs. analytic).

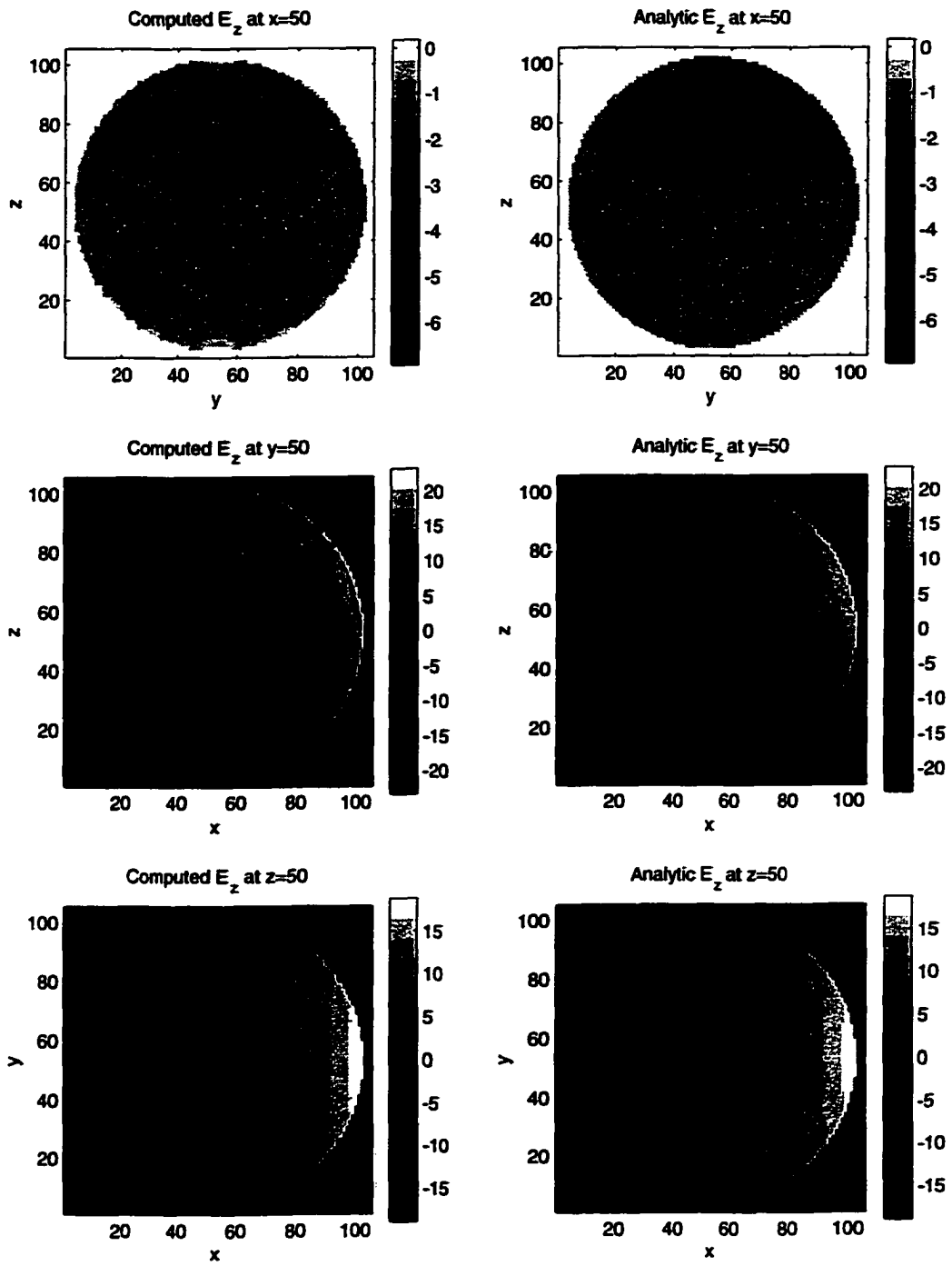

Figure B.3: Magnetic Induction in a lossy sphere from a 60 Hz line-source (1000 V/m at $r = 1\,\mathrm{m}$) - Induced E_z-field (in $\mu\,\mathrm{V/m}$) for cross-sections in the three principal planes (computed vs. analytic).

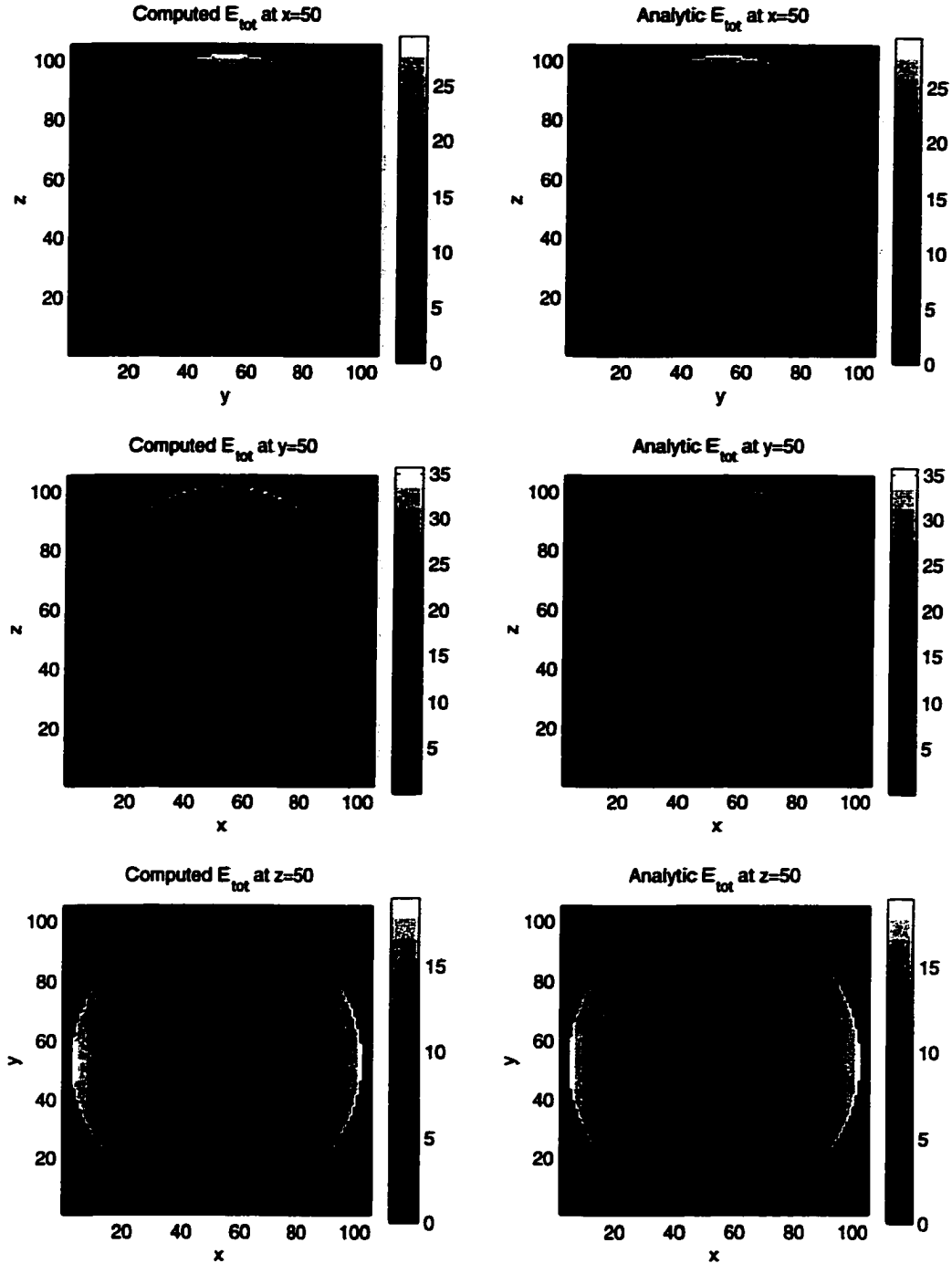

Figure B.4: Magnetic Induction in a lossy sphere from a 60 Hz line-source (1000 V / m at $r = 1\,\mathrm{m}$) - Induced E_{tot}-field (in $\mu\,\mathrm{V}\,/\,\mathrm{m}$) for cross-sections in the three principal planes (computed vs. analytic).

Table B.4: Computed vs Analytic Results for Electric Induction - no post-processing

	Maximum	Average	RMS
Computed Total Electric Field (μV / m)	489.21	103.23	105.46
Analytic Total Electric Field (μV / m)	178.27	102.26	104.28
% Difference $\left(\left\|\frac{Computed-Analytic}{Analytic}\right\| \times 100\right)$	174.4 %	0.9 %	1.1 %
Error Field ($\|Computed - Analytic\|$) (μV / m)	310.93	1.542	5.639

field values. Previous research with plane wave sources has indicated that the method is still valuable because the conductivity gradients in the interior of the human body model are not as great as in the case considered here, in which the conductivity of free space is zero, representing an infinite conductivity gradient at all air-tissue interfaces [93]. No simulations were performed with sub-cell averaging in the case of electric induction, as previous research showed that the averaging actually increased the errors [93].

The large errors evident in electric field induction case are mostly a result of the staircasing approximation of smooth surfaces (this is elaborated in the following section). The immediate cause is the strict enforcement of boundary conditions. This may also be used as a solution, given that the problem of interest represents a very good conductor in quasi-static conditions. It is then reasonable to let the tangential electric fields at the boundary be zero (i.e. the limit for a perfect conductor). This is easily implemented in the post-processing of the data. The external boundary tangential electric field components are identified and set to zero. As a result, the erroneously large computed fields are corrected, and hence the accuracy of the prediction is improved for both the maximum and average electric fields induced.

Table B.5 shows the results using post-processing of the previous data for two different grid resolutions. The post-processing has reduced the maximum error significantly,

Table B.5: Computed vs Analytic Results for Electric Induction - Surface Tangents set to Zero

	Maximum		Average		RMS	
Grid Resolution	1cm	2cm	1cm	2cm	1cm	2cm
Computed Total Electric Field ($\mu V/m$)	224.18	385.45	98.68	104.22	102.50	106.62
Analytic Total Electric Field ($\mu V/m$)	178.27	176.79	97.93	102.51	101.77	104.51
% Difference $\left(\left\|\frac{Computed-Analytic}{Analytic}\right| \times 100\right)$	25.8 %	118 %	0.8 %	1.67 %	0.7 %	2.02 %
Error Field ($\|Computed - Analytic\|$) ($\mu V/m$)	68.12	208.99	1.042	2.679	2.023	7.714

and the average and RMS errors as well. Computed maximum fields are still over-predicted. It is expected that by using a finer grid these errors can be further reduced. Since our computer resources do not allow us to use a finer grid, we used a coarser grid of 2cm to illustrate the effect of the grid size. As expected, the errors increase for this coarser resolution.

B.1.3 Accuracy Evaluation (Staircasing)

Any staircasing approximation changes the object's actual shape and thus the discretized Maxwell's equations enforce different fields at the boundaries than for the actual object. The effects are noticed principally at locations where there is a large discontinuity in material properties. In the FDTD method, it is particularly noticeable for the electric field, as the electric field components are always located on voxel edges, where the object material properties change. Considering a sphere as an example, it is known that the tangential electric field must be continuous across the boundary, and the normal electric flux density must be continuous. By introducing a staircase, we also force continuity conditions which must adapt to abrupt changes in surface normal direction, hence disrupting the expected distribution of field. What is actually simulated is a building block representation of the object.

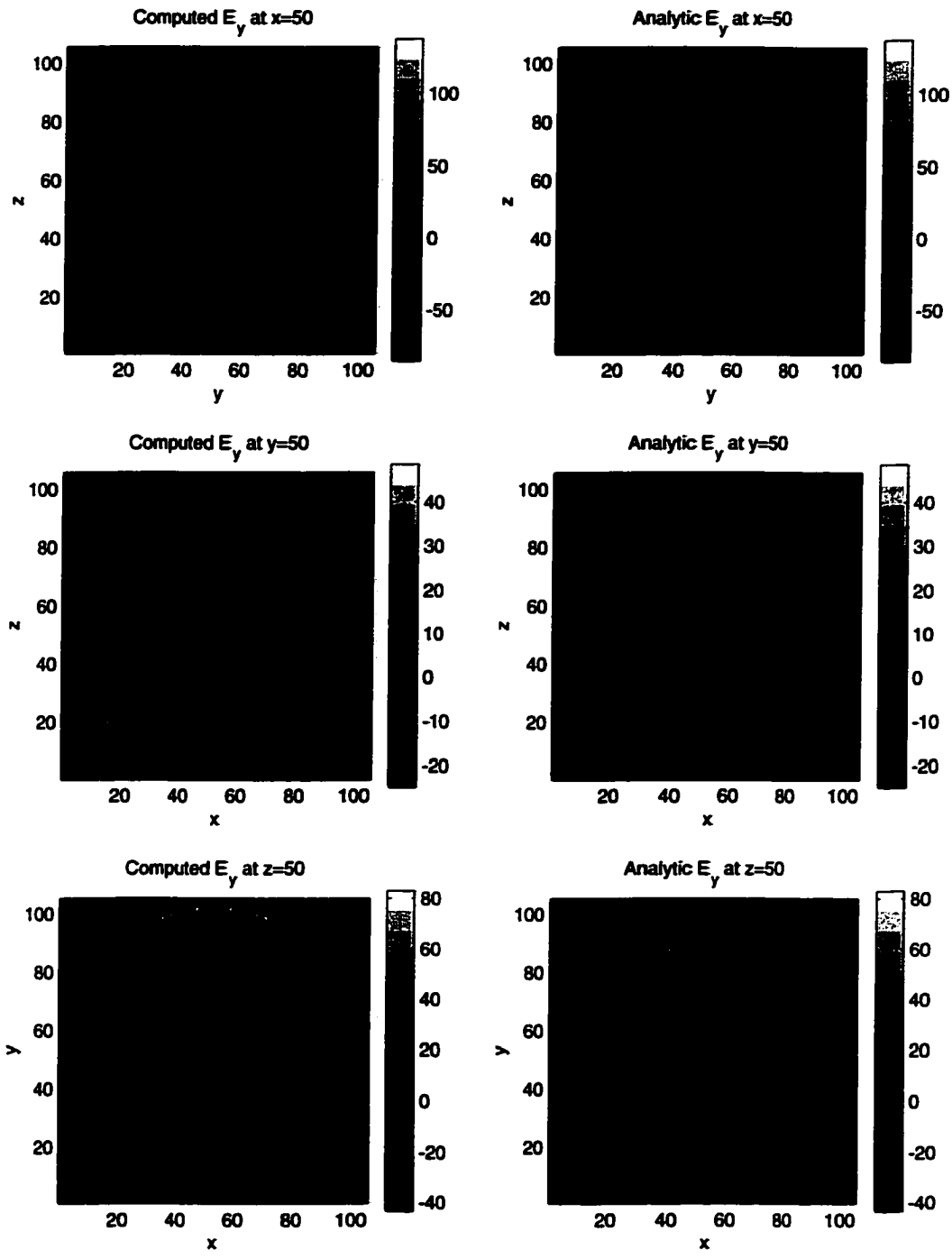

Figure B.5: Electric Induction in a lossy sphere from a 60 Hz line-source (1000 V/m at $r = 1\,\mathrm{m}$) - Induced E_y-field (in $\mu\mathrm{V/m}$) for cross-sections in the three principal planes (computed vs. analytic).

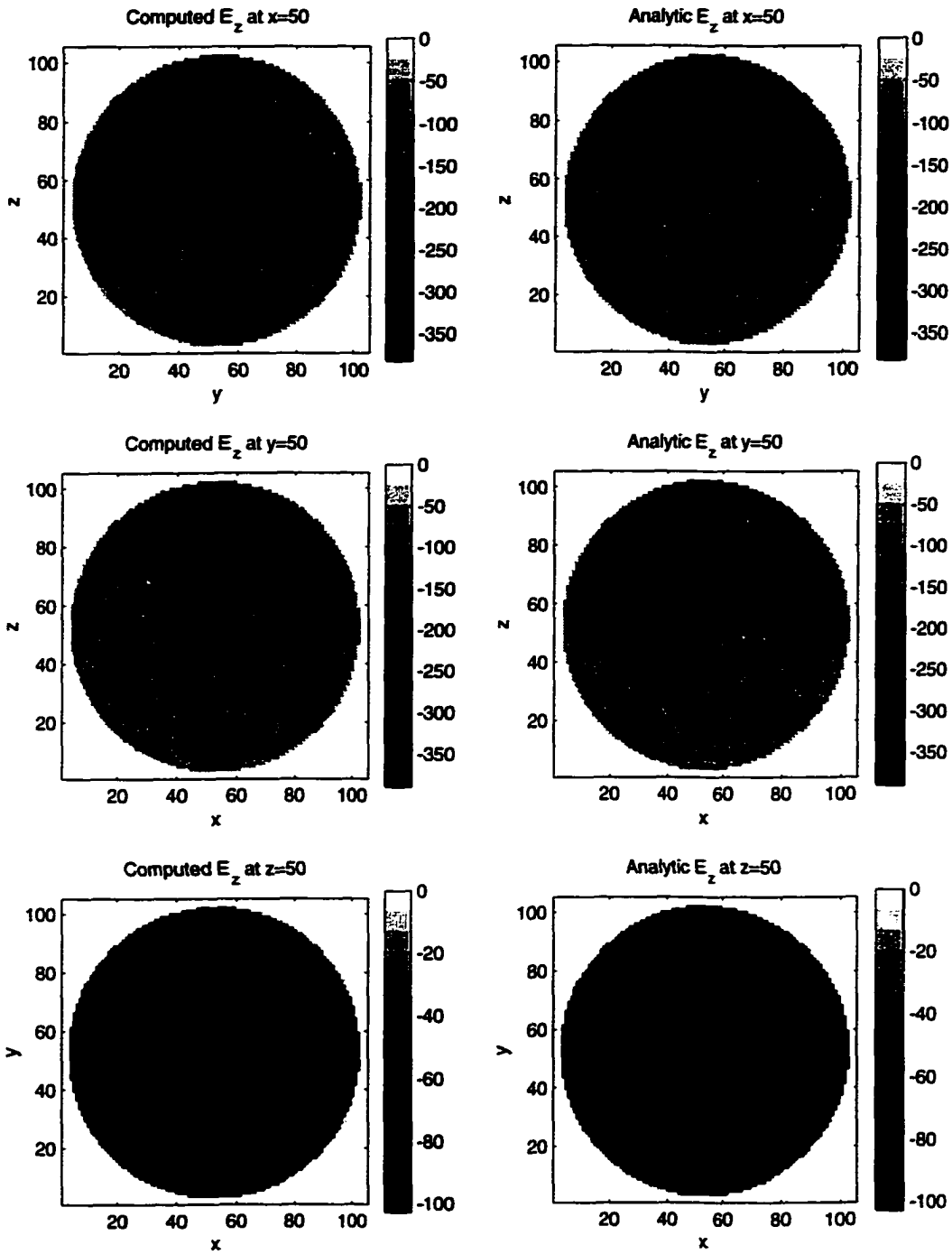

Figure B.6: Electric Induction in a lossy sphere from a 60 Hz line-source (1000 V/m at $r = 1\,\mathrm{m}$) - Induced E_z-field (in $\mu\mathrm{V/m}$) for cross-sections in the three principal planes (computed vs. analytic).

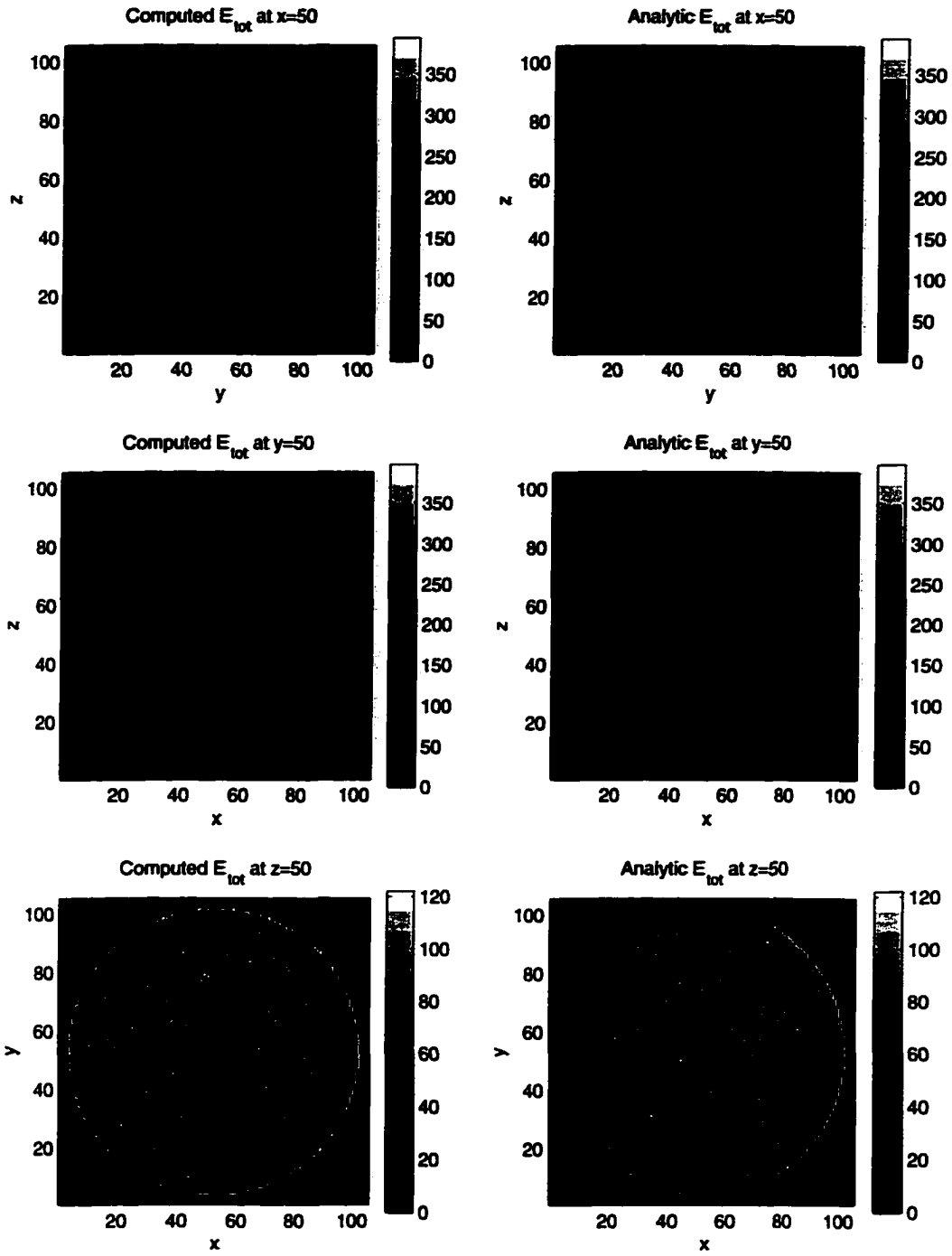

Figure B.7: Electric Induction in a lossy sphere from a 60 Hz line-source (1000 V/m at $r = 1\,\mathrm{m}$) - Induced E_{tot}-field (in $\mu\,\mathrm{V/m}$) for cross-sections in the three principal planes (computed vs. analytic).

For the magnetic induction case the staircasing forces induced currents to flow along a path different from that in a real sphere. High current density is artificially introduced in inner corners of some voxels, resulting in higher than expected field values. For a sphere, the induced currents near the surface would flow continuously around the smooth contour of the sphere. But in the staircased sphere, currents near the surface are impeded by the step approximations. Current flow is effectively constricted around "inside" corners, resulting in high current density (over-predicted values). This is much like the flow of water near a right angle wedge that lies in its path.

For electric induction, first consider that a very good, albeit imperfect, conductor is simulated. As is known for conductors illuminated by incident electric fields, the induced currents and charges tend to concentrate at sharp edges or corners, where field singularities exist. Although the sphere is smooth (and hence would show no charge singularities), simulations actually model a staircased sphere which consists of multiple sharp corners. The results from these simulations show that fields are highly over-predicted, as the program tries to accurately reflect the true singularities that are expected at corners of a staircased object.

The errors for the line-source example are of similar character and magnitude to those encountered for plane wave excitation [93]. This has implications for any simulations involving studies of more complicated lossy structures, since maximum field values for isolated volumetric regions will be over-predicted if the region contains boundaries with high conductivity gradients.

Appendix C

The Partial Eigenfunction Expansion Method Applied to a Rectangular Waveguide

For modeling shielded structures, Mrozowski shows [60, 59] that for a waveguide, it is easy to solve discretely only the longitudinal component of the field, since the transverse configuration is known analytically. Thus numerical considerations can be reduced to one dimension, with the transverse analytic components being added as required.

Consider the case of a rectangular waveguide of width a and height b, with the z-direction being longitudinal. For instance, for the TM_z mode the field components can be expressed as $E_z = \sin(\frac{m\pi}{a}x)\sin(\frac{n\pi}{b}y)u(z,t)$ and $H_z = 0$, with $u(z,t)$ as an amplitude function dependent only on the longitudinal component and time. For general rectangular waveguide problems, Maxwell's curl equations can be separated into six component

equations (C.1-C.6), with β as the phase velocity, and $\omega = 2\pi f$ as the radial frequency.

$$\frac{\partial E_z}{\partial y} + j\beta E_y = -j\omega\mu H_x \tag{C.1}$$

$$-\frac{\partial E_z}{\partial x} - j\beta E_x = -j\omega\mu H_y \tag{C.2}$$

$$\frac{\partial E_y}{\partial x} - \frac{\partial E_x}{\partial y} = -j\omega\mu H_z \tag{C.3}$$

$$\frac{\partial H_z}{\partial y} + j\beta H_y = j\omega\epsilon E_x \tag{C.4}$$

$$-\frac{\partial H_z}{\partial x} - j\beta H_x = j\omega\epsilon E_y \tag{C.5}$$

$$\frac{\partial H_y}{\partial x} - \frac{\partial H_x}{\partial y} = j\omega\epsilon H_z \tag{C.6}$$

For the simple TE_{m0} mode it is known that:

$$E_y = -j\omega\mu\frac{m\pi}{k_x^2 a}K\sin(\frac{m\pi}{a}x)e^{-j\beta z} = Ae_y(z,t)\sin k_x x \tag{C.7}$$

$$H_x = j\beta\frac{m\pi}{k_x^2 a}K\sin(\frac{m\pi}{a}x)e^{-j\beta z} = Bh_x(z,t)\sin k_x x \tag{C.8}$$

$$H_z = A\cos(\frac{m\pi}{a}x)e^{-j\beta z} = Ch_z(z,t)\cos k_x x \tag{C.9}$$

$$E_x = E_z = H_y = 0 \tag{C.10}$$

Take these expressions for the known TE_{m0} fields and substitute them into (C.1-C.6) and three time-step equations are developed which are, more importantly, dependent only on z and t:

$$-A\frac{\partial}{\partial z}e_y(z,t) = -\mu B\frac{\partial}{\partial t}h_x(z,t) \tag{C.11}$$

$$k_x Ae_y(z,t) = -\mu C\frac{\partial}{\partial t}h_z(z,t) \tag{C.12}$$

$$B\frac{\partial}{\partial z}h_x(z,t) + k_x Ch_z(z,t) = A\epsilon\frac{\partial}{\partial t}e_y(z,t) \tag{C.13}$$

These equations can be solved and then multiplied by the *known* transverse configuration to develop the complete field. The same process can be repeated for all modes, and hence a set of one dimensional equations for each mode can be developed. Substantial numerical savings are recovered for large computational domains compared to the conventional modeling using the standard three-dimensional FDTD method.

Although the case of a rectangular waveguide has been used as an example, any perfectly conducting guiding structure with known transverse components can be approached with this method. Mrozowski et al. demonstrated the same methodology for cylindrical waveguiding structures in [62]. A finite set of planes or slices in the rectangular waveguide (or cylinders in the cylindrical waveguide) is used to discretize the wave propagation direction, and transverse analytic functions are factored in as necessary for analysis.

Appendix D

Spherical Wave Theory

In this appendix, details regarding spherical waves are developed, based on [3] and [63], with some input from [74] and [77]. Spherical waves are produced in the solution of Maxwell's equations in spherical coordinates. For a sourceless closed domain of homogeneous, isotropic medium, all electromagnetic field vectors $C \in \left\{\vec{E}, \vec{H}, \vec{B}, \vec{D}\right\}$ satisfy

$$\nabla\nabla \cdot C - \nabla \times \nabla \times C + k^2 C = 0 \tag{D.1}$$

where $k^2 = \epsilon\mu\omega^2 + j\sigma\mu\omega$. In rectangular coordinates, the solution for C is three scalar equations. For spherical waves, first note that the corresponding fields can be developed from the solution to a scalar potential function $\psi(r, \theta, \varphi) = R(r)\Theta(\theta)\Phi(\varphi)e^{j\omega t}$ that satisfies:

$$\nabla^2\psi + k^2\psi = 0 \tag{D.2}$$

By expressing (D.2) in spherical coordinates, a solution for ψ is found by separation of variables. The three equations obtained by separation of variables are given in (D.3). Solutions to (D.3) are spherical Bessel functions $z_n^{(i)}(kr)$, associated Legendre functions

$P_n^m(\cos\theta)$, and sinusoids $\begin{matrix}\cos\\ \sin\end{matrix} m\varphi$ accordingly.

$$\frac{1}{r^2}\frac{d}{dr}(r^2\frac{dR}{dr}) + \left[\frac{\omega^2}{c^2} - \frac{n(n+1)}{r^2}\right] R = 0 \qquad \text{(D.3a)}$$

$$\frac{1}{\sin\theta}\frac{d}{d\theta}(\sin\theta\frac{d\Theta}{d\theta}) + \left[n(n+1) - \frac{m^2}{\sin^2\theta}\right]\Theta = 0 \qquad \text{(D.3b)}$$

$$\frac{d^2\Phi}{d\varphi^2} + m^2\Phi = 0 \qquad \text{(D.3c)}$$

and so the full solution for ψ is $\psi(r,\theta,\varphi) = z_n^{(i)}(kr)P_n^m(\cos\theta)\begin{matrix}\cos\\ \sin\end{matrix} m\varphi$ (time harmonic suppressed).

The spherical Bessel functions $z_n^{(i)}(kr)$ are found from regular Bessel functions as $z_n^{(i)}(kr) \equiv \sqrt{\frac{\pi}{2kr}} Z_{n+1/2}(kr)$, where (i) represents the type of function:

$$z_n^{(1)}(kr) \equiv j_n(kr), \quad z_n^{(2)}(kr) \equiv y_n(kr)$$

$$z_n^{(3)}(kr) \equiv h_n^{(1)}(kr), \quad z_n^{(4)}(kr) \equiv h_n^{(2)}(kr)$$

representing,respectively, Bessel functions of the first and second kind, and Hankel functions of the first and second kind. The first two appear in standing wave solutions, and the last two represent incoming and outgoing radiation waves. The associated Legendre functions $P_n^m(\cos\theta)$ have been explored in great detail in many references, and so they will not be fully explored here. Note that $P_n^m(\cos\theta)$ is zero for $m > n$, where n represents the polar (θ) wave order, and m represents the azimuthal wave order.

With the solution for ψ known, two solutions $\vec{m}_{\begin{matrix}e\\ o\end{matrix}mn}^{(i)}$ and $\vec{n}_{\begin{matrix}e\\ o\end{matrix}mn}^{(i)}$ for the electromagnetic field vectors can be found from:

$$\vec{m}_{\begin{matrix}e\\ o\end{matrix}mn}^{(i)} = \nabla \times (r\psi) = \frac{1}{k}\nabla \times \vec{n}_{\begin{matrix}e\\ o\end{matrix}mn}^{(i)} \qquad \text{(D.4)}$$

where e, o denote an even/odd azimuthal (φ) dependence. Using these as the possible modal solutions for Maxwell's equations in spherical coordinates, one is then led to the full

expressions for the electric and magnetic fields as spherical wave expansions:

$$\vec{E} = -\sum_{n=1}^{N}\sum_{\substack{m=0 \\ e,o}}^{n}\left(a^{(i)}_{\substack{e \\ o}mn}\,\vec{m}^{(i)}_{\substack{e \\ o}mn} + b^{(i)}_{\substack{e \\ o}mn}\,\vec{n}^{(i)}_{\substack{e \\ o}mn}\right)e^{j\omega t} \tag{D.5}$$

$$\vec{H} = \frac{k}{j\omega\mu}\sum_{n=1}^{N}\sum_{\substack{m=0 \\ e,o}}^{n}\left(a^{(i)}_{\substack{e \\ o}mn}\,\vec{n}^{(i)}_{\substack{e \\ o}mn} + b^{(i)}_{\substack{e \\ o}mn}\,\vec{m}^{(i)}_{\substack{e \\ o}mn}\right)e^{j\omega t} \tag{D.6}$$

given that the spherical vector wave functions are:

$$\vec{m}^{(i)}_{\substack{e \\ o}mn} = \left(\mp\frac{m}{\sin\theta}z_n^{(i)}(kr)P_n^m(\cos\theta)\begin{matrix}\sin \\ \cos\end{matrix}m\varphi\right)\hat{\theta} - \left(z_n^{(i)}(kr)\frac{\partial P_n^m(\cos\theta)}{\partial\theta}\begin{matrix}\cos \\ \sin\end{matrix}m\varphi\right)\hat{\varphi} \tag{D.7}$$

$$\vec{n}^{(i)}_{\substack{e \\ o}mn} = \left(\frac{n(n+1)}{kr}z_n^{(i)}(kr)P_n^m(\cos\theta)\begin{matrix}\cos \\ \sin\end{matrix}m\varphi\right)\hat{r} + \left(\frac{1}{kr}\frac{\partial}{\partial r}\left[rz_n^{(i)}(kr)\right]\frac{\partial}{\partial\theta}P_n^m(\cos\theta)\begin{matrix}\cos \\ \sin\end{matrix}m\varphi\right)\hat{\theta} \left(\mp\frac{m}{kr\sin\theta}\frac{\partial}{\partial r}\left[rz_n^{(i)}(kr)\right]P_n^m(\cos\theta)\begin{matrix}\sin \\ \cos\end{matrix}m\varphi\right)\hat{\varphi} \tag{D.8}$$

where $k = \omega\sqrt{\epsilon\mu} = 2\pi/\lambda$ and ω, ϵ, and μ are real constants. Also note that the expansion coefficients, $a^{(i)}_{\substack{e \\ o}mn}$ for TE waves and $b^{(i)}_{\substack{e \\ o}mn}$ for TM waves, will change their values depending on the source of the spherical waves.

Both m and n are restricted to integer values by periodicity requirements, and hence modal solutions are achieved in free space. For an exact representation of fields, the mode number $N \to \infty$. However, unlike plane wave or cylindrical wave expansions, spherical wave expansions can be terminated at some finite integer N, such that the resulting expansion contains a specified percentage of the analytic total power. In practice, this limit on N becomes $N \cong kr_0$ where r_0 is a the radius of a sphere which completely encloses the sources of the field [75]. Any modes greater than N effectively do not propagate. This

becomes a cut-off criterion for free space, where we can limit the number of modes necessary to adequately represent the resultant field. An expansion is only valid in a particular region of space; and if the origin is shifted, the expansion coefficients change.